

THE DEPENDENCE OF LEAD-SALT NANOCRYSTAL
PROPERTIES ON MORPHOLOGY AND DIELECTRIC
ENVIRONMENT

A Dissertation

Presented to the Faculty of the Graduate School

of Cornell University

in Partial Fulfillment of the Requirements for the Degree of

Doctor of Philosophy

by

Adam Christopher Bartnik

January 2011

© 2011 Adam Christopher Bartnik
ALL RIGHTS RESERVED

THE DEPENDENCE OF LEAD-SALT NANOCRYSTAL PROPERTIES ON MORPHOLOGY AND DIELECTRIC ENVIRONMENT

Adam Christopher Bartnik, Ph.D.

Cornell University 2011

The IV-VI semiconductors, and specifically the lead-salts (PbS, PbSe, and PbTe), are a natural choice for nanocrystal science. In nanocrystals, because of their narrow band gap, small effective masses, and large dielectric constants, they offer a unique combination of both strong confinement and strong dielectric contrast with their environment. Studying how these two effects modify optical and electrical properties of nanocrystals will be the topic of this dissertation.

We begin with a summary of the synthesis of high-quality PbS and PbSe nanocrystals. Special care is taken to explain the chemical procedures in detail to an audience not expected to have significant prior chemistry knowledge. The synthesized nanocrystals have bright and tunable emission that spans the edge of the visible to the near-IR spectrum (700-1800 nm), and they are capped with organic ligands making them easily adaptable to different substrates or hosts. This combination of high optical quality and flexible device engineering make them extremely desirable for application.

Moving beyond single-material nanocrystals, we next explore nanocrystal heterostructures, specifically materials with a spherical core of one semiconductor and a shell of another. Core-shell structures are commonly used in nanocrystals as a method to separate the core material, where the electrons and holes are expected to stay, from interfering effects at the surface. This typically results in improvements in stability and fluorescence quantum efficiency. To that end, we develop a model

to explain how confinement plays out across abrupt changes in material, focusing on the optical and electrical properties of recently synthesized PbSe/PbS core-shell quantum dots. We show that for typical sizes of these nanocrystals, a novel type of nanocrystal heterostructure is created, where electrons and holes extend uniformly across the abrupt material boundary, and the shell does not act as a protecting layer. For very large sizes not yet achievable, we expect that the electron and hole will separate in different layers, with potentially measurable effects. Comparisons are made to optical and electrical measurements on these structures, showing good agreement.

Next, we explore how shape can impact nanocrystal properties, on top of their intrinsic size or material dependence. By looking at cylindrically shaped nanocrystals, called “nanorods,” with aspect ratios $\lesssim 10$, we explore how having a slightly extended dimension can impact nanocrystal properties. A model is developed to explain their electronic structure, with surprising results. Foremost is that along the extended dimension, electrons and holes are strongly electrically bound, not with each other directly, but with their image charges in the outer host dielectric material. Nevertheless, the energy spectra of the excitons remains nearly host-independent, with the effects of this strong binding instead seen in a redistribution of transition oscillator strength. To test the model, we develop a novel synthesis of high quality PbSe nanorods, and find good agreement with measured absorption spectra.

Finally, we present a study on the transfer of charge into and out of a nanocrystal. By modeling the charge transfer process within a modified Marcus Theory, we isolate the relevant parameters that can be used to control the rate of transfer. Primary among these are the values of the quantum dot energy levels, and the electrostatic charging energy of the acceptor. We vary the former by changing the

quantum dot size, and the latter by varying the host dielectric constant. To test the model, we chemically bind a small molecular acceptor molecule to the surface of PbS nanocrystals and use transient fluorescence to measure the rate of charge transfer. Both the dependence of the rate on quantum dot size and host dielectric constant show good agreement with the model.

BIOGRAPHICAL SKETCH

Adam Bartnik was born in Bloomington, Indiana in 1980, though most of his childhood and all of his teenage years were spent in Murray, Kentucky, a small college town with a good school system. From nearly the beginning he knew he wanted to be a physicist. At one point as a young child, he was asked what he wanted to be when he grew up– the immediate response was that he was, “going to go to MIT and become a physicist.” Though the location changed, the passion for understanding how the universe worked never did.

In 1998 he went to Cornell University to study physics, and it was in that major that he met his future wife, Laurel. He graduated from Cornell University with a B.A. in physics in 2002, and traveled with Laurel to the University of Pennsylvania to continue his education in their Ph.D. program. They spent one year there, before deciding that the quality of life was better in Ithaca. After returning to Ithaca, they then took turns getting higher education at Cornell, with Adam working for one year while Laurel earned a masters, followed by Adam’s entrance into the Applied Physics Ph.D. program.

Adam joined the Frank Wise group as a Ph.D. candidate in 2005. Since then he has researched lead-salt nanocrystals, both with theoretical modeling and through optical spectroscopy. He has enjoyed every minute of the time spent here, and both the subject material and the atmosphere will be greatly missed as he continues after his degree.

To my parents for giving me support, my wife for giving me focus, and my son
for giving me purpose.

ACKNOWLEDGEMENTS

First and foremost, I cannot thank Frank Wise enough for being a truly unique and wonderful advisor. He is insightful, motivational, caring, and understanding to a depth that I did not expect from a Ph.D. advisor. I would also like to thank my committee members, Alexander Gaeta and Michal Lipson, for their guidance.

It has been an absolute pleasure to work with the Wise group members. Foremost, I would like to thank Byung-Ryool (Yul) Hyun, for teaching me practical experimental knowledge, for guidance in research and elsewhere, for being a remarkably patient and caring guy, and for making me an honorary member of the Korean mafia. I thank Liangfeng Sun for his contagious calm demeanor, his assistance with my research, and especially for all the five dollar dining hall lunches. I thank Simon Lefrancois for using his seemingly boundless knowledge of all areas of physics to help give me intuitive grasp of concepts, and for teaching me, at length, of the classification system of Scandinavian black metal music¹. I thank William Renninger for his ability to impersonate a Bob Dylan song on any random topic—including fiber lasers—and his random, noisy, often musical, but always hilarious outbursts while otherwise sitting quietly at his computer. I thank Josh Choi for routinely demonstrating that “dude”, “freaking awesome”, and “nanocrystal” can be used together effectively in the same sentence. I will truly miss all you guys!

Finally, I am forever indebted to my wife, Laurel, for her love and patient support for all of these years. Yes, I am finally done.

¹For example, I believe this dissertation is neither “grim” nor “necro.”

TABLE OF CONTENTS

Biographical Sketch	iii
Dedication	iv
Acknowledgements	v
Table of Contents	vi
List of Tables	ix
List of Figures	x
BIBLIOGRAPHY	xv
1 Introduction	1
1.1 Quantum Dots	1
1.2 Envelope Function Theory	4
1.3 Organization of the Dissertation	8
BIBLIOGRAPHY	11
2 Quantum Dot Synthesis	12
2.1 Introduction	12
2.2 The Synthesis Setup	14
2.3 Common Themes in Nanocrystal Syntheses	16
2.3.1 Creating an N ₂ environment	17
2.3.2 Filling the flask with a liquid reactant	18
2.3.3 Vacuuming during the synthesis	19
2.3.4 Preparing reactants over long periods of time	19
2.3.5 Purification of the nanocrystal products	20
2.4 PbS Quantum Dot Synthesis	22
2.5 PbSe Quantum Dot Synthesis	27
2.6 Troubleshooting Common Problems	31
2.7 Conclusions	33
BIBLIOGRAPHY	34
3 Core-Shell Quantum Dots	36
3.1 Introduction	36
3.2 Theory	37
3.3 Solutions	40
3.4 Discussion	42
3.5 Comparison with Experiment	46
3.5.1 Experimental Methods and Chemical Synthesis	46
3.5.2 Optical Spectroscopy	47
3.5.3 Scanning Tunneling Spectroscopy	48
3.6 Conclusion	52

BIBLIOGRAPHY	53
4 Lead–salt Nanowires and Nanorods	54
4.1 Introduction	54
4.2 Four band effective mass model	56
4.3 Energy spectra in PbSe Nanowires	59
4.4 Dielectric confinement	65
4.5 1D excitons in PbSe nanowires and nanorods	68
4.5.1 Finite length effects	74
4.5.2 Oscillator strength of the interband optical transitions	77
4.6 Experiment	79
4.6.1 Difficulties encountered in nanorod syntheses	79
4.6.2 Nanorod synthesis using TDP	83
4.6.3 Absorption Spectra	85
4.7 Discussion and Conclusions	92
BIBLIOGRAPHY	95
5 Charge Transfer in Quantum Dots	99
5.1 Absolute Energy Levels in Lead–Salt QDs	102
5.1.1 Introduction	102
5.1.2 The Transport Energy Gap	104
5.1.3 Calculating the Absolute Energy Levels	106
5.1.4 Comparison to Cyclic Voltammetry	109
5.2 Reorganization Energy	111
5.3 Charge Transfer to Molecular Acceptors	113
5.4 Conclusion	120
BIBLIOGRAPHY	122
6 Future directions	124
BIBLIOGRAPHY	127
A Additional Syntheses	128
A.1 CdSe Quantum Dots	128
A.2 Hexadecylxanthate ligands	130
BIBLIOGRAPHY	133
B PbSe Nanorods	134
B.1 Effect of anisotropy on the nanowire energy spectra	134
B.2 Calculations of the one dimensional Coulomb potential	136
B.3 Numerical calculation of the exciton binding in PbSe nanorods	139
B.4 Choice of the room temperature band parameters	139

BIBLIOGRAPHY	143
C Nanocrystal Vibrational Spectra	145
C.1 Introduction	145
C.2 Quantum Dot Vibrational Model	146
C.2.1 The System of Equations	147
C.2.2 Description of Solutions	150
C.2.3 Boundary Conditions in Heterostructures	151
C.2.4 Boundary Conditions in Quantum Dots	152
C.2.5 Theoretical Pitfalls	153
C.2.6 Conclusion	154
BIBLIOGRAPHY	155

LIST OF TABLES

2.1	Chemicals needed for a typical synthesis of PbS QDs.	22
2.2	Chemicals needed for a typical synthesis of PbSe QDs.	28
2.3	Suggested temperatures for various QD absorption peak ranges for PbSe NC syntheses.	30
3.1	Bulk Band Parameters.	39
4.1	Energy band parameters that provide the best fits to the room temperature data from PbSe NCs. The left columns show the transverse band components, while the right columns show the ratio of transverse to longitudinal components.	90
4.2	Transitions observed in the absorption spectra of PbSe NRs.	91
A.1	Chemicals needed for a typical synthesis of CdSe QDs.	128
A.2	Chemicals needed for a synthesis of lead hexadecylxanthate.	130
C.1	Boundary conditions at the surface of nanocrystals. The common electromagnetic BCs are shown on top, while the four common choices of mechanical BCs are on bottom.	153

LIST OF FIGURES

1.1	The widening of the energy gap and focusing of the density of states as a bulk semiconductor is decreased in size from a QD to single molecule.	2
1.2	Schematic of the environment of a PbS quantum dot. A 3-10 nm roughly spherical core of PbS crystal is surrounded by ~ 2 nm organic surface molecules, and all are immersed in a solvent. The optical dielectric constants are labeled for all elements.	3
1.3	Envelope function models of PbS QDs. Symbols show QD sizes measured using a scanning tunneling electron microscope (STEM).	7
2.1	A typical Schlenk line setup.	14
2.2	Absorption and emission spectra of typical sizes of synthesized PbS QDs.	26
2.3	(a) STEM image of PbS QDs as synthesized in our lab (full picture width or height is 31.5 nm). (b) Relation between diameter and optical energy gap of PbS QDs. TEM data from Refs. [1, 2, 3] and STEM data from Ref. [4] are shown, along with the prediction from a 4-band envelope function theory calculation.	26
2.4	Absorption and emission spectra from a synthesis of PbSe QDs at 140°C for various growth times.	29
2.5	Literature values [5, 6, 7, 8, 9, 10] of the first absorption peak in PbSe QDs versus size compared to calculations using the band parameters from Ref. [11] and band parameters chosen to best fit the trend (see Appendix B.4).	31
3.1	Energy gaps in PbSe/PbS core-shell QDs.	38
3.2	LUMO and HOMO energy levels of PbSe/PbS QDs with (a) fixed shell thickness and (b) fixed outer diameter.	43
3.3	Wavefunctions for a constant 3 nm diameter core and variable shell thickness of (a) 0.0 nm, (b) 0.83 nm, (c) 1.67 nm, (d) 2.5 nm.	44
3.4	Wavefunctions for a constant 6 nm diameter core and variable shell thickness of (a) 0.0 nm, (b) 1.67 nm, (c) 3.33 nm, (d) 5.0 nm.	45
3.5	Experimental transition energies inferred from absorption (a) & (b), and predicted values (c) & (d). Shell thicknesses from 0 to 3 monolayers (ML) with various core sizes are shown.	48

3.6	(a) Plots of dI/dV_{bias} vs. ηV_{bias} (called “Energy”) for one core and three core-shell QDs. All QDs have a PbSe core of 4.4 nm diameter. (b) Energy gaps of core-shell QDs from different sources. The black line is calculated from the present model. The green line+triangles is the gap determined by subtracting the location of the HOMO peak from the LUMO peak in the STS spectra in (a). The red circles are determined by subtracting the coulomb energy 2Σ in Eq. (3.8) from the STS energy gaps. Finally the blue triangles are from the first optical absorption peak.	51
3.7	The tunneling spectra for (a) 5.9 nm and (b) 6.8 outer diameter core-shell QDs. Black lines are the measured spectra, and the vertical grey bars indicate predicted locations of the electron and hole energy levels, which are the bare energies plus the Coulomb charging correction, $E_i \pm \Sigma$, where the + is for electrons and the – for holes.	51
4.1	Energy gaps of a 4-nm diameter PbSe NW at each of the four valleys as a function of the growth direction of the NW (red lines). The numbers indicate the valley degeneracy of the energy gaps. Dashed grey lines are the same energy gaps after accounting for the self-Coulomb interaction, described later in the text.	63
4.2	1D band structure of a 4-nm PbSe NW for the cases of the axis along the directions (a) $\langle 111 \rangle$ and (b) $\langle 100 \rangle$. The bands are labeled by the angle θ between the considered valley and the rod growth axis and also by their multiple valley degeneracy, up to a maximum of (x4). In (b), the individual subbands are labeled using notation adopted from molecular physics: $kX_{ n }^{e,h}$ for the k^{th} electron or hole level of certain symmetry with total z angular momentum n , where $X = \Sigma, \Pi, \Delta, \dots$, is used for $ m = 0, 1, 2, \dots$, respectively, where m is the angular momentum projection of the conduction (valence) band component of the wavefunction of the electron, ‘e’, (hole, ‘h’) state. In (a), the order of the levels is the same, and the labeling is suppressed for clarity.	64
4.3	Points show the effective binding potential, $V_{1/2,1}^{1/2,1}$, between an electron and a hole occupying the ground one dimensional subband $n = n' = 1/2$ and $k = k' = 1$ as a function of their separation, calculated for a 4-nm radius PbSe NW. The solid line shows the approximation of this dependence by the Elliott & Loudon effective potential described by Eq. (4.21)	67
4.4	Fitting parameters used in the effective potential described by Eq. (4.21) in PbSe NWs of various radius and medium dielectric constant. The parameter is plotted vs. (a) nanowire diameter with $\kappa_m = 2$ (b) medium dielectric constant with $R = 2$ nm.	70

4.5	Coulomb energies calculated for (a) $\kappa_m = 2$ with varying R and (b) $R = 2$ nm with varying κ_m . Lines are the sum of the electron $E_{\text{self,e}}^{1/2,1}$ and hole $E_{\text{self,h}}^{1/2,1}$ self interaction energies (red circles); the electron-hole binding energy ε_0 (blue triangles); and their total (black squares).	72
4.6	Dependence on PbSe NW radius of the average (r.m.s.) separation of the electron and hole in the 1D exciton. Inset shows the square of the ground exciton wavefunction $ \psi_{1D} ^2$ for a NW with 2 nm radius.	74
4.7	Comparison of the numerically and analytically calculated 1D exciton wavefunctions $ \Psi_{1D} ^2$. Each subplot has axes z_e and z_h ranging along the length of the nanorod from 0 to L . The two lowest energy states and the 17th state are shown.	75
4.8	Numerically-calculated energies for the lowest few exciton states in a 4 x 20 nm PbSe NR (black circles). The lines are the energies from the analytic model using two different confinement lengths for the center of mass.	77
4.9	TEM image of the PbS cubes formed during an attempted nanorod synthesis.	81
4.10	TEM image of the result of attempted PbS nanorod synthesis <i>via</i> decomposition of Pb-HDX. Both straight and curved thin nanorods along with fatter nanorods, cubes, spheres, and aggregates of PbS are visible. This image was nicknamed the “nano-zoo”.	83
4.11	(a) TEM image of typical PbSe NRs. (b) High-resolution TEM image of an individual PbSe NR. (Inset: FFT image of the (100) face.)	85
4.12	(a) Absorption spectra of PbSe NRs (black line, vertically offset for clarity) and spherical PbSe NCs (red line) are compared. The inset shows detail of the first peak. (b) Emission spectra and fluorescence decays measured at the emission peak (inset) of the same two samples.	87
4.13	(a) Example absorption spectra of a 3.9 x 17 nm PbSe NR. Inset shows the same data, but on a scale where the 5th peak is visible. (b) Peaks in 2nd derivative spectrum as a function of NR diameter (symbols), calculated allowed transitions (grey lines), simple parabolic effective mass calculation around the Σ -point (dashed grey line), and linear fits (colored dashed lines.)	89
5.1	Energy diagram of Marcus theory.	99
5.2	Diagram of the populations of an idealized two level quantum dot system.	105
5.3	Comparison of the bare QD energy levels $E_{1,2}$ and the shifted electron affinity (EA) and ionization potential (IP) locations.	106
5.4	Effective shell+medium dielectric constant as a function of medium dielectric constant for a 3 nm NC, surrounded by an oleic acid shell of thickness S .	108

5.5	Calculated EA and IP of PbS (blue, orange lines) and PbSe (black, red lines) QDs, along with measured CV data (symbols).	110
5.6	Schematic of a single spherical PbS QD donor bound to many DAT molecular acceptors.	114
5.7	EA and IP of PbS QDs as a function of QD diameter and the EA of DAT molecules (flat line). Below diameter D_{crit} , electron transfer from PbS to DAT should be allowed.	115
5.8	Time-integrated fluorescence measurements of PbS QDs bound to DAT molecules. Blue lines are bare QDs without DAT; red lines are after binding to DAT. Inset shows detail of the quenched emission. The QDs smaller than the critical diameter show dramatic quenching in the presence of the DAT electron acceptor.	116
5.9	Measured fluorescence decay times of PbS QDs bound to DAT molecules. In (a) the dependence on QD size is shown, with an unbound 3.0 nm QD shown in the inset. In (b) the dependence on solvent is shown.	117
5.10	Dependence of charge transfer time on various combinations of the solvent dielectric constants. In (a) the standard combination of optical and static constants is chosen. In (b) only the optical constant is used. In neither case is a uniform trend observed with these choices.	118
5.11	Charge transfer time dependence on solvent static dielectric constant (a) and QD size (b). Experimentally measured values (symbols) are compared to calculated trends (colored lines) for different values of the unknown parameter λ_0 . The inset of (a) shows the trends for $\lambda_0 = 0, 0.03, 0.05, 0.15$ eV for even larger static dielectric constants than those measured.	119
B.1	Effect of the energy spectrum anisotropy on the energy of the 1D subband bottom in a 4 nm PbSe NW grown along the (a) $\langle 111 \rangle$ and (b) $\langle 100 \rangle$ crystal axes. The “approximate” calculations are conducted within the cylindrical approximation, which gives Eq. (4.15) for the energy levels. The “full” calculations are performed as described in the text. The energy levels are labeled by the angle between the L-point and the rod growth axis. Note that the $\theta = 0$ energy levels do not require perturbation, as $H_{an} = 0$ for that angle.	137

B.2 Calculations of the lowest electron levels in spherical PbSe NCs. (a) Splitting of the P state induced by the fully anisotropic Hamiltonian in a 4 nm radius NC. Anisotropic states are labeled by writing the state in the basis of isotropic states, and labeling it by the isotropic state with largest coefficient. (b) The size dependence of the transition energies in spherical PbSe NCs. Experimental data [10] are shown by symbols. The solid lines show the size dependence of optically allowed transitions calculated in a fully anisotropic effective mass model. The optically allowed transitions occur between the states of the same symmetry but opposite parity, and we label them by a symmetry type, which is common for both states. Open points indicate transitions originating from the L-point in the Brillouin zone, while half-open points are suggested to be from the Σ point as in Ref. [10]. The dashed line shows the size dependence of lowest confined level connected with the Σ point of the Brillouin zone, calculated in a parabolic effective mass approximation as explained in the text. 142

BIBLIOGRAPHY

- [1] N. F. Borrelli and D. W. Smith, *J. Non-Cryst. Sol.* **180**, 25 (1994).
- [2] L. Cademartiri, E. Montanari, G. Calestani, A. Migliori, A. Guagliardi, and G. A. Ozin, *J. Am. Chem. Soc.* **128**, 10337 (2006).
- [3] I. Moreels, K. Lambert, D. Smeets, D. De Muynck, T. Nollet, J. C. Martins, F. Vanhaecke, A. Vantomme, C. Delerue, G. Allan, and Z. Hens, *ACS Nano* **3**, 3023 (2009).
- [4] J. J. Peterson, Ph.D. thesis, University of Rochester, 2007.
- [5] C. B. Murray, S. Sun, W. Gaschler, H. Doyle, T. A. Betley, and C. R. Kagan, *IBM J. Res. Dev.* **45**, 47 (2001).
- [6] I. Moreels, K. Lambert, D. De Muynck, F. Vanhaecke, D. Poelman, J. C. Martins, G. Allan, and Z. Hens, *Chem. Mater.* **19**, 6101 (2007).
- [7] B. L. Wehrenberg, C. Wang, and P. Guyot-Sionnest, *J. Phys. Chem. B* **106**, 10634 (2002).
- [8] J. Steckel, S. Coe-Sullivan, V. Bulovic, and M. Bawendi, *Adv. Mater.* **15**, 1862 (2003).
- [9] W. W. Yu, J. C. Falkner, B. S. Shih, and V. L. Colvin, *Chem. Mater.* **16**, 3318 (2004).
- [10] R. Koole, G. Allan, C. Delerue, A. Meijerink, D. Vanmaekelbergh, and A. Houtepen, *Small* **4**, 127 (2008).
- [11] I. Kang and F. W. Wise, *J. Opt. Soc. Am. B* **14**, 1632 (1997).

CHAPTER 1

INTRODUCTION

1.1 Quantum Dots

A “quantum dot” (QD) is a small piece of semiconductor crystal, which as a result of its small size, has properties vastly different than those of the bulk semiconductor. The most characteristic of these new properties is the increase of the semiconductor band gap. In bulk, the lead-salts (PbS, PbSe, PbTe) are narrow band gap semiconductors ($E_g \sim 0.3\text{-}0.4$ eV), but the smallest QDs made of those materials have energy gaps as high as 2.5 eV. As a result, QDs can be highly efficient emitters or absorbers with a size-tunable wavelength. In addition to the widening of the band gap, the bands themselves are also modified as the crystal becomes small. The density of states narrow, eventually into discrete states, becoming more similar to molecular energy levels than semiconductor bands. This trend is summarized in Fig. 1.1.

Quantum dots cannot be described as either an infinite periodic crystal or an aperiodic molecular cluster, since they still contain 100-1000 crystal unit cells. QDs occupy an intermediate domain between the two, borrowing some traits from both. For example, the conservation of crystal momentum is partially relaxed in nanocrystals. Instead, selection rules more akin to molecular systems determine allowed optical processes. This provides pathways for processes forbidden in bulk, such as indirect transitions or more efficient Auger recombination. In addition, even among the processes permitted in bulk, dramatic changes occur. For example, the oscillator strength is focused into fewer and fewer transitions as the size decreases, enhancing both linear and nonlinear susceptibilities. All of these

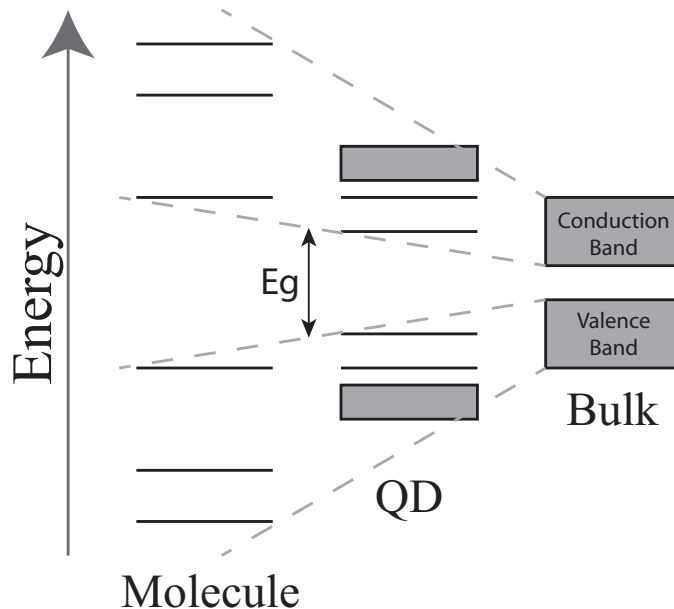


Figure 1.1: The widening of the energy gap and focusing of the density of states as a bulk semiconductor is decreased in size from a QD to single molecule.

changes motivate the study of the optical properties of quantum dots.

As originally understood by Efros and Efros [1], the size below which the crystal begins to show these size-dependent “quantum confinement” effects is the Bohr radius of the electron (a_e), hole (a_h), or exciton ($a_B = a_e + a_h$), depending on which type of particle the experiment considers. The Bohr radii are defined as:

$$a_{e,h} = \frac{4\pi\epsilon_\infty\hbar^2}{m_{e,h}e^2} \quad (1.1)$$

where ϵ_∞ is the optical dielectric constant of the bulk semiconductor and $m_{e,h}$ are the band edge effective masses of the electron and hole. The lead-salts offer uniquely large Bohr radii because they have both small effective masses $m_{e,h} \sim 0.1m_0$ and large dielectric constants $\epsilon_\infty \sim 20$, placing the exciton Bohr radius in the 20-50 nm range. This means that for a given size of nanocrystal below the exciton Bohr radius, the lead-salts show uniquely strong confinement compared to other semiconductor materials [2], and as a result are a particularly interesting

choice as a testbed for nanocrystal science.

In addition to these effects from confinement, the immediate environment surrounding a QD also becomes more important as its size becomes smaller. A diagram of the environment of a lead-salt QD is shown in Fig. 1.2. Lead-salt QDs

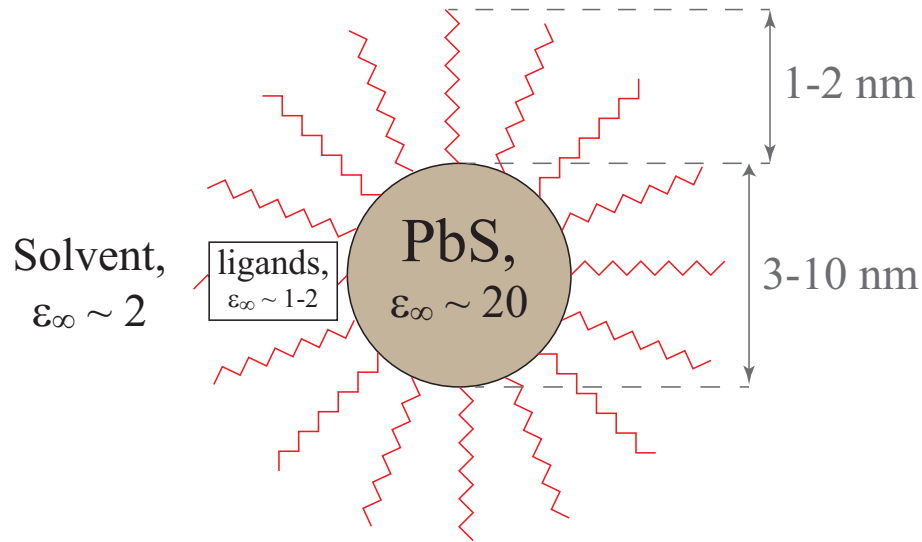


Figure 1.2: Schematic of the environment of a PbS quantum dot. A 3-10 nm roughly spherical core of PbS crystal is surrounded by ~ 2 nm organic surface molecules, and all are immersed in a solvent. The optical dielectric constants are labeled for all elements.

are typically encapsulated with short organic molecules that have the dual purpose of passivating surface trap states and allowing the QDs to be soluble in various solvents. This passivation helps reduce the importance of the details of these molecules, because after the surface trap states are removed, only the QD core states remain, which are more easily modeled. The medium surrounding the QD is often modeled as only affecting the QD through its dielectric constant. This dielectric constant can be very important for QD properties, because the electric field of the electron and hole penetrates into the surrounding medium, which commonly has a dielectric constant much smaller than the QD. Thus, the electron or hole polarize the surface of the QD. In the simple case of a flat interface, for

example, this polarization can be described easily as an interaction with an image charge [3]. In the case of smaller external dielectric constant, the interaction is repulsive. The repulsive potential in nanostructures of any shape leads an additional confinement of electrons or holes, called the “dielectric confinement” effect.

1.2 Envelope Function Theory

In order to model these size-dependent and environment-dependent effects in lead-salt QDs, a theoretical framework is needed. Lead-salt quantum dots have been calculated using many methods, including envelope function theory (also called $\mathbf{k}\cdot\mathbf{p}$ theory) [4], pseudopotentials [5], tight binding [6], and density functional theory [7, 8]. Because of both its simplicity and its amazing prior success at describing QD properties, we choose an envelope function approximation to the electronic wavefunction as our modeling framework. This approximation is based on the standard Bloch separation of the wavefunction into a phase term $\exp[i\mathbf{k}\cdot\mathbf{r}]$ and an atomic function $u_{\mathbf{k}}(\mathbf{r})$, which has the periodicity of the crystal. The envelope function $\Psi_{\text{env}}(\mathbf{r})$ replaces the Bloch phase term in QDs:

$$\Psi_{\text{bulk}} = e^{i\mathbf{k}\cdot\mathbf{r}} u_{\mathbf{k}}(\mathbf{r}) \quad (1.2)$$

$$\Psi_{\text{QD}} = \Psi_{\text{env}}(\mathbf{r}) u_{\mathbf{k}}(\mathbf{r}) \quad (1.3)$$

The total Hamiltonian of the QD system is expressed in terms of the bulk Hamiltonian and a perturbation, $H_{\text{total}} = H_{\text{bulk}} + H_{\text{pert}}$, where H_{pert} are the two additional effects felt in nanocrystals: quantum and dielectric confinement. Quantum confinement is modeled using, typically, an infinite confining potential outside of a sphere of radius R , and dielectric confinement is modeled electrostatically, approximating the QD as a dielectric sphere in a dielectric medium.

Formally, the solutions to the bulk system are assumed to be: $H_{\text{bulk}}\Psi_{\text{bulk}} = E_0\Psi_{\text{bulk}}$, though we will find that the details of Ψ_{bulk} will not be needed. With these assumptions, Slater [9] was the first to analyze these equations within a slowly varying envelope approximation. He discovered the following approximate equation for the envelope function:

$$[E_0(-i\nabla) + H_{\text{pert}}(\mathbf{r})]\Psi_{\text{env}}(\mathbf{r}) = E_{\text{total}}\Psi_{\text{env}} \quad (1.4)$$

That is, inserting the differential form of the wavevector $\mathbf{k} = -i\nabla$ into the energy band dispersion $E_0(\mathbf{k})$ produces a Hamiltonian-like equation for the envelope function. This approximation holds as long as the resulting envelope function is slowly varying over a unit cell. An additional simplification occurs if we stay near the ground state of the system, allowing the function E_0 to be expanded to second order using the effective mass of the energy band. This produces the Schrödinger-like equation:

$$\left[-\frac{\hbar^2}{2m^*}\nabla^2 + H_{\text{pert}}(\mathbf{r})\right]\Psi_{\text{env}} = (E_{\text{total}} - E_0(0))\Psi_{\text{env}} \quad (1.5)$$

where m^* is the band edge effective mass. Amazingly, the details of both the atomic-scale crystal potential and wavefunction are unimportant! Only the band-edge dispersion of the bulk energy band $E_0(\mathbf{k})$ is needed to calculate QD energy levels. This is a dramatic simplification, allowing analytic calculation of QD properties using nothing more than a “particle-in-a-box” model, Eq. (1.5).

So far we have considered only a single band, either conduction or valence, and as such only electrons or holes individually have been treated. To study excitons within a QD, *i.e.* interacting electrons and hole, a similar Hamiltonian that includes their interaction is used:

$$\begin{aligned} \left[-\frac{\hbar^2}{2m_e}\nabla_e^2 - \frac{\hbar^2}{2m_h}\nabla_h^2 - \frac{e^2}{\varepsilon_\infty|\mathbf{r}_e - \mathbf{r}_h|} + V_{\text{image}}(\mathbf{r}_e, \mathbf{r}_h)\right]\Psi_{\text{env}}(\mathbf{r}_e, \mathbf{r}_h) \\ = (E - E_g)\Psi_{\text{env}}(\mathbf{r}_e, \mathbf{r}_h) \end{aligned} \quad (1.6)$$

where $\mathbf{r}_{e,h}$ is the position of the electron or hole, ε_∞ is the dielectric constant of the QD, V_{image} is the image charge potential induced by the dielectric medium, E_g is the bulk semiconductor band gap, and the infinite confining potential has been suppressed with the assumption that the $\Psi_{\text{env}}(\mathbf{r}_e, \mathbf{r}_h)$ solutions go to zero if either \mathbf{r}_e or \mathbf{r}_h is outside of the QD.

If the QD and medium dielectric constants are the same in Eq. (1.6), then there are no image charges and $V_{\text{image}} = 0$, and this equation becomes formally identical to a Hydrogen atom (except for the boundary conditions at the sphere surface). This is what motivates the definition of the Bohr radius in Eq. (1.1), since that is the natural length scale of this equation. Thus, there are two important length scales associated with the system: the Bohr radius a_B and the physical QD radius R . If the NC radius is much larger than the Bohr radii, then the boundary will not be felt, and the exciton wavefunction will be hydrogenic in form. But when the NC radius is much smaller than the Bohr radii, then the boundary determines the form of the wavefunction instead, becoming more like a particle-in-a-box. It is this limit of strong confinement that is important for lead-salt QDs.

In that limit, the ground state solution to this equation has energy $E = E_g + \hbar^2\pi^2/2\mu R^2$, where $\mu = m_e m_h / (m_e + m_h)$ is the reduced mass of the electron and hole, and where we have temporarily ignored the Coulomb terms in the Hamiltonian. Using the effective masses measured in bulk PbS, the predicted size dependence of the band gap, along with the measured trend is shown in Fig. 1.3. The red line is the prediction described above, called the “one-band” model as it considers each single band (conduction and valence) individually. The blue line presents a refinement of this model which includes the coupling between the valence and conduction bands, and treats all four bands (including spin) simul-

taneously. This model will be described in more depth later in the text. It is remarkable that such a simple model could produce such fantastic agreement with experiment, considering the number of approximations used.

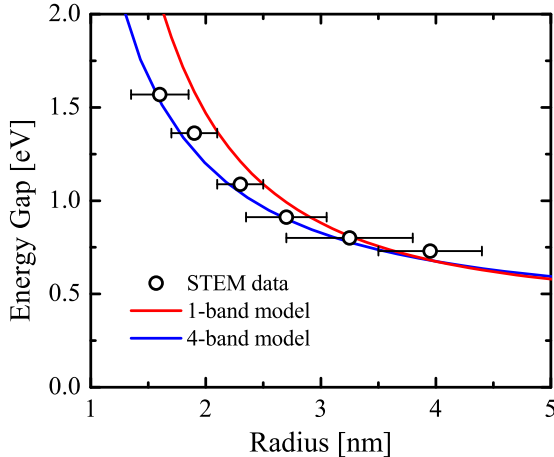


Figure 1.3: Envelope function models of PbS QDs. Symbols show QD sizes measured using a scanning tunneling electron microscope (STEM).

In this analysis, the effects of both the electron-hole Coulomb attraction and the image potential V_{image} in Eq. (1.6) were ignored. In fact, both terms are negligible in spherical lead-salt QDs. The former term is negligible because the large dielectric constants of the lead-salts nearly completely screen out the Coulomb interaction. The latter term is negligible because there is nearly perfect cancelation of charge within a QD, and without a net charge, there are no image charges to consider. This charge cancelation occurs when the electron and hole wave functions are nearly identical, which is true because the shape of the wave function is determined almost entirely by the shape of the nanocrystal. This is always the case for particle-in-a-box models, and is easiest to see in the 1D case. Here, the wave functions are $\sqrt{2/L} \sin(n\pi x/L)$, which only depends on the length of the box L , and not on the mass of the particle, for example. Similarly, in a spherical QD, the shape of the envelope wave function depends only on the radius R . So, on the scale of a single

crystal unit cell, the electron and hole wave functions may differ dramatically. But if averaged over a few units cells, then their identical envelope functions will cause the total charge to cancel. Thus, to first order there is nearly complete cancelation of charge within quantum dots, causing the environment to have negligible effect on their excitonic energy spectra.

Nevertheless, the environment can still impact excitons in quantum dots in more subtle ways. For example, in a manner similar to the Casimir force, the contrast of dielectric constants changes the density of states of the electromagnetic field. As a result, the spontaneous emission lifetime is increased by a factor of $(2\varepsilon_m + \varepsilon_{\text{QD}})^2/9\varepsilon_m^{5/2}$, where ε_m is the dielectric constant of the medium and ε_{QD} is that of the quantum dot [10]. This is a factor of 10-20 in lead-salt QDs, and is part of the reason for their long, few microsecond lifetime. In addition, the environment has a dramatic impact on QD properties when it has only a single charge, instead of an exciton. In that case, charge cancelation is impossible, and the full effect of the image charges in the medium are felt. This is important in the case of charge transfer, when charges are individually moved into and out of nanocrystals.

1.3 Organization of the Dissertation

The goal of this dissertation is to explore in more detail these two effects of quantum and dielectric confinement. To study quantum confinement, we will modify either the structure or shape of the nanocrystals, to see how nanocrystal properties can be modified beyond their intrinsic size dependence. Dielectric confinement will be studied primarily by charging the nanocrystal, so that only a single electron or hole exists within it. In all, three systems will be studied.

The first system explored will be that of a core-shell quantum dot. A core-shell QD is a spherical nanocrystal heterostructure of two semiconductor materials, an inner core of one material and an outer spherical shell of another. In this case, depending on the precise nature of each layer, it is possible that the electron and hole may both live together within the core or shell, or they may separate and one occupy each layer. In the latter case, there would be charge separation within the nanocrystal, and interesting Coulomb effects may be noticeable. In this work, a model is developed to describe the specific case of a PbSe core, PbS shell QD, which was recently synthesized [11]. We discover that in most cases, the electron and hole are expected to behave in a novel third manner— extending over both core and shell, mostly ignoring the boundary— but very large sizes will show charge separation with the hole existing primarily in the shell. Comparison is made to experiment and is shown to agree well with both optical and electrical measurements.

The second example explored will be that of elongated, cylindrically shaped nanocrystals, or “nanorods” (NRs). By virtue of their single extended dimension, the electrons and holes have the freedom to separate slightly along the rod axis. As a result, there may no longer be complete charge cancelation in this direction. In this dissertation, we develop a novel synthesis of PbSe NRs and develop a model to describe them. We find that despite these expectations, the electron and hole wavefunctions still have nearly complete overlap, removing the effect of the image potential on the NR energy levels; but that nevertheless the potential still has a dramatic effect on the exciton wavefunction by heavily correlating electron and hole motion along the nanorod axis, with observable effects.

The final case explored will be of a PbS QDs coupled to small organic molecule

charge acceptors. After optical excitation, the electron will travel into the acceptor, causing the nanocrystal to become charged. As a result, the environment has a dominant effect on the dynamics of the charge transfer. Experiments are performed on this model system to try to understand the mechanisms behind this charge transfer, and a model is developed from a modification of Marcus Theory. Both the modeling herein and the experiments performed are the first systematic attempts to understand charge transfer from lead salt quantum dots.

An additional chapter is included at the beginning of the dissertation to describe in detail the process of synthesizing nanocrystals. The results do not constitute any novel scientific material, but the process of building up both the physical infrastructure and the chemical knowledge base within our lab to successfully and robustly produce nanocrystals was a significant undertaking. The purpose of this chapter, then, is not to present material that is new to the scientific community, but rather to present material in a novel manner such that it is accessible for future researchers in our lab, or possibly for other labs trying to similarly gain this capability.

BIBLIOGRAPHY

- [1] Al. L. Efros and A. L. Efros, *Sov. Phys. Semicond.* **16**, 772 (1982).
- [2] F. W. Wise, *Accounts Chem. Res.* **33**, 773 (2000).
- [3] J. D. Jackson, *Classical Electrodynamics Third Edition*, 3rd ed. (Wiley, New York, 1998).
- [4] I. Kang and F. W. Wise, *J. Opt. Soc. Am. B* **14**, 1632 (1997).
- [5] J. M. An, A. Franceschetti, S. V. Dudyi, and A. Zunger, *Nano Lett.* **6**, 2728 (2006).
- [6] G. Allan and C. Delerue, *Mater. Sci. Eng., C* **25**, 687 (2005).
- [7] S. V. Kilina, C. F. Craig, D. S. Kilin, and O. V. Prezhdo, *J. Phys. Chem. C* **111**, 4871 (2007).
- [8] A. Franceschetti, *Phys. Rev. B* **78**, 075418 (2008).
- [9] J. C. Slater, *Phys. Rev.* **76**, 1592 (1959).
- [10] A. Thränhardt, C. Ell, G. Khitrova, and H. M. Gibbs, *Phys. Rev. B* **65**, 035327 (2002).
- [11] E. Lifshitz, M. Brumer, A. Kigel, A. Sashchiuk, M. Bashouti, M. Sirota, E. Galun, Z. Burshtein, A. LeQuang, I. Ledoux-Rak, and J. Zyss, *J. Phys. Chem. B* **110**, 25356 (2006).

CHAPTER 2

QUANTUM DOT SYNTHESIS

2.1 Introduction

Nanofabrication of semiconductors elicits images of gigantic and expensive electron beam or photolithography facilities. But even with state-of-the-art equipment, this type of method cannot reach the 1-10 nm length scales needed for quantum dots. Thus, the nanocrystals must be encouraged somehow to self-assemble. Epitaxial growth using molecular beam epitaxy is commonly used for III-V semiconductors, such as InAs or GaAs, but this method is similarly complex and expensive and also results in a fixed substrate for further experiments. Wet-chemical growth is the preferred method for nanocrystal fabrication, because it combines simplicity, inexpensiveness, and the potential for scaling up to yields on the milligram to (rarely) kilogram scale.

There are three primary goals of a nanocrystal synthesis. First, it should have good control over the size— the QD diameter should be tunable, and the size distribution should be narrow, e.g. $\Delta R/R \lesssim 10\%$. Second, the produced QDs should have high optical quality— quantum yields (QYs) at least above 10%, narrow absorption peaks without evidence of scattering from malformed QD aggregates, and all with long-term stability. Third, the host material should not interfere with experiment or subsequent device fabrication. Attempts to fabricate lead-salt nanocrystals began in the late 80s, but did not succeed in any of these three criteria. Later, the first successful syntheses were of PbS QDs in polymer [1] and glass [2], and PbSe QDs in glass [3]. Though showing good optical quality, and allowing many initial experiments, the host materials in these cases were still to

restrictive.

In 2001, Murray [4] developed a wet-chemical method to easily produce extremely high quality PbSe QDs surrounded by small organic molecules, allowing them to be soluble in organic solvents. Shortly thereafter, the method was also extended to PbS QDs [5]. The QDs produced by these methods satisfy all criteria, with narrow size distribution as small as 5%, excellent long term stability if stored under nitrogen, and the flexibility of a liquid host material.

Unfortunately, most chemical synthesis papers are intended for an experienced audience that is already familiar with the details. But, as is often the case, the details can be crucial for success. So, the purpose of this chapter is to write a more detailed description of lead-salt nanocrystal syntheses, intended for an audience with little relevant background in chemistry. I will focus on the correct techniques only, rather than describing all of our initial missteps, and as often as possible giving explanations for them.

The next sections are organized by first explaining the synthesis setup in detail. Next, a few common procedures relevant to any synthesis are explained. Then the PbS and PbSe NC syntheses are explained along with a summary of results from our lab and sizing curves are presented for reference. Finally, a short troubleshooting section is included with the most common problems encountered, and the chapter is summarized in the conclusions.

2.2 The Synthesis Setup

Nanocrystal synthesis typically needs to be performed in air-free (no water, no oxygen) environments. A robust way to handle this, without the need to put the entire setup inside a nitrogen glove box, is with the use of a Schlenk line, Fig. 2.1.

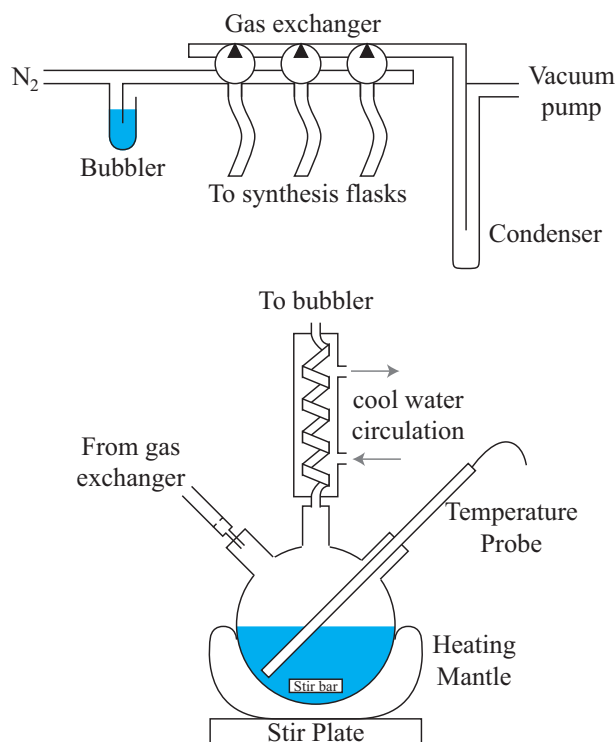


Figure 2.1: A typical Schlenk line setup.

At the top of the figure is the gas exchanger. Its purpose is to easily switch between a fresh nitrogen supply and a vacuum pump, letting the user initially quickly vacuum away the air within their setup, followed by flowing a supply of nitrogen through the setup during the synthesis. In principle, once nitrogen has filled the system, the entire reaction could be performed without any additional flow, but in practice, a realistic gas exchange system will have leaks that will contaminate the N₂ environment slowly over time. So, a steady supply of N₂ is supplied at slightly above atmospheric pressure, so that any leaks will only leak

N₂ out of the system.

Nitrogen enters the gas exchanger on the left of the diagram and goes into the “bubbler,” which is simply a bent piece of glass, filled with an inert and viscous fluid, such as silicone oil or mineral oil. Its purpose is to normalize the pressure inside the gas exchanger to just above atmospheric pressure, by allowing residual pressure to bubble out through the liquid to the air. Without this, one would likely break the fragile glass components that follow with the typically high pressure leaving an N₂ cylinder.

Entering on the right side of the gas exchanger is the vacuum supply. Typically, the vacuum pump is only run when needed, and so this may also have unfiltered air inside it, and caution is needed to prevent accidental contamination of your setup. The vacuum supply proceeds through a condenser, which is used to prevent vaporized chemicals from entering the pump. If one is only vacuuming air from the setup, then the condenser is not used. When used, a dewar of liquid N₂ is placed around the condenser, to re-condense any vaporized chemicals before entering the pump.

The gas exchanger itself follows, and can have from one to many ports below. Each port can independently switch between N₂ and vacuum using the knobs at the top. Depending on the quality of the exchanger, care should be taken when the vacuum pump is on. Because of leaks, a partial vacuum can occur even when the knobs are not placed in the vacuum setting. The most common problems of this type are discussed in a later section.

At the bottom of Fig. 2.1 is an example synthesis 3-neck flask. Entering on the left neck of the flask is the N₂/vacuum from the gas exchanger. It enters usually

with a large gauge (diameter) needle that punctures a rubber sealing septum. Needles are useful because the gauge can be used to determine the amount of N_2 flow, and because longer needles can be inserted directly into the reacting liquid to “bubble” the liquid, which can remove dissolved gaseous impurities. On the top neck is a condenser with optional flowing water cooling, which then proceeds to an oil bubbler (not pictured.) When vacuuming the flask to remove air or other gases, this condenser is disconnected from the bubbler, because the vacuum will suck the bubbler oil into the flask, contaminating your synthesis. During N_2 flow, it is reconnected to the bubbler to allow the N_2 to escape the system in a manner that prevents back-flow of air.

On the right neck of the flask is a temperature probe, which is submerged in the reacting liquid. This is connected to a temperature controller, which is additionally connected to the heating mantle below the flask. Ideally, this can be used to maintain the desired temperature of your reaction. Finally, at the bottom of the flask is a magnetic stir bar and stir plate, which are used to vigorously stir the reaction to maintain uniform concentrations of reactants and uniform temperatures in the reaction liquid.

2.3 Common Themes in Nanocrystal Syntheses

All nanocrystal syntheses are built up out of a few basic types of steps. In fact, there are very few unique procedures that are used in nanocrystal syntheses, and below I will try to summarize many of them. In addition to these few building blocks, it is important to stress *patience*, *cleanliness*, and *careful planning* during all of this.

2.3.1 Creating an N₂ environment

Initially, reaction flasks should only be filled with solid reactants. This is to prevent the need of the condenser on the vacuum pump, because any liquid reactants could vaporize under vacuum and contaminate the pump. After putting all solids into your flask, connecting all tubes in the Schlenk line setup, and *disconnecting* the bubbler from the flask, it is time to prepare the N₂ environment within.

Position the needle from the gas exchanger far from any powders inside the flask, or the vacuuming/N₂ will blow the powder all over your flask. First, turn on the N₂ from the gas cylinder supply. Because the bubbler maintains a constant pressure independent of the flow coming into it, the pressure going to the bubbler is unimportant. The best case is to have only ≈ 1 bubble per second appearing in the bubbler. This will minimize the amount of wasted gas during your experiment. Next, turn on the vacuum pump and switch the exchanger to the vacuum setting and listen for the “hiss” of air flowing out of the flask. Wait for a few seconds after you can no longer hear the hiss, and quickly switch the exchanger to the N₂ setting. The bubbler will stop bubbling as the pressure is equalized in the flask. You will know when the flask is full because the bubbler will begin bubbling again. Repeat this vacuum/N₂ cycle at least three times. Finally, turn off the vacuum pump and use an open port on the gas exchanger to re-fill the vacuum side of the exchanger with room air (relieving the pressure.) Then, reattach the condenser on the flask to the bubbler, which should show obvious bubbling. If you do not see bubbles, then either there is a block in your tubes or you didn't relieve the pressure in the vacuum and leaks in the exchanger are causing a partial vacuum in your flask.

2.3.2 Filling the flask with a liquid reactant

Solid reactants are placed in the flask before vacuuming it, but liquids cannot be, to avoid contaminating the vacuum pump. So, liquids must be added to the reaction flask after the N₂ environment has been created. Thus, it's important not to ruin the N₂ environment while adding the liquid.

The best way to do this involves having a secondary flask (or other simple container) already filled with N₂. Find a syringe that is large enough to hold all of the liquid to be added, and plunge that empty syringe into the secondary flask, and slowly completely fill the syringe with the N₂ a few times, venting the original air in it into a bubbler. In general, before placing a syringe in your reaction flask, it is a good idea to flush it like this.

After flushing it, quickly remove the syringe and place it in your liquid container and suck up the liquid. Turn the syringe upside down so that the air/N₂ bubbles within the syringe float to the top. Push the plunger of the syringe up to remove the residual air/N₂ bubbles, keeping a kimwipe at the tip to collect any liquid that comes out. Continue until a small amount of liquid visibly comes out of the top of the syringe. Now that all air/N₂ is removed from the syringe, it can be pushed into the reaction flask *via* one of the sealing septums, and the liquid slowly pushed into the flask.

It is a good idea to “bubble” the liquid in the reaction flask to remove any dissolved oxygen, by placing the needle that brings the N₂ from the gas exchanger fully into the liquid (but not hitting the stir bar) and letting it visibly bubble the liquid for 5-15 minutes.

2.3.3 Vacuuming during the synthesis

Sometimes, gases are produced due to chemical reactions during your synthesis. A common example is when lead oxide reacts with oleic acid to form lead oleate and gaseous water. This water is known not to interfere greatly with lead-salt syntheses, but for best precision, or in other similar syntheses, one might wish to remove it.

To do so, fill a liquid N₂ dewar and place it around the the vacuum condenser, letting it come to a stable temperature. Then, making sure to remove the connection between the condenser on the flask and the exhaust bubbler, turn on the vacuum pump. Now, the flask can be safely vacuumed. In the case of water, the reaction liquid is typically hot enough to boil the water out of the solution, but the top parts of the flask are often cool enough to let it recondense. You might see droplets of clear liquid forming there. So, vacuuming should proceed as long as it takes to remove these droplets. In general, it isn't unusual for it to take 10-15 minutes of vacuuming to fully remove the (possibly recondensed) gases.

When finished, make sure to relieve the pressure on the vacuum lines after turning off the pump, as mentioned above, before reconnecting the flask condenser to the exhaust bubbler. Once again, this is to prevent an accidental partial vacuum from sucking bubbler oil into your flask.

2.3.4 Preparing reactants over long periods of time

Some reactants require a long period of time to react in a nitrogen environment, such that it becomes impractical to use the Schlenk line. For example, the prepara-

tion of trioctylphosphine selenide is typically performed overnight. In these cases, it is best to use a nitrogen glove box, and prepare a large quantity of the reactant beforehand, from which small aliquots can be taken as needed. The difficulty arises when trying to move this aliquot to the Schlenk line setup to combine with the other reactants. Exposure with air should be minimized during this transportation, so hopefully there is a glove box near your setup.

The best method I found is to use a syringe (disposable or otherwise) sealed within a plastic ziplock bag (possibly multiple bags.) This has been used successfully to bring some samples across campus. The idea being to directly puncture the ziplock bag, straight into the flask of your setup, almost completely removing the time exposed directly to air. Of course, the lead-salt syntheses are so robust, that almost identical success can be had just walking quickly across the room with the syringe exposed to the air (though doing it that way smells much worse!)

2.3.5 Purification of the nanocrystal products

When the synthesis is complete, one is left with a mixture of the produced nanocrystals, leftover un-reacted ingredients, and possibly some badly formed and aggregated nanocrystals. To purify the mixture, we selectively centrifuge the mixture to separate components.

First, a mixture of roughly 1:2 hexane:methanol with a tiny additional amount of butanol is added to the QD solution. The role of the butanol is solely to allow the methanol and hexane to mix together, and only a tiny amount, a few drops to a few mL, is needed. This mixture is added to your QD solution until the solution becomes cloudy, indicating that the nanocrystals have precipitated out of solution

and clumped together.

The purpose of this precipitation is to make them heavy enough to be able to be centrifuged. Individual nanocrystals are too light to be centrifuged, even at the fastest setting, but clumps of precipitated nanocrystals are heavy enough to work. Next, the solution is centrifuged in a large-volume centrifuge at a moderate speed around 1000-2000 rpm for 5-10 minutes. After this, the cloudy solution should become clear, with a black film on the bottom of the centrifuge tube. If not, put it back in for longer/faster or add more methanol and try again.

The clear solution is dumped out of the tubes and disposed, being careful not to accidentally dump any of the black film (although losing a few nanocrystals is much preferable to leaving impurities in the solution.) The tubes are left upside down on top of a kimwipe, allowing the residual viscous solution to drain for a minute or two. After this, a small amount (~ 5 mL) of toluene is added to the centrifuge tube, which should easily redissolve the black film into a brownish solution. At first, a gentle shaking can help it redissolve, but a vortexer can be used for the impatient. Keep adding toluene until all the black film is dissolved into the solution.

It is a good idea, though probably optional, to repeat the precipitation / centrifugation process again once or twice at this point to further purify the solution. We have anecdotal evidence that impurities remain until repeated at least twice more, but there is always a small risk of damaging the QDs with each successive precipitation. If repeated, one needs only add methanol to precipitate the QDs, hexane and butanol can be avoided now.

After having repeated the precipitation and redissolving, one is left with a brownish solution in toluene. At this point, we have likely removed all of the un-

reacted ingredients (because they were light enough to be dumped out with the clear solution), though any clumps of badly formed QDs still remain in solution. To remove these, place the brown solution back into the centrifuge (without precipitating!) and run it at nearly its fastest setting. The nanocrystal aggregates are now heavy enough to fall out of solution, while the good nanocrystals are not. When finished, slowly pour or pipette out the brown solution, being careful not to touch or disturb the likely black film on the bottom of the centrifuge tube. This time, we keep the brown solution and dispose of the black film on the centrifuge tube. This process does not need to be repeated, but can be repeated just to verify its success.

2.4 PbS Quantum Dot Synthesis

The synthesis of PbS QDs is adapted from the method in Ref. [5]. Table 2.1 summarizes the chemicals needed for a typical PbS QD synthesis. All chemicals are purchased from Sigma-Aldrich.

Table 2.1: Chemicals needed for a typical synthesis of PbS QDs.

Name, (purity)	Abbr.	Amount	(g/mol)	(g/mL)
Lead (II) Oxide, (99.999%)	PbO	220 mg	223.20	9.64
Oleic Acid, (90%)	OA	0-10 mL	282.46	0.895
1-Octadecene, (90%)	ODE	5-15 mL	252.48	0.789
Bis(trimethylsilyl)sulfide, (syn. grade)	TMS	105 μ L	178.44	0.846

In order to make PbS QDs with an absorption peak around 1200 nm, 220 mg of PbO are weighed and placed within a 100 mL flask. This 100 mL flask and one 25 mL flask are prepared with an N₂ environment. A mixture of 5.5 mL OA and 4.5 mL ODE are injected into the 100 mL flask, while gently stirring. The temperature is then raised to 130°C. Over the next 5-10 minutes, as the temperature increases,

the solution will change from yellow (the color of PbO) to clear (the color of Pb-Oleate). After turning clear, the solution is bubbled with N₂ gas for 10 minutes, while maintaining stirring. After this, the bubbling needle is removed and the temperature is lowered to the final reaction temperature of 100°C, and allowed to stabilize.

Simultaneously, 5 mL of ODE is loaded into a syringe and injected into the 25 mL flask with gentle stirring. The temperature of this flask is then raised to the final reaction temperature of 100°C and allowed to stabilize.

While the temperature of both flasks is stabilizing, an ice bath (bucket filled with ice and tap water) is prepared. When all of this is ready, 105 μL of TMS is carefully injected into the 25 mL flask, and allowed to mix with the ODE for a few seconds, while the TMS bottle is immediately returned to its inert storage container. Then, with a syringe that has been flushed with N₂, the ODE+TMS mixture is rapidly injected into the 100 mL flask under vigorous stirring. Within seconds, the solution should change to a dark brown or black, indicating the formation of PbS nanocrystals.

The solution is left to cook for 1-5 minutes, and the precise time is unimportant. The PbS QDs rapidly reach their final size within 10-30 seconds, and then are stable for up to 30 minutes of reaction time afterwards, with minimal spectral shifting. For best reproducibility, 3 minutes cooking time is suggested.

Finally, the flask is removed from the heating mantle, and placed in the ice bath, while still under N₂ flow. This is most easily achieved by having the mantle on an adjustable height stand, which can be lowered to remove the heater, and then raised again with the ice bath.

After reaching room temperature, and before going too far below, the solution is removed from the ice bath, the N₂ shut off, and the solution removed by syringe into two 50 mL centrifuge tubes. Around 15 mL of hexane is added to each tube, followed by around 1 mL of butanol, followed by around 25-50 mL of methanol. The methanol is slowly added until the QDs visibly precipitate and is immediately stopped afterwards. The typical purification routine is then performed, as described previously, and the finished QDs are stored either as a dried solid powder or in solution for convenience within a nitrogen glove box. It is important to put them in storage within minutes or hours of finishing the synthesis— even one day in open air can cause degradation.

To adjust the size of the QD, the amount of OA and the reaction temperature are adjusted. In general, if x mL of OA is used, then $10 - x$ mL of ODE is used, to keep the concentration of Pb-oleate the same. With our current equipment, I was never able to achieve reproducibility in the QD absorption peak better than ± 50 nm. If one is really striving for reproducibility, then following all of the above and additionally adding steps like vacuuming the Pb-Oleate solution, and likely purchasing a newer, more accurate temperature controller are necessary. Because of this lack of perfect reproducibility, the final size of QDs also depends on who is performing the synthesis, so I recommend to the reader to try it themselves a few times to calibrate it for yourself.

As a guide, though, the following formula would typically put me within 50 nm of the predicted absorption peak wavelength

$$\text{Abs. peak (nm)} = 110 + \frac{1240}{1.11 \exp(-mL/9.4) + 0.947 - 0.00441T} \quad (2.1)$$

where T is the reaction temperature and mL is the amount of oleic acid in mL. I would typically perform one synthesis with these parameters, using the resulting

absorption peak wavelength to calibrate my next attempt. A followup attempt would typically get within 25 nm of the goal. Remaining under ~ 10 mL OA and T within 80-150°C is recommended.

At the extreme limit of this synthesis, particles with an absorption peak in the visible can be created. A single synthesis was performed at room temperature, producing PbS QDs with a bandgap around 515 nm and visible red emission at ≈ 700 nm. Though unlike small PbSe clusters, they had poor quantum yield and proved to be unstable, within days having red shifted over a hundred nanometers. Though untested, it might be possible to cap these very small nanocrystals with CdS to improve their long-term stability and quantum yield [6]. The upper limit to synthesized QD size was not explored, because our use of InGaAs detectors prevents characterization of these samples when they emit above 1750 nm.

The concentration of the synthesized QDs can be determined in many ways, though the simplest method is to use the known extinction coefficient [7, 8] of PbS QDs to extract the concentration from a simple absorption measurement. This is particularly simple because at high energy the absorption spectra of all sizes of QDs converge to the bulk absorption spectrum, so one can determine the concentration simply from a single value of the absorption at high energy. Specifically, the following formula from Ref. [7] can be used:

$$C_{\text{mass}} = 0.375 \times A_{400} \text{ (mg/mL)} \quad (2.2)$$

$$C_{\text{molar}} = \frac{156}{d^3} \times A_{400} \text{ (\mu M)} \quad (2.3)$$

where A_{400} is the absorbance at 400 nm (base-10 logarithm convention), d is the diameter of the QD in nanometers, and a standard cuvette path length of 3 mm is assumed. To modify for other sample thicknesses, both of these concentrations are inversely proportional to the path length.

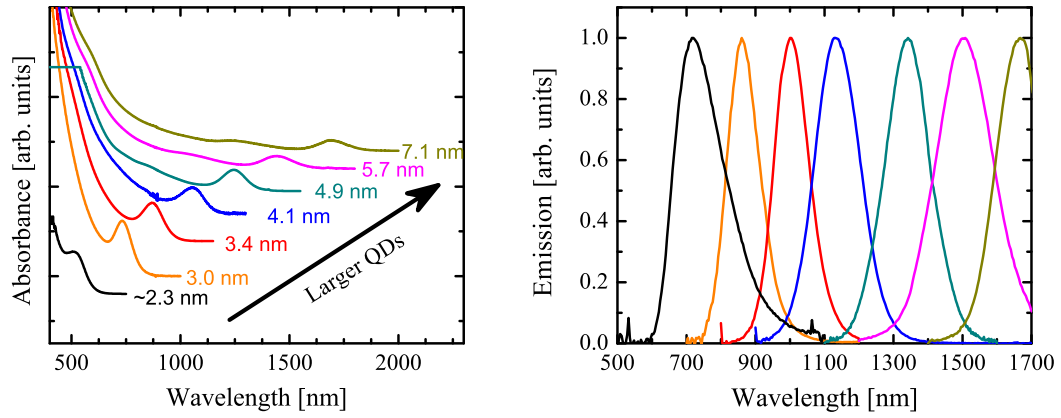


Figure 2.2: Absorption and emission spectra of typical sizes of synthesized PbS QDs.

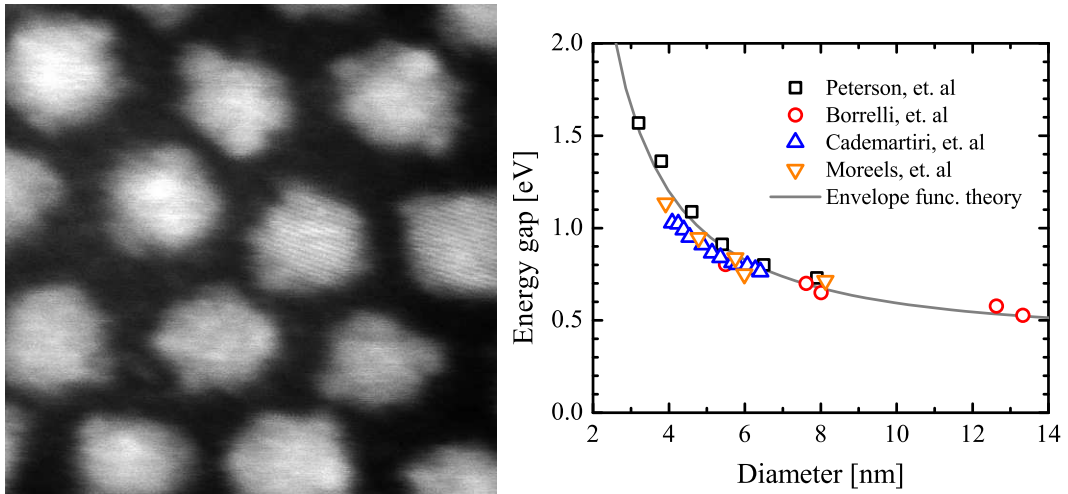


Figure 2.3: (a) STEM image of PbS QDs as synthesized in our lab (full picture width or height is 31.5 nm). (b) Relation between diameter and optical energy gap of PbS QDs. TEM data from Refs. [2, 8, 7] and STEM data from Ref. [9] are shown, along with the prediction from a 4-band envelope function theory calculation.

Fig. 2.2 shows a typical range of the as-synthesized absorption and emission spectra of PbS QDs. Fig. 2.3 shows an example STEM image of PbS QDs synthesized in our lab, and a comparison of the theoretical and experimental size dependence of the QD energy gap. For reference, the size dependence of the energy gap is best fit with the following formula:

$$E_g = 0.41 + 6.31d^{-1.54} + 2.42d^{-3} \quad (2.4)$$

where the energy gap is expressed in eV and the quantum dot diameter in nanometers.

2.5 PbSe Quantum Dot Synthesis

The synthesis of PbSe QDs [4] proceeds in a nearly identical fashion to that of PbS QDs, but with two important distinctions. First, the initial selenium precursor needs at least 12 hours to be created, and is typically done overnight. Second, the duration of the synthesis is now important, and is a convenient method for controlling particle size. From one nanocrystal synthesis, multiple sizes of quantum dots can be created. The chemicals needed for the synthesis are listed in Table 2.2. It is important to get precisely 90% pure trioctylphosphine from Fluka, as some groups have reported worse yield using *more* pure TOP. Other chemicals are purchased from Sigma-Aldrich. As always, if you find a good batch of TOP, or any other chemical, consider buying many more bottles of the same lot.

The day before the synthesis, 0.79 g of Se is dissolved in 10 mL of TOP in a glove box and stirred overnight. Only a small part of this solution will be used, and the rest can be stored for weeks without noticeable degradation. In a typical synthesis, 330 mg of PbO, 1.9 mL of OA, and 10 mL of ODE is combined in a 100 mL flask

Table 2.2: Chemicals needed for a typical synthesis of PbSe QDs.

Name, (purity)	Abbr.	Amount	(g/mol)	(g/mL)
Lead (II) Oxide, (99.999%)	PbO	330 mg	223.20	9.64
Oleic Acid, (90%)	OA	0-10 mL	282.46	0.895
1-Octadecene, (90%)	ODE	5-15 mL	252.48	0.789
Selenium powder, (99.5%, 100 mesh)	Se	0.79 g	78.96	4.81
Trioctylphosphine, (90%)	TOP	10 mL	370.64	0.831
Diphenylphosphine, (90%)	DPP	80 μ L	186.19	1.071

in a similar manner as for the PbS QD synthesis. The temperature is raised to 130°C for 30 minutes while stirring, forming the clear Pb-oleate precursor. Then the temperature is changed to the reaction temperature, typically from 110-180°C and allowed to stabilize. 4.5 mL of the TOP-Se solution is drawn into a syringe, removed from the glove box, and injected into the flask during vigorous stirring. Aliquots are removed every 30 s, or other desired growth times, and rapidly cooled in small vials of hexane within an ice bath. The cooled QD solutions are purified in an identical manner as for PbS QDs.

For an unknown reason, adding diphenylphosphine to the TOP-Se solution dramatically increases the number of produced nanoparticles, without any apparent negative repercussions. Typically a molar ratio of 0.3 DPP:Pb would produce around 8x more QDs. So, if desired, 80 μ L of DPP can be mixed with the 4.5 mL of TOP-Se before injection.

There is one final, and crucial problem that occurs during PbSe NC synthesis, and is seen most easily in the resulting emission spectra of the NCs. In Fig. 2.4, the QD spectra produced by a synthesis at 140°C is shown as a representative case. The emission spectra shows two peaks for all but the longest growth time— that is, there are two sizes of QDs in the solution. This is because the growth of the QDs proceeds by first nucleating small PbSe clusters, which brightly emit around 800

nm, and then these clusters group together to form the larger PbSe QDs. Over time, the supply of these clusters runs out, as evidenced by the decreasing size of the emission peak at 800 nm. I did not find a systematic way to avoid these clusters, besides waiting long enough to exhaust their supply. The amount of time requires to wait depends also on what temperature the reaction is performed at and the amount of DPP added. No systematic work was done on understanding or predicting this time, and the only recommendation is to take aliquots every minute and only use those that do not emit at 800 nm. It may be possible to carefully use size-selective precipitation to remove the smaller particles, but this is untested. Additionally, the extra narrow peak in the absorption at around 1380 nm is an artifact from either excess toluene or oleic acid, and could be removed with further purification; this data was chosen specifically because it shows this problem.

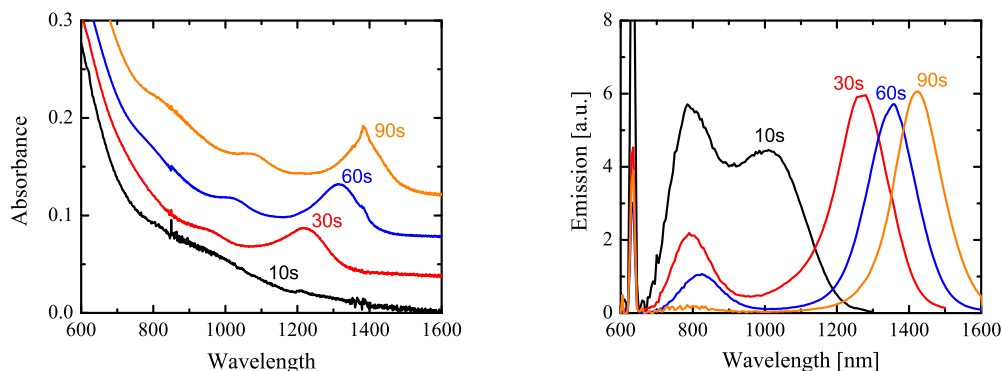


Figure 2.4: Absorption and emission spectra from a synthesis of PbSe QDs at 140°C for various growth times.

Only a handful of PbSe syntheses were ever performed in our lab, primarily because PbS covers the same IR spectral range while going further towards the visible spectrum (into the important silicon detector range), offers a higher electron affinity for easier electron transfer (explained in a later chapter), and has nearly identical chemical processing capability (ligand exchange, etc.) As a result, specific growth times and temperatures needed to produce exact particle sizes are not

known for our lab. Still, because multiple sizes are made within one NC synthesis, all that is needed is a rough estimate of the reaction temperature, and then one of the aliquots taken will likely produce the desired QD size. If taking aliquots every 30s, for a total of 5-6 different sizes, then the following table gives a summary of suggested temperatures for different particle size ranges. The reader is strongly encouraged to read Refs. [4, 10] for additional information, including the effect of various chemical impurities on the synthesis.

Table 2.3: Suggested temperatures for various QD absorption peak ranges for PbSe NC syntheses.

Temperature ($^{\circ}\text{C}$)	Absorption peak range (nm)
140	1200-1400
150	1400-1700
160	1700-2100

The concentration of the synthesized QDs can be determined in the same simple manner as for PbS QDs, explained previously, using the extinction coefficient in Ref. [11]. This produces the following formula:

$$C_{\text{mass}} = 0.337 \times A_{400} \text{ (mg/mL)} \quad (2.5)$$

$$C_{\text{molar}} = \frac{132}{d^3} \times A_{400} \text{ (\mu M)} \quad (2.6)$$

where again, A_{400} is the absorbance at 400 nm (base-10 logarithm convention), d is the diameter of the QD in nanometers, and a standard cuvette path length of 3 mm is assumed. To modify for other sample thicknesses, both of these concentrations are inversely proportional to the path length.

Fig. 2.5 shows the literature values for the dependence of absorption peak on nanocrystal size, compared with the $\mathbf{k} \cdot \mathbf{p}$ prediction with the parameters from Ref. [12] and with parameters chosen to best fit the trend (see Appendix B.4). For reference, the size dependence of the energy gap is best fit with the following

formula:

$$E_g = 0.28 + 4.43d^{-1.34} + 0.555d^{-4.62} \quad (2.7)$$

where the energy gap is expressed in eV and the quantum dot diameter in nanometers.

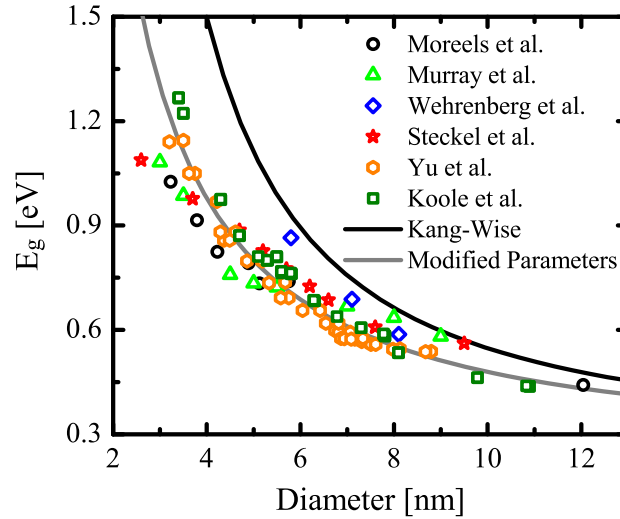


Figure 2.5: Literature values [4, 11, 13, 14, 15, 16] of the first absorption peak in PbSe QDs versus size compared to calculations using the band parameters from Ref. [12] and band parameters chosen to best fit the trend (see Appendix B.4).

2.6 Troubleshooting Common Problems

In this section, I'll briefly mention a few common problems and rules of thumb that appear during nanocrystal synthesis. The points are very loosely organized and are intended to just be a list of things to consider.

Stir solutions vigorously. Bad size distributions are often the result of not stirring fast enough, though it is possible for the entire synthesis to fail. The faster one stirs, the more uniformly distributed the reactants are during the reaction. In

general, stir as quickly as is possible, without drastically splashing the solution.

Measure viscous liquids by mass, not volume. The viscosity prevents pipettes from working accurately, so it is best to fill up a container on a scale in order to measure a specific volume. The most common example is Oleic Acid.

Problem: Oil is sucked into the reaction flask. Remove the bubbler attached to the flask during vacuuming! And do not reattach it until the pressure in the vacuum lines is released.

Problem: Solution doesn't precipitate. If methanol does not work, try acetone. In general, acetone will precipitate more easily, but it can more easily cause damage. Acetone is primarily useful for the smallest QDs, as these are especially difficult to precipitate.

Problem: Solution doesn't turn clear. If the solution remains yellow (the color of lead oxide), then one of two things is at fault. Either your chemicals have gone bad (likely the oleic acid as lead oxide is very stable) or you did not have an inert environment in the flask, i.e. there was a leak. Make sure that the bubblers are bubbling and that there isn't a block in the N₂ lines somewhere. If you cannot find a leak, buy new chemicals.

Problem: Solution doesn't turn brown. Don't panic and try the synthesis again. If it fails twice in a row, then the most likely culprit is that the TMS chemical has gone bad. Typical shelf life in a desiccator filled with N₂ is 3-6 months.

Problem: Too much temperature fluctuation. Using wool fibers, wrapped around the flask like a blanket can greatly increase stability. You should be able to get $\approx 0.1^\circ\text{C}$ stability. If not, clean the temperature probe and try it on

a moderate volume (≈ 20 mL) of pure ODE to see if the controller is at fault.

2.7 Conclusions

An air-free Schlenk line synthesis setup has been built and described here, with care given to detailing many of the subtleties in nanocrystal synthesis. Using the setup detailed above, lead salt nanocrystals have been fabricated successfully. Lead sulfide QDs were produced in the size range from 3-7 nm, with bandgaps from 530-1800 nm, and emission from 700-1750 nm (emission longer than 1750 nm was not recorded with our InGaAs detector.) The synthesis procedure was optimized to produce the narrowest size distribution and smallest line widths in absorption and emission. PbSe QDs were successfully synthesized, but not thoroughly studied, with sizes from 4-5 nm. Other sizes could be made simply using the above procedure. Though not detailed here, the setup has also been used successfully to synthesize CdSe (see appendix A.1), CdTe, Au, TiO₂, ZnO, and SnO₂ nanoparticles, demonstrating its versatility and the commonality of the mentioned building block procedures.

BIBLIOGRAPHY

- [1] M. T. Nenadovic, M. I. Comor, V. Vasic, and O. I. Micic, *J. Phys. Chem.* **94**, 6391 (1990).
- [2] N. F. Borrelli and D. W. Smith, *J. Non-Cryst. Sol.* **180**, 25 (1994).
- [3] A. Lipovskii, E. Kolobkova, V. Petrikov, I. Kang, A. Olkhovets, T. Krauss, M. Thomas, J. Silcox, F. Wise, Q. Shen, and S. Kycia, *Appl. Phys. Lett.* **71**, 3406 (1997).
- [4] C. B. Murray, S. Sun, W. Gaschler, H. Doyle, T. A. Betley, and C. R. Kagan, *IBM J. Res. Dev.* **45**, 47 (2001).
- [5] M. Hines and G. Scholes, *Adv. Mater.* **15**, 1844 (2003).
- [6] J. M. Pietryga, D. J. Werder, D. J. Williams, J. L. Casson, R. D. Schaller, V. I. Klimov, and J. A. Hollingsworth, *J. Am. Chem. Soc.* **130**, 4879 (2008).
- [7] I. Moreels, K. Lambert, D. Smeets, D. De Muynck, T. Nollet, J. C. Martins, F. Vanhaecke, A. Vantomme, C. Delerue, G. Allan, and Z. Hens, *ACS Nano* **3**, 3023 (2009).
- [8] L. Cademartiri, E. Montanari, G. Calestani, A. Migliori, A. Guagliardi, and G. A. Ozin, *J. Am. Chem. Soc.* **128**, 10337 (2006).
- [9] J. J. Peterson, Ph.D. thesis, University of Rochester, 2007.
- [10] A. J. Houtepen, R. Koole, D. Vanmaekelbergh, J. Meeldijk, and S. G. Hickey, *J. Am. Chem. Soc.* **128**, 6792 (2006).
- [11] I. Moreels, K. Lambert, D. De Muynck, F. Vanhaecke, D. Poelman, J. C. Martins, G. Allan, and Z. Hens, *Chem. Mater.* **19**, 6101 (2007).
- [12] I. Kang and F. W. Wise, *J. Opt. Soc. Am. B* **14**, 1632 (1997).
- [13] B. L. Wehrenberg, C. Wang, and P. Guyot-Sionnest, *J. Phys. Chem. B* **106**, 10634 (2002).
- [14] J. Steckel, S. Coe-Sullivan, V. Bulovic, and M. Bawendi, *Adv. Mater.* **15**, 1862 (2003).

- [15] W. W. Yu, J. C. Falkner, B. S. Shih, and V. L. Colvin, *Chem. Mater.* **16**, 3318 (2004).
- [16] R. Koole, G. Allan, C. Delerue, A. Meijerink, D. Vanmaekelbergh, and A. Houtepen, *Small* **4**, 127 (2008).

CHAPTER 3

CORE-SHELL QUANTUM DOTS

3.1 Introduction

A natural extension from single material nanostructures, hereafter referred to as “core” structures, is to heterostructures with other semiconductors. Core-shell QDs, spherical QDs surrounded by a thin second material layer, have had major impact owing to their ability to increase quantum yield and stability [1]. These properties are attributed to confinement of the exciton states to the core of the QD, away from interfering effects at the surface. Successful syntheses of core-shell QDs have been demonstrated for various combinations of CdSe, CdTe, ZnS, and InAs [1, 2, 3, 4]. In addition, the first PbSe/PbS core-shell structures were recently reported [5]. Despite strong motivation to understand core-shell structures thoroughly, theoretical treatments of their electronic structure are still relatively scarce. Envelope function calculations have been applied to CdX/HgX [6], and atomistic calculations have been performed on CdSe/CdX [7]. Of course, due to the specific band structure of these materials, neither analysis is applicable to nanostructures of the lead-salts.

In this chapter we will analyze the electronic structure of PbSe/PbS core-shell QDs. The energy levels and wavefunctions are calculated by extending a 4-band envelope function theory across the PbSe/PbS material boundary. Contrary to expectations, the exciton wavefunctions are not localized within the PbSe core of the structure. Instead, two types of behavior are found, depending on the size of the QD. For small (3-10 nm outer diameter) QDs, the wavefunction extends into both material layers, causing it to behave similarly to core QDs. In larger

($\gtrsim 14$ nm outer diameter) QDs, the material barrier becomes more important. The lowest unoccupied molecular orbital (LUMO) is then localized in the core, while the highest occupied molecular orbital (HOMO) is delocalized. Optical absorption and electrical tunneling measurements are performed on core-shell QDs in the small size regime and the results agree with the prediction of weak core confinement.

3.2 Theory

PbS and PbSe have a simple cubic crystal structure with nearly identical lattice constants (5.93 Å and 6.12 Å at 300K, respectively), which facilitates the formation of heterostructures. They also have similar band structures, with a direct band gap at eight equivalent L points in the Brillouin zone. The bottom of the conduction band has L_6^- symmetry and the top of the valence band has L_6^+ symmetry in the double group notation, and there is a two-fold spin degeneracy in both levels. The band gaps of PbS and PbSe at 300K are 0.41 eV and 0.28 eV, respectively, but their relative energy offset is not known experimentally. The offset has been predicted numerically to be 0.09 eV for low temperatures [8], and we will use this value. We will also show that our main results are not sensitive to the precise value of this parameter. The arrangement of the band gaps is summarized in Fig. 3.1.

Our theory is derived from the core QD envelope function theory by Kang and Wise [9], which uses a bulk $\mathbf{k} \cdot \mathbf{p}$ Hamiltonian [10]. Bloch states of the lowest conduction and topmost valence bands with spin degeneracy are included, so it is a four-band Hamiltonian. Equations are derived within a slowly-varying envelope approximation and recast into Schrodinger-like equations with effective masses determined by the curvature of the bands. The band structure around the L points

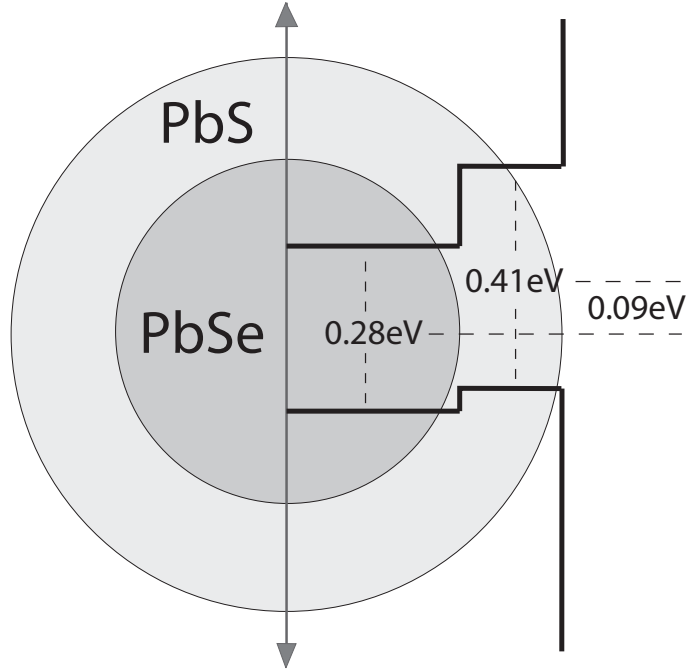


Figure 3.1: Energy gaps in PbSe/PbS core-shell QDs.

in the lead-salts has a slight anisotropy, and thus the exact four-band Hamiltonian should have direction-dependent band parameters. But this anisotropy precludes analytic solutions in a sphere, so we use an approximate isotropic Hamiltonian. The impact of this approximation has been considered previously in core QDs [9, 11], and in the cases of PbS and PbSe is a good approximation.

The parameters of the effective mass model change discontinuously across the PbSe/PbS boundary, and so it is necessary to determine the correct boundary conditions across it. Many different self-consistent choices of boundary condition are possible, and these can lead to conflicting and sometimes unphysical results. Burt has provided a method to construct Hamiltonians across abrupt interfaces [12], which removes this uncertainty in boundary condition. Burt's approach has been successfully applied to other quantum dot systems previously [6]. Applying

Table 3.1: Bulk Band Parameters.

	PbSe	PbS
E_g (eV, 300K)	0.28	0.41
m/m^-	3.9	2.5
m/m^+	6.9	3.0
$2P^2/m$ (eV)	$2.6 \approx 2.55$	$2.5 \approx 2.55$

this method to the 4-band lead-salt model produces the Hamiltonian of Eq. 3.1.

$$\hat{H} = \begin{bmatrix} |L_6^- \uparrow\rangle & |L_6^- \downarrow\rangle & |L_6^+ \uparrow\rangle & |L_6^+ \downarrow\rangle \\ \left(\frac{E_g(r)}{2} - \nabla \cdot \left(\frac{\hbar^2}{2m^-(r)} \nabla \right) \right) \mathbf{1} & & \frac{\hbar P}{mi} \sigma \cdot \nabla & \\ \frac{\hbar P}{mi} \sigma \cdot \nabla & & - \left(\frac{E_g(r)}{2} - \nabla \cdot \left(\frac{\hbar^2}{2m^+(r)} \nabla \right) \right) \mathbf{1} & \end{bmatrix} \quad (3.1)$$

To include the effect of the band offsets, we solved the modified equation $(\hat{H} + \Delta(r))\Psi = E\Psi$, where $\Delta(r)$ is the offset. We used the convention that $\Delta(r) = 0$ in the PbSe core of the QD, since the function is defined only up to an overall constant. The constant energy shift in either material does not change the functional form of the wavefunctions, but does influence the energy eigenvalues. For simplicity, we took the Kane momentum P to have the same value in both materials, since it varies by only a few percent and is within experimental uncertainty. The band parameters are summarized in Table 3.1.

The form of the Hamiltonian uniquely determines the boundary conditions at the PbSe/PbS interface from continuity, but there are still two choices for the boundary condition on the outside of the shell: an infinite potential well or a third material. Infinite potential barriers artificially increase the confinement energies of the states, forcing one to shift the energy levels in an *ad hoc* way in order to match experimental data. Using a third material as a finite barrier is more desirable, but is also problematic because the model parameters in this material are often unknown or ill-defined. PbSe/PbS QDs are typically capped by oleic acid and dispersed in solvents such as chloroform or hexane, and since neither is a crystal,

they do not have well-defined band parameters. As a compromise, we chose to use free-electron masses in the outside material, while leaving the energy gap as a free parameter. Fitting the model to experimental data set the energy gap to roughly 5 eV. Qualitative trends in the results are completely insensitive to this value.

3.3 Solutions

The solutions to these equations are similar to the solutions in a core quantum dot. Because the band parameters in the core-shell structure only depend on the radial coordinate r , the solutions are eigenfunctions of total angular momentum j , its z-component m , and parity π . Thus, depending on parity, these solutions have the form of Eq. 3.2 or 3.3.

$$\psi_{\pi,j,m} = \begin{bmatrix} i f_l(r) \begin{pmatrix} \sqrt{\frac{l+m+1/2}{2l+1}} Y_l^{m-1/2} \\ \sqrt{\frac{l-m+1/2}{2l+1}} Y_l^{m+1/2} \end{pmatrix} \\ f_{l+1}(r) \begin{pmatrix} \sqrt{\frac{l-m+3/2}{2l+3}} Y_{l+1}^{m-1/2} \\ -\sqrt{\frac{l+m+3/2}{2l+3}} Y_{l+1}^{m+1/2} \end{pmatrix} \end{bmatrix},$$

$$j = l + 1/2, \quad \pi = (-1)^{l+1}, \quad (3.2)$$

$$\psi_{\pi,j,m} = \begin{bmatrix} i g_{l+1}(r) \begin{pmatrix} \sqrt{\frac{l-m+3/2}{2l+3}} Y_{l+1}^{m-1/2} \\ -\sqrt{\frac{l+m+3/2}{2l+3}} Y_{l+1}^{m+1/2} \end{pmatrix} \\ g_l(r) \begin{pmatrix} \sqrt{\frac{l+m+1/2}{2l+1}} Y_l^{m-1/2} \\ \sqrt{\frac{l-m+1/2}{2l+1}} Y_l^{m+1/2} \end{pmatrix} \end{bmatrix},$$

$$j = (l + 1) - 1/2, \quad \pi = (-1)^l. \quad (3.3)$$

In Eqs. 3.2 and 3.3, the radial functions $f_i(r)$ and $g_i(r)$ are superpositions of Bessel and modified Bessel functions of the first and second kind. Only Bessel functions that are well-behaved at the origin are allowed in the core of the QD,

while only exponentially-decaying solutions are allowed in the outermost region. In each region, if the energy is outside the local bulk energy gap, then both Bessel and modified Bessel functions are allowed; but if the energy falls within the gap, only modified Bessel functions are allowed. These rules are summarized in Eqn. 3.4.

$$\begin{aligned}
f_l, g_l &= \begin{cases} ai_l(\lambda_1 r) + bi_l(\lambda_2 r) & |E - \Delta| < E_g/2 \\ +ck_l(\lambda_1 r) + dk_l(\lambda_2 r) & \\ \\ aj_l(kr) + bi_l(\lambda_1 r) & |E - \Delta| > E_g/2 \\ +cn_l(kr) + dk_l(\lambda_1 r) & \end{cases} \\
f_{l+1}, g_{l+1} &= \begin{cases} ei_{l+1}(\lambda_1 r) + fi_{l+1}(\lambda_2 r) & |E - \Delta| < E_g/2 \\ +gk_{l+1}(\lambda_1 r) + hk_{l+1}(\lambda_2 r) & \\ \\ ej_{l+1}(kr) + fi_{l+1}(\lambda_1 r) & |E - \Delta| > E_g/2 \\ +gn_{l+1}(kr) + hk_{l+1}(\lambda_1 r) & \end{cases} \quad (3.4)
\end{aligned}$$

Inserting this ansatz into the differential equation produces the energy dispersions in Eqs. (3.5,3.6). When the energy falls outside the energy gap, both equations have a single real root (k, λ_1) . In contrast, when the energy is inside the gap, Eqn. 3.6 has two real roots $(\lambda_{1,2})$, while Eqn. 3.5 has none. This is reflected in our choice of Bessel functions in Eqn. 3.4.

$$\left[\frac{E_g}{2} + \frac{\hbar^2 k^2}{2m^-} - E(k) \right] \left[-\frac{E_g}{2} - \frac{\hbar^2 k^2}{2m^+} - E(k) \right] = \frac{\hbar^2}{m^2} P^2 k^2 \quad (3.5)$$

$$\left[\frac{E_g}{2} - \frac{\hbar^2 \lambda_i^2}{2m^-} - E(\lambda_i) \right] \left[-\frac{E_g}{2} + \frac{\hbar^2 \lambda_i^2}{2m^+} - E(\lambda_i) \right] = -\frac{\hbar^2}{m^2} P^2 \lambda_i^2 \quad (i = 1, 2) \quad (3.6)$$

Inserting the ansatz into the differential equation also relates pairs of coefficients a and e , b and f , etc. This leaves eight undetermined coefficients with the energy E , which are fixed (up to normalization) by the eight boundary conditions. The equations can be set up in a matrix, with the energy levels found by setting the

8x8 determinant to zero.

3.4 Discussion

We calculated multiple energy levels, but found that the properties of the solutions are best summarized by looking at only the LUMO and HOMO states. As a result, we will focus on those two states here. A variety of core and shell sizes were considered, and a summary of these calculations is shown in Fig. 3.2. In these graphs, the numerical value of the energy levels is less important than the trends that they exhibit. When holding the shell thickness fixed, the energy levels behave similarly to those of core QDs (Fig. 3.2a). With the outer diameter fixed, increasing the core size produces an entirely different trend – both the LUMO and HOMO states move down in energy, which causes the transition energy between those states to be roughly constant (Fig. 3.2b). These results imply a simple rule of thumb for this system – the transition energies are primarily determined by the outer diameter.

At first, this may seem surprising. The PbSe/PbS ordering of the layers was chosen so that the wavefunctions would be confined within the core of the QD. If that were the case, one would expect precisely the opposite trends; specifically, if the wavefunction must squeeze almost entirely into the core, then the size of the core alone should set the energy levels. Because this is not the observed trend, the calculated energy levels suggest that the wave functions are not confined to the core of the structure.

Looking more closely at the envelope functions of the solutions, this suggestion is found to be correct in small (3-10 nm outer diameter) QDs, but begins to break

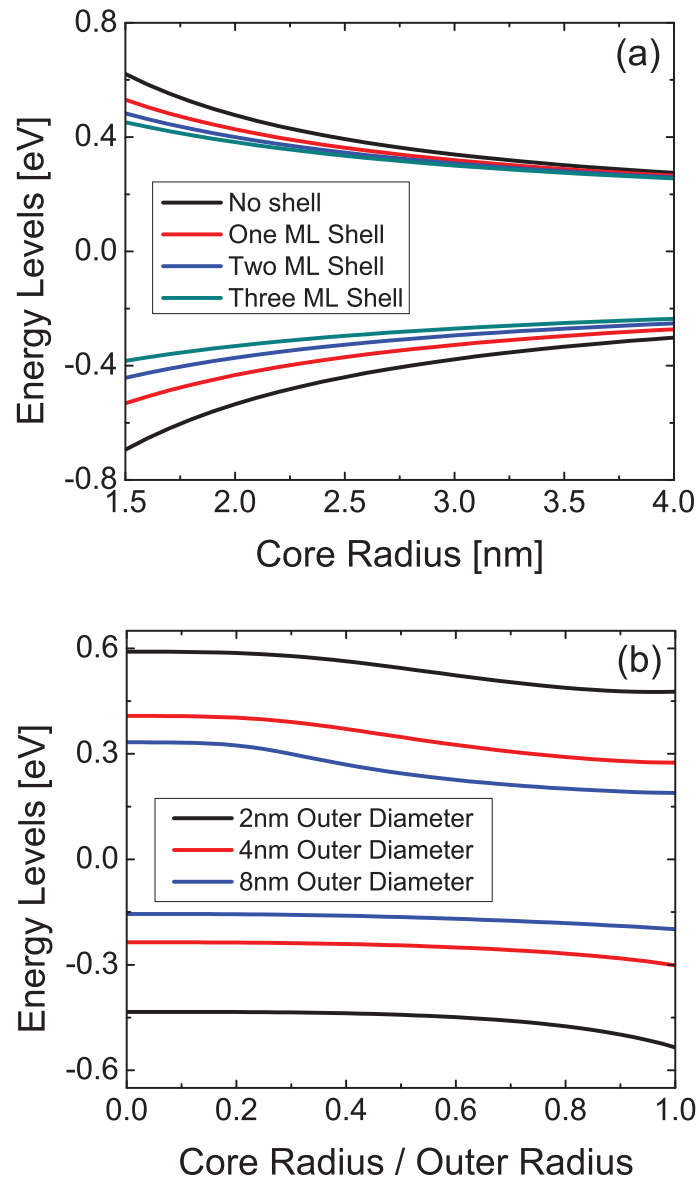


Figure 3.2: LUMO and HOMO energy levels of PbSe/PbS QDs with (a) fixed shell thickness and (b) fixed outer diameter.

down in large ($\gtrsim 14$ nm outer diameter) QDs. As an example of the small size regime, Fig. 3.3 demonstrates how the envelope function changes while increasing the shell thickness for constant core size. The wavefunction extends into the shell with a slight discontinuity in the slope due to the abrupt change in effective mass, but otherwise ignores the material boundary. Thus, it is not surprising that the energy levels are mainly determined by the outer diameter.

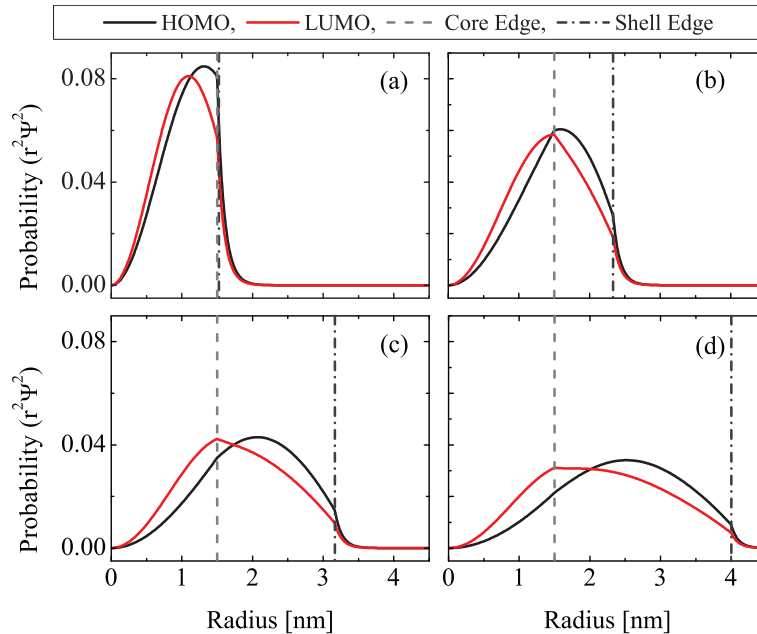


Figure 3.3: Wavefunctions for a constant 3 nm diameter core and variable shell thickness of (a) 0.0 nm, (b) 0.83 nm, (c) 1.67 nm, (d) 2.5 nm.

On the other hand, Fig. 3.4 indicates that larger structures behave quite differently. The LUMO state remains bound in the core as the shell thickness is increased, while the HOMO state extends into the shell just as in small QDs. This causes the LUMO energy to be mainly determined by the core size, and the HOMO energy by the total size. If the size is increased further, the LUMO state becomes even more strongly bound to the core.

This change in behavior with increasing size is determined by the position of the bulk energy gaps relative to the QD energy levels. When the energy lev-

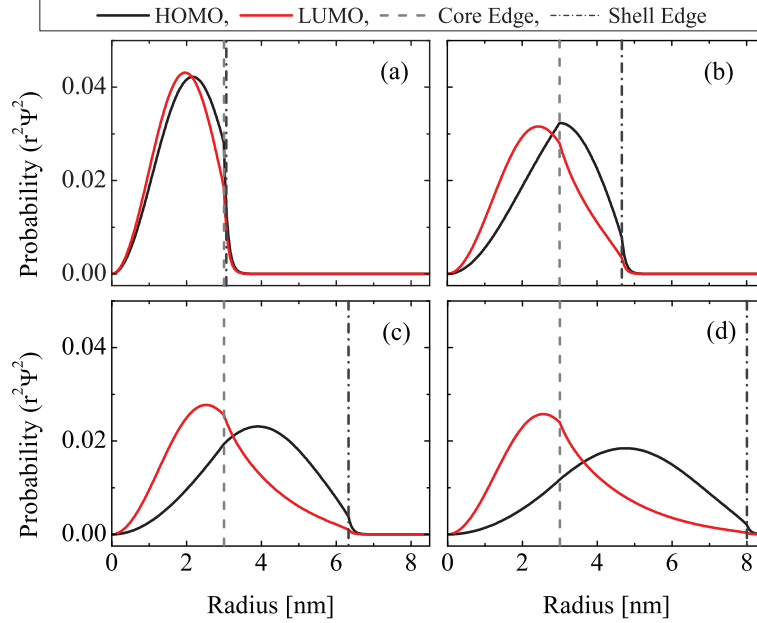


Figure 3.4: Wavefunctions for a constant 6 nm diameter core and variable shell thickness of (a) 0.0 nm, (b) 1.67 nm, (c) 3.33 nm, (d) 5.0 nm.

els are outside the gaps, oscillatory solutions are allowed; but when inside, only exponentially-decaying solutions are allowed. In small QDs, the energy levels are high above the band edges, so oscillatory solutions are allowed in both materials and confinement to the core is prevented. In large QDs, the energy levels decrease in magnitude. Owing to the positive offset of the PbS energy gap, the LUMO crosses the PbS conduction band before the HOMO crosses the valence band. Only decaying solutions are then allowed in the PbS shell, and the LUMO is confined to the core.

Because much of the behavior of large core-shell QDs depends on the band offsets, it is sensitive to the choice of bulk energy gap offset. Thus, the results for large structures should not be trusted quantitatively without an accurate, and preferably experimental, value of the offset. If large core-shell QDs can be fabricated in the future, analysis of their spectra may help determine the band offset. On the other hand, small QDs have energy levels far removed from the bulk band

edges, and are thus insensitive to the precise value of the offset. Thus, the qualitative predictions of the model in the small size regime are independent of the correct choice of energy gap offset. This is significant because all PbSe/PbS core-shell QDs fabricated to date fall into the small size regime.

3.5 Comparison with Experiment

3.5.1 Experimental Methods and Chemical Synthesis

PbSe/PbS QDs with various core sizes and shell thicknesses from 0-3 monolayers (ML) were grown according to Ref. [5]. Briefly, with a shell thickness up to 1.8 nm, PbSe/PbS core-shell QDs were prepared via a single injection of shell constituents of the appropriate stoichiometry amounts at 130 °C into a freshly prepared (free of Se monomers) PbSe core solution. However, core-shell CQDs with a shell thickness >1.8 nm required repeated injections (2-4 times) of the shell elements until the desired thickness was achieved. Representative aliquots were drawn from the reaction solution during the growth and their absorption and transmission electron microscopy (TEM) images were monitored. The absorption spectra were recorded on a spectrometer model UVVIS-NIR spectrometer JASCO V-570 at room temperature and the TEM images were recorded using a FEI Tecnai G2 T20 S-Twin instrument, operating at 200 kV.

The scanning tunneling microscopy (STM) and spectroscopy (STS) measurements of single-core or core-shell QDs were done by depositing QDs onto a gold [Au(111)] thin film, supported on a Mica substrate, and treated with a self-assembled hexanedithiol monolayer. This self-assembled monolayer was prepared

by immersing the gold films overnight in a solution, while any noncovalently linked thiol molecules were rinsed away from the surface. Then uniform and isolated QD coverage was formed by immersing thiol-treated gold films in a chloroform solution suspended with a low concentration of CQDs for a limited duration (1 min). Thus, isolated QDs were anchored to the gold substrate via thiol linking groups, immobilized during the experiment. The QD film on gold was further annealed at 110 °C overnight within the STM chamber in ultrahigh vacuum (UHV), removing any excess contamination. The topography and the electronic structure of a single PbSe/PbS core-shell CQD were measured by the use of a STM/STS Omircon Nanotechnology system (UHV variable temperature scanning probe microscopy), operating at 25 K in UHV (4×10^{-11} mbar) conditions. The STM images were achieved with a bias voltage (V_{bias}) of 2 V and a set-point current of 550 pA, adjusting a feedback loop to keep a constant current. The current-voltage (I-V) curves were measured by positioning an atomistic edge tip above a single dot and interrupting the feedback loop. The conductance spectra (dI/dV_{bias} versus V_{bias}) were obtained either by a numerical differentiation of the I-V curves or by a direct measure via a lock-in amplifier. A set-point current up to 70 pA was used when the voltage was altered between -2 V to +2 V. The reproducibility of the data was ensured by recording I-V curves of a single QD hundreds of times, and the data were smoothed by averaging over various accumulations.

3.5.2 Optical Spectroscopy

The energies of the lowest absorption peak are shown along with their predicted values in Fig. 3.5. Plotted versus outer diameter, all points fall on the same line (Fig. 3.5a), independent of shell thickness. Conversely, plotted versus core

diameter, larger shells have smaller transition energies (Fig. 3.5b). Both of these trends are predicted theoretically (Fig. 3.5c and d), and indicate that the outer diameter is the critical determinant of the QD energy levels, consistent with wave functions that are not confined within the core. In addition, with increasing shell thickness, both the lowest absorption peak and the emission peak are redshifted, with a decreasing rate of shift in thicker shells [13]. This trend is also evident from our calculated energies.

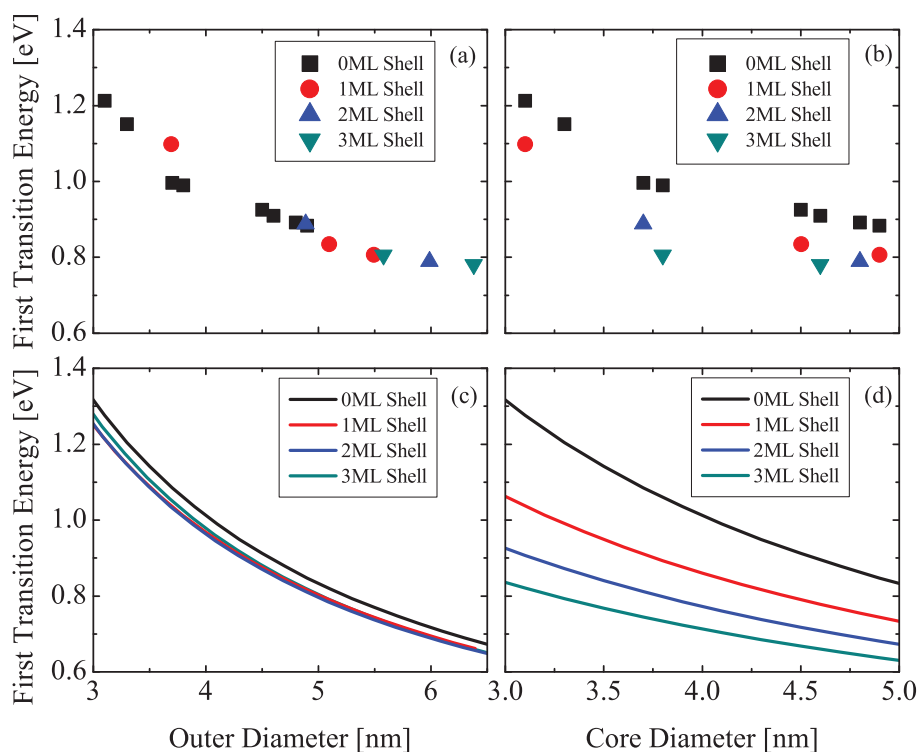


Figure 3.5: Experimental transition energies inferred from absorption (a) & (b), and predicted values (c) & (d). Shell thicknesses from 0 to 3 monolayers (ML) with various core sizes are shown.

3.5.3 Scanning Tunneling Spectroscopy

A complete description of how the STS data is analyzed is beyond the scope here, but for a thorough description of all of the issues relevant to STS on nanocrystals,

Ref. [14] is recommended. As explained in that reference, differences in voltage bias V_{bias} measured in an STS measurement are related to electronic energy gaps E_g by the following relation:

$$\eta\Delta V_{\text{bias}} = E_g + 2\Sigma \quad (3.7)$$

$$\Sigma \approx \frac{e^2}{2R} \left(\frac{1}{\epsilon_{\text{out}}} - \frac{1}{\epsilon_{\text{in}}} \right) \quad (3.8)$$

The scaling parameter η in Eq. (3.7) can be expressed in terms of a ratio of the capacitances of various parts of the system [14], and in our case was determined to vary between 0.65 to 0.75. All graphs presented here will have had this scaling factor already applied to the energies, thus calibrating them to the actual energy levels in the QD. Equation (3.8) is discussed in greater detail in a later chapter on charge transfer as it is a universal expression for the energy of charging of a dielectric sphere surrounded by a dielectric medium. Because the lead-salts are ionic solids, their dielectric constants are large enough ($\epsilon_{\text{static}} \approx 200$) to make the contribution from ϵ_{in} in Eq. (3.8) negligible. On the other hand, the outside dielectric constant would seem to be simply equal to 1.0, since the experiment is performed in UHV. But due to the effect of the nearby metal substrate, surface ligands, and the STM tip, an “effective” dielectric constant is often assumed, and used as a fitting parameter. For the purposes here, the value of 1.0 will be used, instead of the best fit value, because the data is still well-represented by this more physically reasonable choice.

Because scanning tunneling spectroscopy is not an ensemble measurement, but rather an experiment on a single QD, then ideally one should determine the size of the particular QD measured in the experiment. Because taking a height profile around the QD is necessary for an STS measurement, the natural method to extract the QD size would be to use the peak STM tip height. Unfortunately, using the tip

height introduces too much uncertainty in size estimates to be useful in modeling. For example, for the PbSe core QDs measured here, the measured STM tip height is 3.0 nm, but the expected size distribution of the sample from absorption and TEM is 4.4 ± 0.2 nm. Due to this large discrepancy, for the purposes of the modeling here, we use the average size of the QD ensemble, from either TEM or predicted from the absorption peak.

In Fig. 3.6a the measured tunneling spectra are plotted for four sizes of core-shell QDs. In each case the PbSe core is 4.4 nm in diameter, and the PbS shell is grown to a total outer diameter of 4.4, 4.9, 5.9, and 6.8 nm, respectively. In the spectra, the peaks correspond to the location of energy levels for electrons (right side) and holes (left side.) From these spectra, the transport energy gap (defined and discussed in more depth in a later chapter) can be directly determined by subtracting the location of the first hole peak from the first electron peak. This is shown in Fig. 3.6b, along with the energy gaps measured in absorption and predicted with the current model. After subtracting off the coulomb charging energy 2Σ as in Eq. (3.7), all three energy gaps show good agreement.

In addition, the location of excited electron and hole states also shows good agreement to that predicted with the current model. In Fig. 3.7, the tunneling spectra is shown along with the energy levels calculated with the current model. The energy levels shown include the Coulomb charging correction from Eq. (3.7), split equally between the electron and hole, so that electron levels are increased in energy by Σ and hole levels decreased by Σ . All electron peaks are well reproduced, though in each shown case one hole level is not. This might be either evidence that the effect of band anisotropy (not considered here) is more important for holes than electrons, which would slightly split some of the nearly-degenerate states shown,

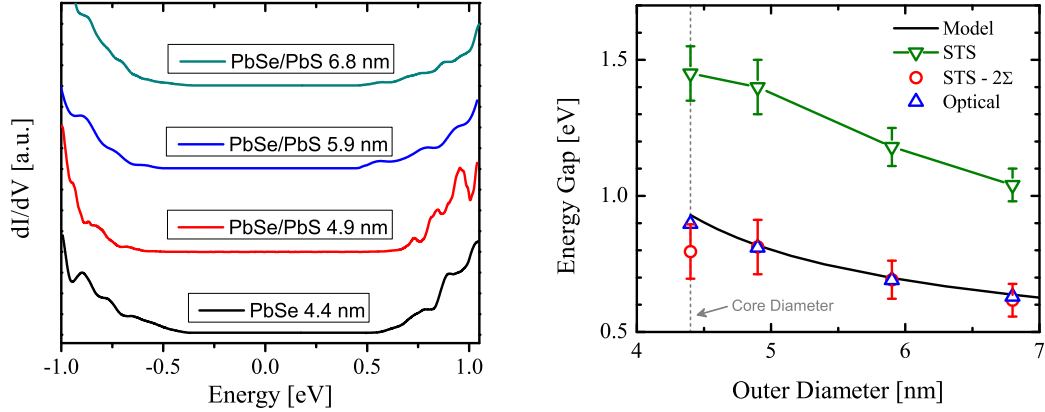


Figure 3.6: (a) Plots of dI/dV_{bias} vs. ηV_{bias} (called “Energy”) for one core and three core-shell QDs. All QDs have a PbSe core of 4.4 nm diameter. (b) Energy gaps of core-shell QDs from different sources. The black line is calculated from the present model. The green line+triangles is the gap determined by subtracting the location of the HOMO peak from the LUMO peak in the STS spectra in (a). The red circles are determined by subtracting the coulomb energy 2Σ in Eq. (3.8) from the STS energy gaps. Finally the blue triangles are from the first optical absorption peak.

or possibly that the Σ -point band edge is seen, which has been predicted to be more important for holes than electrons [15] in core PbSe QDs.

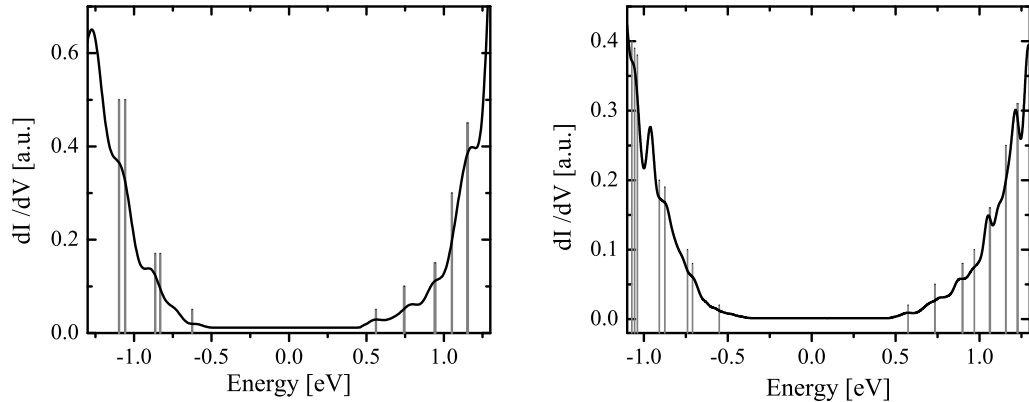


Figure 3.7: The tunneling spectra for (a) 5.9 nm and (b) 6.8 outer diameter core-shell QDs. Black lines are the measured spectra, and the vertical grey bars indicate predicted locations of the electron and hole energy levels, which are the bare energies plus the Coulomb charging correction, $E_i \pm \Sigma$, where the + is for electrons and the - for holes.

3.6 Conclusion

In conclusion, a four-band effective mass theory has been presented that is applicable to discontinuous material boundaries in lead-salt heterostructures. The model has been applied to PbSe/PbS core-shell QDs and reveals novel behavior of the wavefunctions in this structure. For small sizes, the envelope function extends over the nominal core and shell, while for large sizes the LUMO will be confined while the HOMO remains delocalized. Experimental results support these predictions.

Interestingly, one of the major motivations for core-shell structures, to separate the wavefunction from problems at the surface, is violated here. As a result, it is not surprising that the best quantum yields reported for core PbSe and core-shell PbSe-PbS of 40% and 45% are the same. Nevertheless, improved long-term stability is still seen in these structures, retaining their quality for months or years. We tentatively attribute this to increased resistance to oxygen of the PbS shell.

Future theoretical work could address the impact of band anisotropy or multi-valley coupling on the spectrum and wave functions of core-shell structures. Numerical calculations will be needed to refine this model or extend it to highly anisotropic PbTe. With only the LUMO confined in large QDs, the transition dipoles should depend strongly on QD size. This could have a variety of measurable effects, including size-dependent radiative lifetime and quantum yield. Finally, because the surfaces of core-shell structures are somehow passivated without confining the wavefunctions, the shell should not inhibit the transfer of electrons and holes, which will be relevant to applications such as solar energy conversion.

BIBLIOGRAPHY

- [1] M. Hines and P. Guyot-Sionnest, *J. Phys. Chem.* **100**, 468 (1996).
- [2] X. Peng, M. Schlamp, A. Kadavanich, and A. Alivisatos, *J. Am. Chem. Soc.* **119**, 7019 (1997).
- [3] M. C. Schlamp, X. Peng, and A. P. Alivisatos, *J. Appl. Phys.* **82**, 5837 (1997).
- [4] S. Kim, B. Fisher, H.-J. Eisler, and M. Bawendi, *J. Am. Chem. Soc.* **125**, 11466 (2003).
- [5] E. Lifshitz, M. Brumer, A. Kigel, A. Sashchiuk, M. Bashouti, M. Sirota, E. Galun, Z. Burshtein, A. LeQuang, I. Ledoux-Rak, and J. Zyss, *J. Phys. Chem. B* **110**, 25356 (2006).
- [6] E. P. Pokatilov, S. N. Klimin, V. M. Fomin, J. T. Devreese, and F. W. Wise, *Phys. Rev. B* **65**, 075316 (2002).
- [7] J. Li and L.-W. Wang, *Appl. Phys. Lett.* **84**, 3648 (2004).
- [8] S.-H. Wei and A. Zunger, *Phys. Rev. B* **55**, 13605 (1997).
- [9] I. Kang and F. W. Wise, *J. Opt. Soc. Am. B* **14**, 1632 (1997).
- [10] D. L. Mitchell and R. F. Wallis, *Phys. Rev.* **151**, 581 (1966).
- [11] G. E. Tudury, M. V. Marquezini, L. G. Ferreira, L. C. Barbosa, and C. L. Cesar, *Phys. Rev. B* **62**, 7357 (2000).
- [12] M. G. Burt, *J. Phys. Condens. Matter* **11**, 53 (1999).
- [13] M. Brumer, A. Kigel, L. Amirav, A. Sashchiuk, O. Solomesch, N. Tessler, and E. Lifshitz, *Adv. Funct. Mater.* **15**, 1111 (2005).
- [14] Y. M. Niquet, C. Delerue, G. Allan, and M. Lannoo, *Phys. Rev. B* **65**, 165334 (2002).
- [15] J. M. An, A. Franceschetti, S. V. Dudiy, and A. Zunger, *Nano Lett.* **6**, 2728 (2006).

4.1 Introduction

Solution-based chemical synthesis of semiconductor nanostructures has allowed tremendous flexibility in crystal morphology. After much work on zero-dimensional (0D) nanocrystals (NCs), attention is shifting to one-dimensional (1D) nanorods (NRs) and nanowires (NWs) [1, 2, 3, 4] and the variation of material properties in the transition from 0D to 1D. The electronic structure of these crystals is the foundation for understanding their properties. Previously, the electronic structure of 1D nanocrystals has been modeled using a variety of methods, including effective-mass theories based on $\mathbf{k} \cdot \mathbf{p}$ Hamiltonians [5, 6, 7, 8, 9], pseudopotential techniques [10, 11, 12], tight binding models [13, 14, 15, 16, 17], and density functional theory [18, 19, 20, 9, 17, 21]. A common theme in these calculations is that the relaxation of confinement in going from 0D to 1D goes hand-in-hand with an increase in the importance of Coulomb effects mediated through the nanocrystal's dielectric environment [22].

Lead–salt (PbS, PbSe, PbTe) nanocrystals offer unique advantages to study the interplay of these two effects. Their large exciton Bohr radii places them at the limit of strong confinement, while their large dielectric constants coupled with their mirror–like electron and hole spectra substantially reduce the Coulomb interaction in spherical quantum dots [23, 24]. However, in a 1D structure the Coulomb interaction can act primarily through the host medium, so it will not be screened as effectively as in 0D [7]. Thus, the lead salts provide a unique system to study the transition from strong confinement to strong Coulomb binding as the

length of the nanocrystal changes.

Within $\mathbf{k}\cdot\mathbf{p}$ theory, the general treatment of the optical properties of NWs and NRs surrounded by media with small dielectric constant was developed in Refs. [5, 6, 7]. A type of adiabatic approximation naturally separates the calculation into pieces. In recognition of strong confinement perpendicular to the NR or NW axis, one first calculates the 1D subband energies and wavefunctions, while neglecting the Coulomb interaction. Next, using these wave functions of transverse electron and hole motion, one can calculate the longitudinal motion of the exciton, including corrections from image forces in the surrounding medium. To do that, the three-dimensional Coulomb potential is averaged to a one-dimensional Coulomb interaction between the electron and hole along the NW or NR axis. Using this potential, the spectra of 1D excitons and their transition oscillator strengths are found. Finally, in NRs one should find the spectrum of the exciton center of mass motion, in order to include this additional effect of confinement. The main aspects of this framework were performed for lead–salt nanowires recently by Rupasov [25], although approximations to the simplified band structure used in that paper preclude the description of real experimental results.

In this chapter we present calculations of the 1D subband energy spectra of lead–salt nanowires with arbitrary axis orientation, taking into account the multi-valley structure and accurate electron and hole energy-level dispersions in these semiconductors. For PbSe NWs with axis along the $\langle 100 \rangle$ direction, we calculate the spectra of 1D excitons including self-interaction corrections. Surprisingly, the calculations show that although the binding energy of excitons in the smallest NWs reaches 350 meV, the optical transition energies are not affected by the small dielectric constant of the surrounding medium and are almost identical to the

transitions between non-interacting electron and hole subbands. The cancelation of the exciton binding energy and the self-interaction corrections to the electron and hole levels is a consequence of the almost mirror symmetry of the conduction and valence bands of PbSe. The theoretical results agree well with the measured absorption spectra of $\langle 100 \rangle$ PbSe NRs.

The chapter is organized as follows. In Section 4.2 we will describe the Hamiltonian governing the 1D nanowire system, with solutions in Section 4.3. In Section 4.4 we present the effects of dielectric confinement and Coulomb forces on the 1D exciton, with 1D wavefunction solutions in Section 4.5. Experimental data and comparison with theory are presented in Section 4.6, followed by discussion and conclusion.

4.2 Four band effective mass model

PbS, PbSe, and PbTe are direct-gap semiconductors, with extrema of the conduction and valence bands at the L points in the Brillouin zone. The energy bands near the L point can be well-described within the four-band $\mathbf{k} \cdot \mathbf{p}$ model [26, 27]. This model takes into account the direct interaction between the nearest conduction and valence bands, as well as the contributions of the remote bands to the electron and hole effective masses. Following Ref. [24], we use the multiband effective mass approximation and expand the full wave functions inside the nanorod as

$$\Phi(\mathbf{r}) = \sum_{\mu=\pm 1/2} \Psi_{\mu}^c(\mathbf{r})|L_{6,\mu}^{-}\rangle + \sum_{\mu=\pm 1/2} \Psi_{\mu}^v(\mathbf{r})|L_{6,\mu}^{+}\rangle, \quad (4.1)$$

where $|L_{6,\mu}^{-}\rangle$ and $|L_{6,\mu}^{+}\rangle$ are the Bloch functions of the conduction band and valence band edge, respectively, at the L -point. The upper sign “ \pm ” in the notation

reflects the invariance of these functions with respect to the operation of spatial inversion. The smooth functions $\Psi_{\pm 1/2}^c(\mathbf{r})$ and $\Psi_{\pm 1/2}^v(\mathbf{r})$ are the components of the conduction band and valence band spinor envelopes, respectively:

$$\Psi^c = \begin{pmatrix} \Psi_{1/2}^c \\ \Psi_{-1/2}^c \end{pmatrix}, \quad \Psi^v = \begin{pmatrix} \Psi_{1/2}^v \\ \Psi_{-1/2}^v \end{pmatrix}. \quad (4.2)$$

The bi-spinor envelope function $\Psi = \begin{pmatrix} \Psi^c \\ \Psi^v \end{pmatrix}$ is the solution of the Schrödinger equation $\hat{H}(\hat{\mathbf{p}})\Psi = E\Psi$, where $\hat{\mathbf{p}} = \hbar\hat{\mathbf{k}} = -i\hbar\nabla$ is the momentum operator, and the Hamiltonian $\hat{H}(\hat{\mathbf{p}})$ of Ref. [24] can be written in compact form as

$$\hat{H}(\hat{\mathbf{p}}) = \begin{pmatrix} \left(\frac{E_g}{2} + \frac{\hat{p}_z^2}{2m_l^-} + \frac{\hat{p}_\perp^2}{2m_t^-} \right) \hat{U}_2 & \frac{P_l}{m_0} \hat{p}_z \hat{\sigma}_z + \frac{P_t}{m_0} (\hat{p}_\perp \hat{\sigma}_\perp) \\ \frac{P_l}{m_0} \hat{p}_z \hat{\sigma}_z + \frac{P_t}{m_0} (\hat{p}_\perp \hat{\sigma}_\perp) & - \left(\frac{E_g}{2} + \frac{\hat{p}_z^2}{2m_l^+} + \frac{\hat{p}_\perp^2}{2m_t^+} \right) \hat{U}_2 \end{pmatrix}. \quad (4.3)$$

In Eq. (4.3) \hat{U}_2 is the 2×2 unit matrix, $\hat{\boldsymbol{\sigma}} = \{\hat{\sigma}_x, \hat{\sigma}_y, \hat{\sigma}_z\}$ are the Pauli matrices that act on the spinor components of the wave functions ($\mu = \pm 1/2$), E_g is the bulk energy gap, E is the electron or hole energy measured from the middle of the gap, m_0 is the free electron mass, $\hat{p}_\perp^2 = \hat{p}_x^2 + \hat{p}_y^2$, $(\hat{p}_\perp \hat{\sigma}_\perp) = \hat{p}_x \hat{\sigma}_x + \hat{p}_y \hat{\sigma}_y$, P_t and P_l are the transverse and longitudinal momentum matrix elements taken between the conduction and valence band edge Bloch functions [24], and m_t^\pm and m_l^\pm are the remote-band contribution to the transverse and longitudinal band edge effective masses, respectively. For electrons and holes, these band edge effective masses can be expressed as $m_{l,t}^e = [1/m_{l,t}^- + 2P_{l,t}^2/m_0^2 E_g]^{-1}$ and $m_{l,t}^h = [1/m_{l,t}^+ + 2P_{l,t}^2/m_0^2 E_g]^{-1}$, respectively. In each valley, the z axis in Eq. (4.3) is directed toward the L-point of the Brillouin zone, e.g. along the $\langle 111 \rangle$ direction of the cubic lattice. As a result, for each of the four valleys, the z axis will point in different directions.

Although the Hamiltonian of Eq. (4.3) has cylindrical symmetry with respect to, e.g., the $\langle 111 \rangle$ crystallographic direction, this direction may not coincide with

the NR growth direction. For a description of NR electronic and optical properties it is convenient to use coordinates connected with the latter direction instead, even though the cylindrical symmetry of the Hamiltonian is generally broken. In PbS and PbSe, the small anisotropy of conduction and valence bands allows us to treat deviations from cylindrical symmetry perturbatively. The Hamiltonian (4.3) can be written $\hat{H} = \hat{H}_0 + \hat{H}_{an}$, where the cylindrically-symmetric part \hat{H}_0 is

$$\hat{H}_0(\hat{\mathbf{p}}) = \begin{pmatrix} \left(\frac{E_g}{2} + \frac{\hat{p}_z^2}{2m_z^-} + \frac{\hat{p}_\perp^2}{2m_\perp^-} \right) \hat{U} & \frac{P_z}{m_0} \hat{p}_z \hat{\sigma}_z + \frac{P_\perp}{m_0} (\hat{p}_\perp \hat{\sigma}_\perp) \\ \frac{P_z}{m_0} \hat{p}_z \hat{\sigma}_z + \frac{P_\perp}{m_0} (\hat{p}_\perp \hat{\sigma}_\perp) & - \left(\frac{E_g}{2} + \frac{\hat{p}_z^2}{2m_z^+} + \frac{\hat{p}_\perp^2}{2m_\perp^+} \right) \hat{U} \end{pmatrix}. \quad (4.4)$$

The modified band parameters are

$$\begin{aligned} P_\perp &= \frac{P_t}{2}(1 + \cos^2 \theta) + \frac{P_l}{2} \sin^2 \theta & P_z &= P_t \sin^2 \theta + P_l \cos^2 \theta & (4.5) \\ \frac{1}{m_\perp^\pm} &= \frac{1}{2m_t^\pm}(1 + \cos^2 \theta) + \frac{1}{2m_l^\pm} \sin^2 \theta & \frac{1}{m_z^\pm} &= \frac{1}{m_t^\pm} \sin^2 \theta + \frac{1}{m_l^\pm} \cos^2 \theta & (4.6) \end{aligned}$$

where θ is the angle between the growth axis and the $\langle 111 \rangle$ direction. The anisotropic part of the Hamiltonian is given in Appendix B.1. Note that Eq. (4.4) has a form identical to Eq. (4.3), but the z axis is now directed along the growth axis. For arbitrary orientation of the growth direction, there will be four different angles θ for each of the four valleys, and therefore four different sets of modified band parameters defined in Eq. (4.5). As a result, each valley will have unique electronic structure.

The energy spectra associated with the different valleys become degenerate when the growth direction leads to identical values of θ for them. The highest degree of degeneracy is reached when the growth direction is along the $\langle 100 \rangle$ crystal axis. In this case all four valleys have the same θ ; $\cos^2 \theta = 1/3$, which results in $P_\perp = P_z$ and $m_\perp = m_z$ in Eq. (4.4). All of the spectra are degenerate.

The anisotropic part \hat{H}_{an} of the full Hamiltonian can be considered as a perturbation if $|P_l - P_t| \ll P_l + P_t$ and $|1/m_l^\pm - 1/m_t^\pm| \ll 1/m_l^\pm + 1/m_t^\pm$. The

first-order corrections to the solutions of \hat{H}_0 caused by \hat{H}_{an} vanish in the 2-fold Kramers-degenerate subspace at each energy level. As a result, only second-order perturbation theory gives corrections to the energy levels. We will neglect these corrections from this point on, although an example higher-order calculation appears in Appendix B.1.

4.3 Energy spectra in PbSe Nanowires

The first step in our modeling process is to find the energy spectra of 1D subbands of infinitely-long cylindrical nanowires, temporarily ignoring the Coulomb interaction. The cylindrical symmetry of the Hamiltonian of Eq. (4.4) allows the solutions to take the form

$$\Psi^n(k_z) = \begin{pmatrix} \mathcal{R}_1^n(\rho) \exp(i(n - 1/2)\phi) \\ i\mathcal{R}_2^n(\rho) \exp(i(n + 1/2)\phi) \\ \mathcal{R}_3^n(\rho) \exp(i(n - 1/2)\phi) \\ i\mathcal{R}_4^n(\rho) \exp(i(n + 1/2)\phi) \end{pmatrix} \exp(ik_z z), \quad (4.7)$$

where ϕ is the azimuthal angle, $n = \pm 1/2, \pm 3/2, \pm 5/2, \dots$ is the total angular momentum projection on the nanowire axes defined by the operator $\hat{J}_z = -i\partial/\partial\phi + \hat{S}_z$, $\hbar k_z$ is the momentum along the nanowire z axis, and $\rho = \sqrt{x^2 + y^2}$ is the radial coordinate in the plane perpendicular to the NW axis. The chosen phase of each component of the function $\Psi^n(k_z)$ allows the radial functions $\mathcal{R}_i^n(\rho)$ to be pure real. Substitution of Eq. (4.7) into Eq. (4.4) yields the system of differential equations

that defines these functions:

$$\begin{aligned}
& \left(\alpha_- + \frac{\hbar^2}{2m_{\perp}^-} \Delta_{n-1/2} \right) \mathcal{R}_1^n(\rho) + \frac{\hbar k_z P_z}{m_0} \mathcal{R}_3^n(\rho) + \frac{\hbar P_{\perp}}{m_0} \hat{D}_{n+1/2}^- \mathcal{R}_4^n(\rho) = 0, \\
& \left(\alpha_- + \frac{\hbar^2}{2m_{\perp}^-} \Delta_{n+1/2} \right) \mathcal{R}_2^n(\rho) + \frac{\hbar P_{\perp}}{m_0} \hat{D}_{n-1/2}^+ \mathcal{R}_3^n(\rho) - \frac{\hbar k_z P_z}{m_0} \mathcal{R}_4^n(\rho) = 0, \\
& -\frac{\hbar k_z P_z}{m_0} \mathcal{R}_1^n(\rho) - \frac{\hbar P_{\perp}}{m_0} \hat{D}_{n+1/2}^- \mathcal{R}_2^n(\rho) + \left(\alpha_+ + \frac{\hbar^2}{2m_{\perp}^+} \Delta_{n-1/2} \right) \mathcal{R}_3^n(\rho) = 0, \\
& -\frac{\hbar P_{\perp}}{m_0} \hat{D}_{n-1/2}^+ \mathcal{R}_1^n(\rho) + \frac{\hbar k_z P_z}{m_0} \mathcal{R}_2^n(\rho) + \left(\alpha_+ + \frac{\hbar^2}{2m_{\perp}^+} \Delta_{n+1/2} \right) \mathcal{R}_4^n(\rho) = 0, \quad (4.8)
\end{aligned}$$

where $\alpha_{\pm} = E_g/2 \pm E + \hbar^2 k_z^2 / (2m_z^{\pm})$. The differential operators

$$\hat{D}_m^{\pm} = \mp \frac{\partial}{\partial \rho} + \frac{m}{\rho} \quad (4.9)$$

are the raising and lowering operators $\hat{D}_m^{\pm} J_m(k\rho) = k J_{m\pm 1}(k\rho)$ for the Bessel functions $J_m(k\rho)$ with integer index, and the operator $\Delta_m = \hat{D}_{m+1}^- \hat{D}_m^+ = -(1/\rho)(\partial/\partial\rho)\rho(\partial/\partial\rho) + m^2/\rho^2$.

It is easy to check using the raising and lowering properties of the \hat{D}_m^{\pm} operators that the radial eigenfunctions of Eqs. (4.8) should take the form

$$\begin{pmatrix} \mathcal{R}_1^n(\rho) \\ \mathcal{R}_2^n(\rho) \\ \mathcal{R}_3^n(\rho) \\ \mathcal{R}_4^n(\rho) \end{pmatrix} = \begin{pmatrix} C_1 J_{n-1/2}(k\rho) \\ C_2 J_{n+1/2}(k\rho) \\ C_3 J_{n-1/2}(k\rho) \\ C_4 J_{n+1/2}(k\rho) \end{pmatrix}. \quad (4.10)$$

Substitution of this into Eqs. (4.8) yields a 4x4 system of linear equations for the coefficients $C_{1,2,3,4}$. Setting the determinant of this system to zero produces the relation between the quasi-momentum k_{ρ} and the energy of electrons or holes E :

$$\hbar^2 k_{\rho}^2 = -\alpha(E) \pm \sqrt{\alpha(E)^2 + \beta(E)}, \quad (4.11)$$

where

$$\begin{aligned}
\alpha(E) &= m_{\perp}^+ \left(E + \frac{\hbar^2 k_z^2}{2m_z^+} + \frac{E_g}{2} \right) - m_{\perp}^- \left(E - \frac{\hbar^2 k_z^2}{2m_z^-} - \frac{E_g}{2} \right) + m_{\perp}^- m_{\perp}^+ \frac{2P_{\perp}^2}{m^2} \\
\beta(E) &= 4m_{\perp}^+ m_{\perp}^- \left(E + \frac{\hbar^2 k_z^2}{2m_z^+} + \frac{E_g}{2} \right) \left(E - \frac{\hbar^2 k_z^2}{2m_z^-} - \frac{E_g}{2} \right) - 4 \frac{m_{\perp}^- m_{\perp}^+}{m^2} P_z^2 \hbar^2 k_z^2. \quad (4.12)
\end{aligned}$$

From Eq. (4.11) it is clear that k_ρ^2 can be positive or negative. The negative value of k_ρ^2 results in an imaginary $k_\rho = i\lambda_\rho$, with λ_ρ defined by Eq. (4.11) as $\hbar^2\lambda_\rho^2 = \alpha(E) + \sqrt{\alpha(E)^2 + \beta(E)}$. The complex arguments in Eq. (4.10) are then simplified by replacing the Bessel functions $J_m(i\lambda_\rho\rho)$ with the modified Bessel functions $I_m(\lambda_\rho\rho)$ using the relationship $J_m(i\lambda_\rho\rho) = i^m I_m(\lambda_\rho\rho)$. For each value of k_ρ^2 , there are two independent solutions of the 4x4 linear system for the coefficients $C_{1,2,3,4}$. These two solutions can be chosen such that either $C_3 = 0$ or $C_4 = 0$, which allows the remaining coefficients C_i to be found. Taking into account the positive and negative value of k_ρ^2 , there are four independent solutions for each energy E .

The energy spectrum is determined by the boundary conditions at the NW surface. The boundary conditions are defined on all four components of the wave function, which inside of the NW can be always written as a linear combination of the four degenerate solutions discussed above

$$\begin{pmatrix} \mathcal{R}_1^n(\rho, k_z) \\ \mathcal{R}_2^n(\rho, k_z) \\ \mathcal{R}_3^n(\rho, k_z) \\ \mathcal{R}_4^n(\rho, k_z) \end{pmatrix} = a \begin{pmatrix} k_\rho P_\perp J_{n-1/2}(k_\rho\rho) \\ -k_z P_z J_{n+1/2}(k_\rho\rho) \\ 0 \\ \Gamma_k J_{n+1/2}(k_\rho\rho) \end{pmatrix} + b \begin{pmatrix} k_z P_z J_{n-1/2}(k_\rho\rho) \\ k_\rho P_\perp J_{n+1/2}(k_\rho\rho) \\ \Gamma_k J_{n-1/2}(k_\rho\rho) \\ 0 \end{pmatrix} + \\ + c \begin{pmatrix} \lambda_\rho P_\perp I_{n-1/2}(\lambda_\rho\rho) \\ -k_z P_z I_{n+1/2}(\lambda_\rho\rho) \\ 0 \\ \Gamma_\lambda I_{n+1/2}(\lambda_\rho\rho) \end{pmatrix} + d \begin{pmatrix} k_z P_z I_{n-1/2}(\lambda_\rho\rho) \\ -\lambda_\rho P_\perp I_{n+1/2}(\lambda_\rho\rho) \\ \Gamma_\lambda I_{n-1/2}(\lambda_\rho\rho) \\ 0 \end{pmatrix}, \quad (4.13)$$

where

$$\begin{aligned} \Gamma_k &= \frac{m_0}{\hbar} \left(E - \frac{E_g}{2} \right) - \frac{\hbar m_0}{2m_\perp^- m_z^-} (k_z^2 m_\perp^- + k_\rho^2 m_z^-), \\ \Gamma_\lambda &= \frac{m_0}{\hbar} \left(E - \frac{E_g}{2} \right) - \frac{\hbar m_0}{2m_\perp^- m_z^-} (k_z^2 m_\perp^- - \lambda_\rho^2 m_z^-), \end{aligned} \quad (4.14)$$

and a, b, c , and d are determined by the boundary conditions.

For NWs with an impenetrable surface, the *standard* boundary conditions require each component of the wave function defined in Eq. (4.13) to vanish, leading to $\mathcal{R}_i^n(R, k_z) = 0$, where $i = 1, 2, 3, 4$ and R is the NW radius. These four equations define the 4x4 system for the a, b, c, d coefficients. Requiring the determinant of this system to be zero yields the following implicit equation for the 1D energy bands for angular momentum n , and as a function of the parameter k_z :

$$k_\rho \lambda_\rho [(I_+^n)^2 (J_-^n)^2 - (I_-^n)^2 (J_+^n)^2] + \frac{k_z^2 P_z^2 (\Gamma_k - \Gamma_\lambda)^2 + P_t^2 (k_\rho^2 \Gamma_\lambda^2 - \lambda_\rho^2 \Gamma_k^2)}{P_t^2 \Gamma_k \Gamma_\lambda} I_-^n I_+^n J_-^n J_+^n = 0, \quad (4.15)$$

where we use the notation $J_\pm^n = J_{n\pm 1/2}(k_\rho R)$ and $I_\pm^n = I_{n\pm 1/2}(\lambda_\rho R)$.

After determining the energy from Eq. (4.15), the wavefunctions can be constructed from Eq. (4.13), with only the normalization undetermined. We will use the following notation for normalized eigenfunctions: $\Psi_e^{n,k}$ and $\Psi_h^{n,k}$ for the electron and hole levels given by Eq. (4.15), correspondingly, where $k = 1, 2, 3, \dots$ is the index of the 1D subband with angular momentum n , and $\int_0^R |\Psi_e^{n,k}|^2 \rho_e d\rho_e 2\pi = \int_0^R |\Psi_h^{n,k}|^2 \rho_h d\rho_h 2\pi = 1$.

Using Eq. (4.15) we calculated the energy levels for a 4-nm PbSe NW with various growth directions. The energy band parameters of PbSe which we used in this calculation will be described in a later section. The effective energy gap of the NW, which is the energy distance between the top of the highest 1D sub-band of the valence band and the bottom of the lowest 1D sub-band of the conduction band, impacts many material properties. Figure 4.1 shows the effective energy gap for all four valleys as a function of the growth direction of the nanowire. Because the plot is calculated along high-symmetry directions in the Brillouin zone, the degeneracy of the four valleys is never completely lifted. Without any intervalley

coupling, each of these energy gaps would have separate optical absorption and emission peaks associated with it.

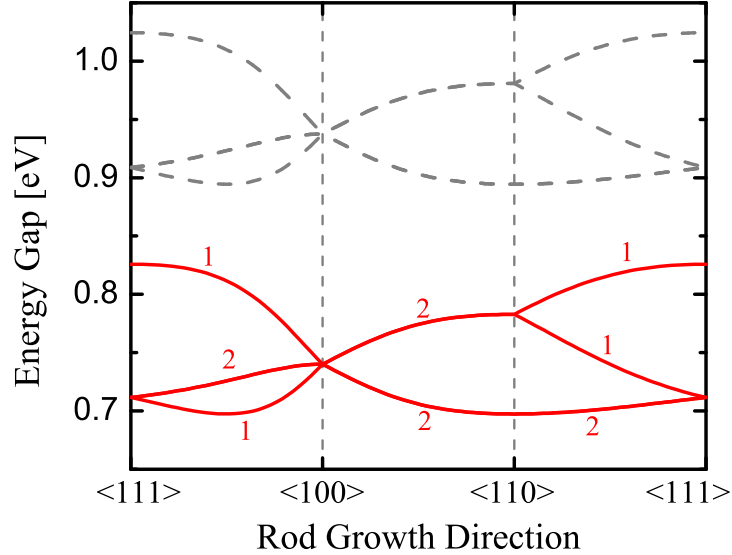


Figure 4.1: Energy gaps of a 4-nm diameter PbSe NW at each of the four valleys as a function of the growth direction of the NW (red lines). The numbers indicate the valley degeneracy of the energy gaps. Dashed grey lines are the same energy gaps after accounting for the self-Coulomb interaction, described later in the text.

Figures 4.2a and 4.2b show the dispersion of the several lowest 1D subbands of the conduction and valence bands in NWs grown along the $\langle 111 \rangle$ and $\langle 100 \rangle$ directions, respectively. NWs grown along $\langle 111 \rangle$ have one valley oriented parallel to the growth direction and the other three valleys oriented at the equal angles $\theta = 71^\circ$ from it. For the $\langle 100 \rangle$ NW, all four valleys are at the same angle $\theta = 55^\circ$ from the growth direction. It is clear that both the band-edge energies and the effective masses of the 1D subbands depend strongly on the growth direction.

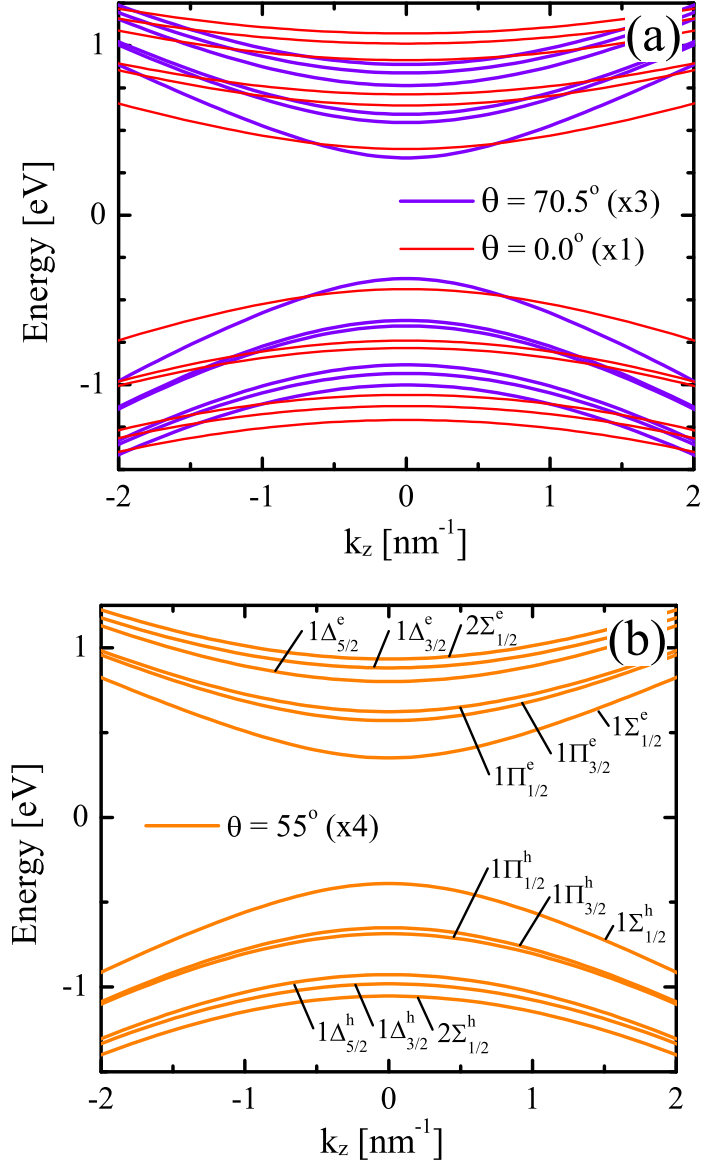


Figure 4.2: 1D band structure of a 4-nm PbSe NW for the cases of the axis along the directions (a) $\langle 111 \rangle$ and (b) $\langle 100 \rangle$. The bands are labeled by the angle θ between the considered valley and the rod growth axis and also by their multiple valley degeneracy, up to a maximum of (x4). In (b), the individual subbands are labeled using notation adopted from molecular physics: $kX_{|n|}^{e,h}$ for the k^{th} electron or hole level of certain symmetry with total z angular momentum n , where $X = \Sigma, \Pi, \Delta, \dots$, is used for $|m| = 0, 1, 2, \dots$, respectively, where m is the angular momentum projection of the conduction (valence) band component of the wavefunction of the electron, ‘e’, (hole, ‘h’) state. In (a), the order of the levels is the same, and the labeling is suppressed for clarity.

4.4 Dielectric confinement

The optical properties of all semiconductor nanostructures are controlled by the strength of the Coulomb interaction between the electron–hole pair participating in the emission and absorption of photons [28]. Compared to the screened Coulomb interaction in a bulk crystal, the interaction is usually enhanced because the electric field of the electron and hole localized inside the nanostructure penetrates into the surrounding medium, which commonly has a dielectric constant smaller than that of the semiconductor. In addition, any charge in the vicinity of this interface polarizes it. In the case of a flat interface, for example, this polarization can be described easily using an image charge that interacts with the primary charge [29]. In the case of small external dielectric constant the interaction is repulsive. This repulsive potential in nanostructures of any shape leads to an additional confinement of carriers, which is referred to as dielectric confinement.

To model these effects in NRs and NWs, the analytic potential for two charges in an infinite dielectric cylinder $U(\mathbf{r}_e, \mathbf{r}_h)$ [30] is used. It was shown previously [7] that this approximation works well as long as the rod length is larger than the size of the exciton. The potential naturally divides into four terms [31]: the unscreened direct interaction of the two charges U_d , the modification of this interaction due to the image effects of the solvent U_s , and the two self-interactions of each charge with its own image U_e and U_h :

$$\begin{aligned}
 U(\mathbf{r}_e, \mathbf{r}_h) &= -e^2/(\kappa_s|\mathbf{r}_e - \mathbf{r}_h|) - eV_s(\mathbf{r}_e, \mathbf{r}_h) + \frac{1}{2}eV_s(\mathbf{r}_e, \mathbf{r}_e) + \frac{1}{2}eV_s(\mathbf{r}_h, \mathbf{r}_h) \\
 &\equiv U_d(|\mathbf{r}_e - \mathbf{r}_h|) + U_s(\mathbf{r}_e, \mathbf{r}_h) + U_e(\mathbf{r}_e) + U_h(\mathbf{r}_h)
 \end{aligned}
 \tag{4.16}$$

where the function V_s has the form

$$V_s(\mathbf{r}_e, \mathbf{r}_h) = \frac{e}{2\pi^2\kappa_s} \int_0^\infty du \sum_{m=0}^\infty \cos(u(z_e - z_h)) \cos(m(\phi_e - \phi_h))(2 - \delta_{m0}) \times \quad (4.17)$$

$$\times \frac{(\kappa_s - \kappa_m)I_m(u\rho_e)I_m(u\rho_h)K_m(Ru)(K_{m-1}(Ru) + K_{m+1}(Ru))}{\kappa_s K_m(Ru)(I_{m-1}(Ru) + I_{m+1}(Ru)) + \kappa_m I_m(Ru)(K_{m-1}(Ru) + K_{m+1}(Ru))}$$

and where κ_s and κ_m are the optical dielectric constants of the bulk semiconductor and the surrounding medium, respectively. I_m and K_m are the modified Bessel functions of the first and second kind. For PbSe we will use $\kappa_s = 23$, and for the medium, if not explicitly stated otherwise, $\kappa_m = 2$ throughout this work.

The self-interaction terms $U_e(\mathbf{r}_e)$ and $U_h(\mathbf{r}_h)$ always contribute to the energy of each electron and hole subband calculated in Section 4.3. In narrow NWs and NRs, where the self-interaction energy is smaller than the confined energies, this contribution can be calculated perturbatively for electron and hole levels, respectively:

$$E_{\text{self},e}^{n,k} = \int \rho_e d\rho_e d\phi_e |\Psi_e^{n,k}|^2 U_e(\mathbf{r}_e), \quad E_{\text{self},h}^{n',k'} = \int \rho_h d\rho_h d\phi_h |\Psi_h^{n',k'}|^2 U_h(\mathbf{r}_h). \quad (4.18)$$

The self-interaction terms $E_{\text{self},e}^{n,k}$ and $E_{\text{self},h}^{n',k'}$ increase the energy of all electron and hole 1D subbands and consequently the effective energy gap in nanowires. The perturbed electron and hole subbands with $n = n' = 1/2$ and $k = k' = 1$ are shown in Fig. 4.1.

In addition, in narrow NWs and NRs one can use an adiabatic approximation of the Coulomb interaction [32, 33], which replaces the three-dimensional potential of electrons and holes of Eq. (4.16) by a one-dimensional Coulomb potential that describes their interaction along the NW/NR axis. The adiabatic potential is obtained by averaging the potential over wave functions $\Psi_e^{n,k}$ and $\Psi_h^{n',k'}$ of the corresponding electron and hole subband. Averaging the first two terms of Eq.

(4.16) results in the 1D adiabatic potential

$$V_{n,k}^{n',k'}(|z_e - z_h|) = \int \rho_e d\rho_e d\phi_e \int \rho_h d\rho_h d\phi_h |\Psi_e^{n,k}|^2 |\Psi_h^{n',k'}|^2 (U_d(|\mathbf{r}_e - \mathbf{r}_h|) + U_s(\mathbf{r}_e, \mathbf{r}_h)), \quad (4.19)$$

which describes the interaction of electrons and holes occupying different subbands. This adiabatic potential is a function of the electron and hole separation, $|z_e - z_h|$, only. One can show that at large distances $|z_e - z_h| \gg R$ it takes the form of a one-dimensional Coulomb potential with the dielectric constant of the surrounding medium, $V_{n,k}^{n',k'} \sim -e^2/(\kappa_m |z_e - z_h|)$. The adiabatic potential for the ground electron and hole subbands with $n = n' = 1/2$ and $k = k' = 1$ is shown in Fig.4.3.

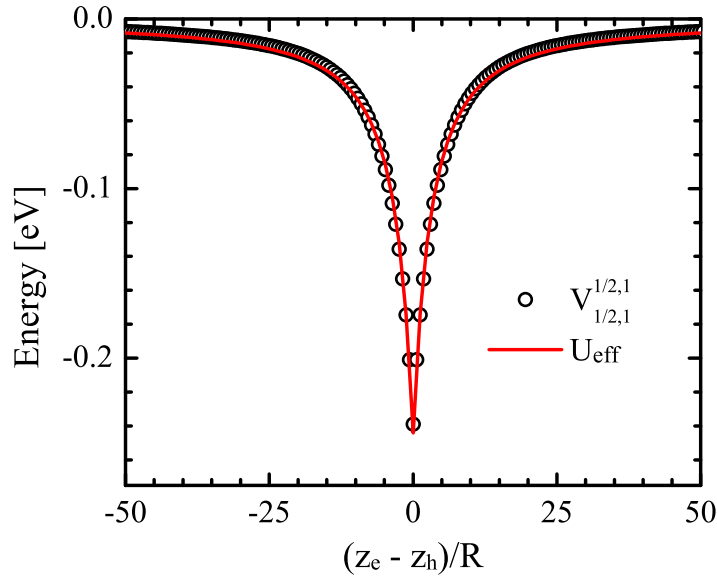


Figure 4.3: Points show the effective binding potential, $V_{1/2,1}^{1/2,1}$, between an electron and a hole occupying the ground one dimensional subband $n = n' = 1/2$ and $k = k' = 1$ as a function of their separation, calculated for a 4-nm radius PbSe NW. The solid line shows the approximation of this dependence by the Elliott & Loudon effective potential described by Eq. (4.21)

4.5 1D excitons in PbSe nanowires and nanorods

The attractive 1D potential described by Eq. (4.19) creates a series of one-dimensional exciton states for each pair of electron and hole subbands (n, k) and (n', k') . The effective masses of electrons and holes along the NW axis $m_e^{n,k}$ and $m_e^{n',k'}$ at the bottom and the top of each subband, correspondingly, is determined by Eq. (4.15). This allows us to write a one-dimensional Schrödinger equation for these 1D excitons:

$$-\frac{\hbar^2}{2\mu_{n,k}^{n',k'}} \frac{\partial^2}{\partial z^2} \Psi_{1D} - \frac{\hbar^2}{2M_{n,k}^{n',k'}} \frac{\partial^2}{\partial Z^2} \Psi_{1D} + U_{n,k}^{n',k'}(z) \Psi_{1D} = \varepsilon_{n,k}^{n',k'} \Psi_{1D}, \quad (4.20)$$

where we introduce the electron-hole separation, $z = z_e - z_h$ and the exciton center-of-mass coordinate $Z = (m_e^{n,k} z_e + m_h^{n',k'} z_h) / (m_e^{n,k} + m_h^{n',k'})$. $\mu_{n,k}^{n',k'} = m_e^{n,k} m_h^{n',k'} / (m_e^{n,k} + m_h^{n',k'})$ is the reduced mass and $M_{n,k}^{n',k'} = m_e^{n,k} + m_h^{n',k'}$ is the total effective mass of the 1D exciton. Importantly, the exciton binding energy $\varepsilon_{n,k}^{n',k'}$ in this equation is calculated relative to the distance between the bottom of the (n, k) conduction subband and the top of the (n', k') valence subband, assuming the self-interaction energy terms $E_{\text{self},e}^{n,k}$ and $E_{\text{self},h}^{n',k'}$ are already taken into account. The solution of Eq. (4.20) can be separated into $\Psi_{1D}(z, Z) = \psi_{1D}(z) \Psi_{\text{cm}}(Z)$. The wave function $\psi_{1D}(z)$ describes relative electron-hole motion and gives the spectrum of 1D excitons. The second component, $\Psi_{\text{cm}}(Z)$, describes the exciton center of mass motion, and in the case of an infinite NW $\Psi_{\text{cm}}(Z) \sim \exp(iKZ)$, where $\hbar K$ is the exciton momentum along the NW axis. This replaces the second term in Eq. (4.20) by the exciton kinetic energy, $\hbar^2 K^2 / 2M_{n,k}^{n',k'}$.

Equation (4.20) allows us to numerically calculate the energy spectrum of 1D excitons created from any pair of electron and hole subbands. In this chapter, we will be interested primarily in the spectrum that arises from the lowest electron and hole subbands $1\Sigma_{1/2}^e$ and $1\Sigma_{1/2}^h$, and we will use the approach suggested by

Elliott & Loudon [33] to describe the spectrum of one-dimensional excitons in a strong magnetic field. They suggest approximation of the one-dimensional adiabatic potential by an effective one-dimensional potential, which has well-known Schrödinger equation solutions,

$$U_{\text{eff}}(z) = -\frac{e^2}{\kappa_m(|z| + \rho_{\text{eff}})} - \frac{A\rho_{\text{eff}} e^2}{\kappa_m(|z| + \rho_{\text{eff}})^2}, \quad (4.21)$$

where ρ_{eff} and A are the two fitting parameters. The medium dielectric constant κ_m is used in Eq. (4.21) so that the correct asymptotic form of the potential is maintained. For a 4-nm PbSe NW immersed in a medium with $\kappa_m = 2$, the numerically-calculated effective potential is described very well by the potential U_{eff} with $\rho_{\text{eff}} = 5.49R$ and $A = 2.73$, as seen in Fig. 4.3. The slight dependence of these fit parameters on NW size is shown in Fig. 4.4a and the much stronger dependence on κ_m is shown in Fig. 4.4b.

The energy spectrum and eigenfunctions of Eq.(4.20) with effective attractive potential $U_{\text{eff}}(z)$ can be obtained analytically. The eigenfunctions of each 1D exciton level, $\psi_\alpha(z)$, can be written as [32, 33]

$$\psi_\alpha(z > 0) = a_1 W_{\alpha, -\frac{1}{2}\sqrt{1-4A\alpha\rho}}(\tilde{z} + \tilde{\rho}) + a_2 M_{\alpha, -\frac{1}{2}\sqrt{1-4A\alpha\rho}}(\tilde{z} + \tilde{\rho}) \quad (4.22)$$

$$\psi_\alpha(z < 0) = \pm\psi_\alpha(|z|) \quad (4.23)$$

where $W_{\alpha,\beta}(x)$ and $M_{\alpha,\beta}(x)$ are the Whittaker functions, $\tilde{z} = 2z/(a_0\alpha)$, $\tilde{\rho} = 2\rho_{\text{eff}}/(a_0\alpha)$, $a_0 = \hbar^2\kappa_m/(\mu_{1/2,1}^{1/2,1}e^2)$ is the effective Bohr radius of a 1D exciton, and a_1 and a_2 are arbitrary coefficients. The sign of Eq. (4.23) is “+” for an even eigenfunction and “−” for an odd one. The coefficients a_1 , a_2 , and parameter α in Eq. (4.22) as well as the exciton binding energy:

$$\varepsilon_\alpha = -\frac{\hbar^2}{2\mu_{1/2,1}^{1/2,1}a_0^2\alpha^2} \quad (4.24)$$

are determined by the boundary conditions.

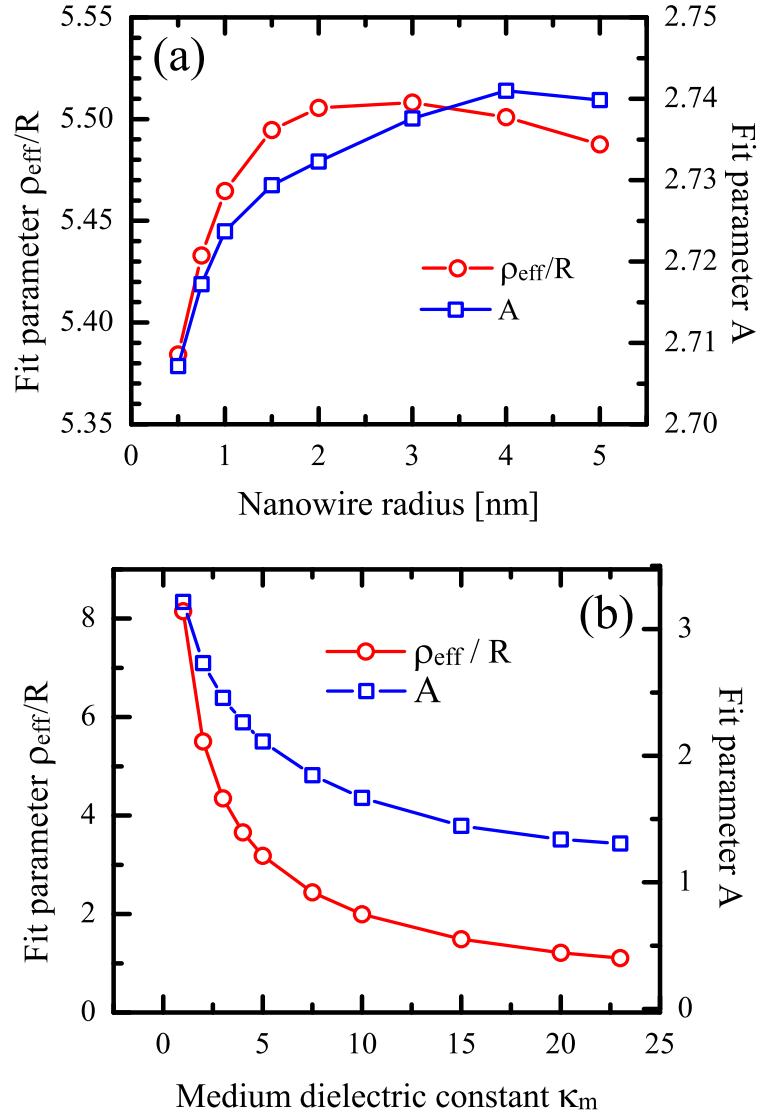


Figure 4.4: Fitting parameters used in the effective potential described by Eq. (4.21) in PbSe NWs of various radius and medium dielectric constant. The parameter is plotted vs. (a) nanowire diameter with $\kappa_m = 2$ (b) medium dielectric constant with $R = 2$ nm.

There are two boundary conditions to impose on the solution in Eq. (4.22): one at $z = z_e - z_h = \pm L$ and one at $z = 0$. We first consider infinite nanowires; the effects of finite length will be treated in the following section. In this case, the first boundary condition is satisfied by letting $a_2 = 0$, because $M_{\alpha, -\frac{1}{2}\sqrt{1-4A\alpha\tilde{\rho}}}(|\tilde{z}| + \tilde{\rho})$ diverges as $|\tilde{z}| \rightarrow \infty$. The second boundary condition, requiring $\psi_\alpha(z)$ to be either an even or odd function of z , determines α and the energy spectrum of the exciton. It was shown in Refs. [32, 33] that for excited doubly-degenerate exciton states, α takes almost-exactly integer values $\alpha = 1, 2, 3, \dots$ and that $\alpha \rightarrow 0$ for ground states with decreasing exciton transverse radius. Following Refs. [32, 33] we use ε_0 for the ground exciton binding energy.

Figure 4.5 shows the calculated binding energy of the ground exciton state ε_0 and the Coulomb self-interaction energies $E_{\text{self},e}^{1/2,1}$ and $E_{\text{self},h}^{1/2,1}$ of electrons and holes from the ground 1D subbands $1\Sigma_{1/2}^{e,h}$. The binding energy decreases dramatically with NW radius or external dielectric constant. The exciton binding energy in the narrowest NW surrounded with $\kappa_m \sim 2 - 3$ reaches values > 300 meV.

Surprisingly, however, the binding energy is almost exactly compensated by the electron and hole self-interaction terms, which leads to practical cancelation of most effects connected with the small dielectric constant of the surrounding medium. Because of this cancelation, the optical transitions between 1D subbands will be determined primarily by the energies calculated in Section 4.3. This result has important practical consequences. For example, the linear optical spectra of PbSe NWs will not be sensitive to the dielectric constant of the surrounding medium.

This cancelation is well-known in spherical semiconductor NCs. The exact cancelation of these three terms was shown for parabolic valence and conduction

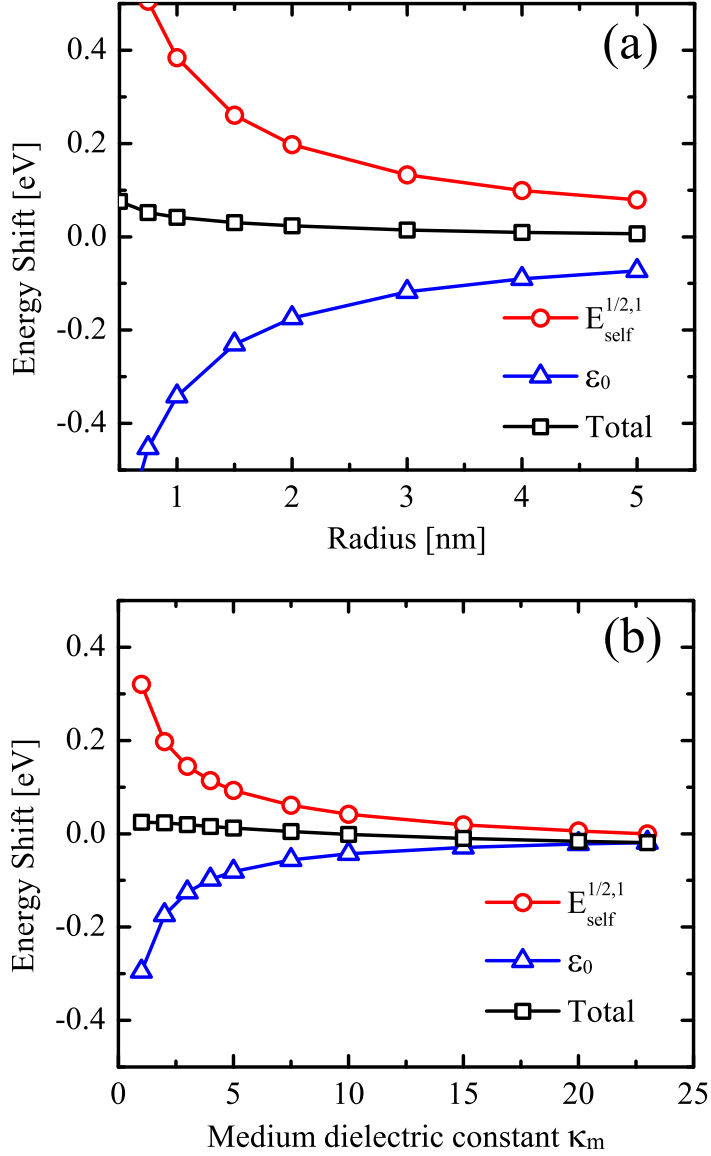


Figure 4.5: Coulomb energies calculated for (a) $\kappa_m = 2$ with varying R and (b) $R = 2$ nm with varying κ_m . Lines are the sum of the electron $E_{\text{self,e}}^{1/2,1}$ and hole $E_{\text{self,h}}^{1/2,1}$ self interaction energies (red circles); the electron-hole binding energy ϵ_0 (blue triangles); and their total (black squares).

bands in Ref. [34]. This is because in a parabolic-band approximation the wave function of electrons and holes are identical and depend only on the NC radius. As a result the electron and hole charge distributions exactly compensate each other at each point in the NC. If there is no local charge in the NC, there is no electric field outside of the NC, and the external medium does not affect the optical properties. This cancelation is nearly exact even when the electron and hole masses are different [35].

The cancelation of the Coulomb energies in the ground exciton of PbSE NWs can be attributed to a similar charge compensation. The mirror symmetry of the conduction and valence bands in PbSe makes the wave functions of the electron and hole transverse motion nearly identical. The similar values of effective masses along the NW axes also makes the electron and hole contributions to the 1D exciton wave function identical. It is interesting to note here that because of the large binding energy, the electron and hole in the exciton are remarkably tightly bound, with average separation only slightly larger than the NW radius. Fig. 4.6 shows the average separation, calculated as $\sqrt{\langle(z - \bar{z})^2\rangle}$, as a function of radius, with inset showing the wavefunction ψ_{1D} for the case of $R = 2$ nm. One can see that the average electron-hole separation in the exciton is an order of magnitude smaller than the 46 nm Bohr radius in bulk PbSe. Further calculations show that this unusual increase in the strength of the binding is due entirely to the 1D shape of the NR, and is only weakly affected by the dielectric contrast. For the weakest dielectric contrast when $\kappa_m = \kappa_s = 23$, the average separation increases slightly to ≈ 4 nm, still much closer to the 4-nm diameter than to the Bohr radius.

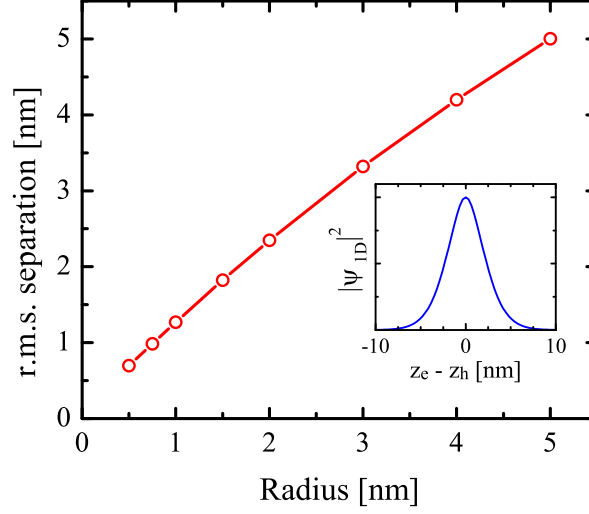


Figure 4.6: Dependence on PbSe NW radius of the average (r.m.s.) separation of the electron and hole in the 1D exciton. Inset shows the square of the ground exciton wavefunction $|\psi_{1D}|^2$ for a NW with 2 nm radius.

4.5.1 Finite length effects

For a nanorod, which has finite length, the relative and center-of-mass (CM) motions of the electron and hole can never be completely separated. If the NR is much longer than the radius of the 1D exciton, one can still approximately separate variables to create effective boundary conditions for the exciton CM motion. No other boundary condition (BC) is needed for the exciton separation coordinate, because the assumption is that the tightly-bound wavefunction is already zero well before any additional confinement is felt. On the other hand, the CM motion can be considered as the motion of a free particle confined in a 1D box of length L . If the box is much larger than the exciton radius one can apply the standard boundary conditions on Ψ_{cm} to obtain the well-known spectrum $E_{\text{cm}}(l) = \hbar^2 \pi^2 l^2 / (2M_{1/2,1}^{1/2,1} L^2)$, where l is the level number.

Even though this CM boundary condition makes intuitive sense, it is difficult

to justify, because the true BCs are for the electron and hole individually. To test our assumption, we calculated the CM wavefunctions and energies numerically by solving the two-particle Schrödinger equation with the correct impenetrable boundary conditions on the electron and hole individually. Details of the calculation are in Appendix B.3. Fig. 4.7 shows the square of the 1D wavefunctions, $|\Psi_{1D}|^2$, calculated both numerically and analytically as a function of z_e and z_h . Note that these wavefunctions are 2D because the position of both the electron and hole must be specified. Wavefunctions align along the lower-left to upper-right diagonal in these figures because those are the positions where the electron and hole are close together, *i.e.* when $z_e \approx z_h$.

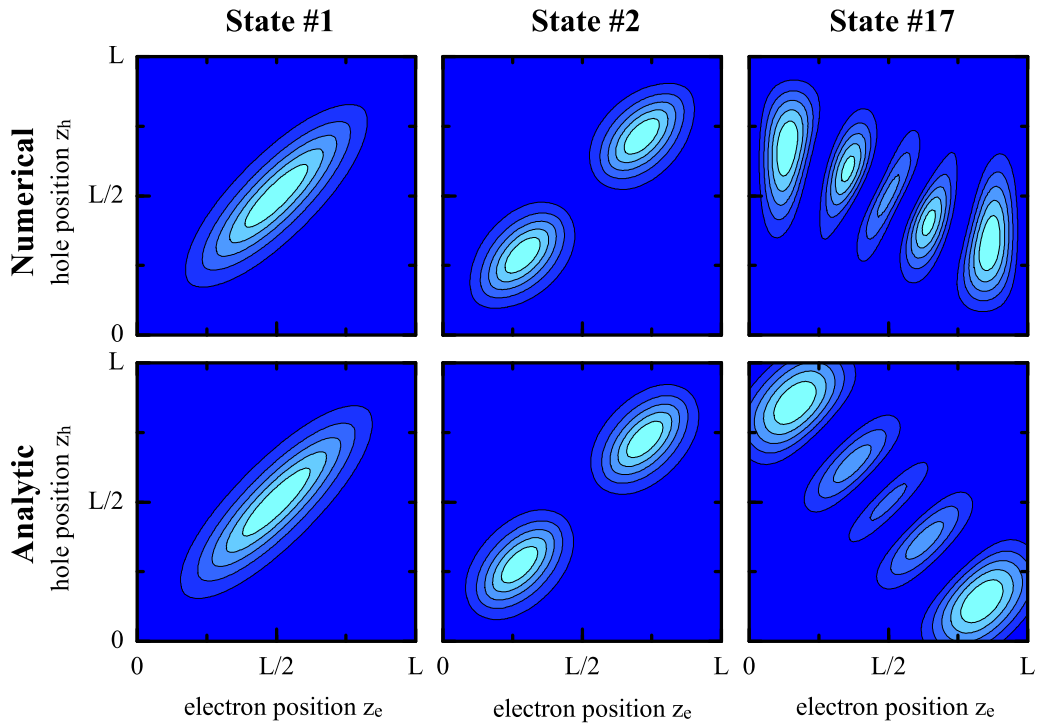


Figure 4.7: Comparison of the numerically and analytically calculated 1D exciton wavefunctions $|\Psi_{1D}|^2$. Each subplot has axes z_e and z_h ranging along the length of the nanorod from 0 to L . The two lowest energy states and the 17th state are shown.

For the lowest two exciton states $|\Psi_{1D}|^2$ shows good agreement between the

numerical model and the analytic calculation. This is because the electron and hole are strongly localized around each other and do not feel the effects of confinement at the edges of box. On the other hand, by the 17th excited state, also shown in Fig. 4.7, the numerical and analytical calculations disagree greatly. This is because the higher kinetic energy of this state causes the wavefunction to reach the edges of the box and feel confined. And, as a result, it begins to look more like that of independent particles, oriented along their own coordinates, z_e and z_h . In general, our analytic model shows good agreement for the lowest ≈ 10 states for each pair of nanowire bands.

Interestingly, the numerically calculated wavefunctions and energies were best matched to those obtained for a free particle with an effective mass of the exciton which is confined in the 1D box of length $L_{\text{cm}} = L - R$. That is, the boundary condition for the bound electron-hole pair is just as you would expect, except confined in a slightly smaller region of size $L - R$. The existence of such a simple expression is probably connected with the approximately-equal effective masses of the electrons and holes and their small separation in PbSe NRs. The first few numerically-calculated energy levels are shown in Fig. 4.8, along with the analytic energies $E_{\text{cm}} = \hbar^2 l^2 \pi^2 / (2M_{1/2,1}^{1/2,1} L_{\text{cm}}^2)$ for various confinement lengths L_{cm} . This modified CM length works well for all rod sizes studied, as long as the NR aspect ratio is $\gtrsim 2$.

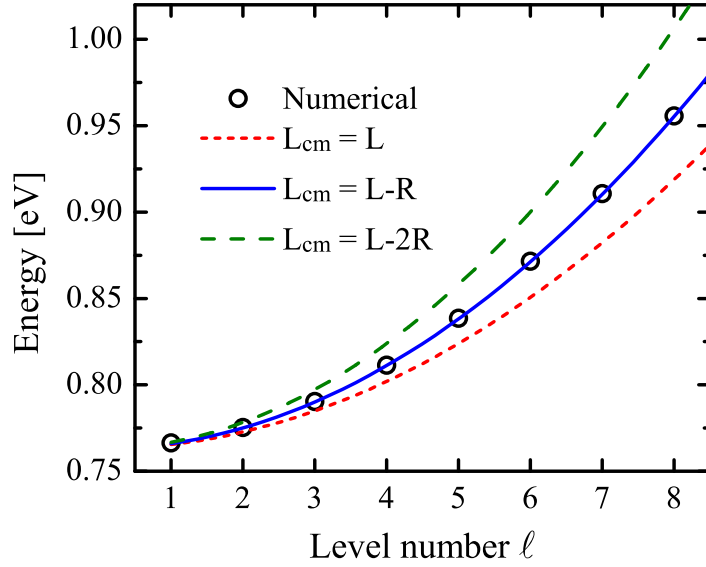


Figure 4.8: Numerically-calculated energies for the lowest few exciton states in a 4 x 20 nm PbSe NR (black circles). The lines are the energies from the analytic model using two different confinement lengths for the center of mass.

4.5.2 Oscillator strength of the interband optical transitions

The decrease of the electron-hole separation within a 1D exciton leads to a dramatic increase of the optical transition strength. It was shown by Elliott & Loudon [33] that the oscillator strength of practically the entire spectrum of 1D excitons becomes concentrated in the ground exciton state. The expression for the transition strength in PbSe NRs can be obtained by combining the results derived for PbSe NCs [24] and CdSe NRs [7]. The total oscillator strength O_{total} can be written as a product $O_{\text{total}} = O_{\perp} O_{\parallel}$, where the tranverse oscillator strength is [24]

$$O_{\perp} = \frac{2P_l^2}{9m_0\hbar\omega} \left| \int_0^R \rho d\rho \int_0^{2\pi} d\phi \begin{bmatrix} \Psi_h^{1/2,1} \\ \Psi_e^{1/2,1} \end{bmatrix}^{\dagger} \begin{bmatrix} 0 & \sigma_z \\ \sigma_z & 0 \end{bmatrix} \begin{bmatrix} \Psi_h^{1/2,1} \\ \Psi_e^{1/2,1} \end{bmatrix} \right|^2 \quad (4.25)$$

with $\hbar\omega$ the total energy of the optical transition. We have neglected the second term from Ref. [24], as it is negligible except for very small NRs, where the envelope function approximation likely breaks down anyway. The oscillator strength of the 1D exciton [7] is

$$O_{\parallel} = |\psi_{1D}(z=0)|^2 \left| \int_0^L dZ \Psi_{\text{cm}}(Z) \right|^2 \quad (4.26)$$

where we normalize the 1D exciton wave function such that

$$\int_{-L}^L dz \int_0^L dZ |\psi_{1D}(z) \Psi_{\text{cm}}(Z)|^2 = 1 . \quad (4.27)$$

The transverse oscillator strength provides the selection rule that there is no change in the z -component of the angular momentum, $\Delta n = 0$, while the longitudinal component focuses the oscillator strength into the ground exciton state. This is because optical transitions are only allowed to the even states of the exciton CM motion with $l = 1, 3, 5, \dots$, and the oscillator strength decreases as $1/l^2$. Even the second allowed transition will be 9 times weaker than the lowest transition. This has practical implications for the optical absorption spectra. Even though the density of allowed transitions increases dramatically with energy in NRs, most of the oscillator strength is concentrated in the lowest-energy transition for each pair of NR subbands. Thus, isolated peaks should still be observable in experimental spectra.

4.6 Experiment

4.6.1 Difficulties encountered in nanorod syntheses

Although the synthesis of lead salt nanowires was reported several years ago [36], the fabrication of high quality lead-salt nanorods has proved challenging. Various methods have been described in the literature, but they have all proved too challenging to reproduce. Briefly here we will describe the difficulties encountered, and speculate on the reasons why.

PbSe NRs were synthesized with noble metals as seeds [37], which were reported to show moderate uniformity in TEM, but poor optical quality. Nevertheless, we briefly pursued this method, in hopes of somehow overcoming their deficiencies with either improved synthesis methods or different optical probes. The first step of the synthesis is to create gold nanoparticles as seeds, which then catalyze the 1D growth of the nanorods off of their surface. As we discovered, producing uniformly sized gold nanoparticles is an art of its own.

The main attraction, but also the main deficiency, of the gold nanoparticle synthesis is its simplicity. Specifically, the reaction can be performed at room temperature in ambient environments and is a two-phase method, involving two liquids which do not mix. The two precursors are dissolved, one in each liquid, and the reaction occurs at the liquid interface. This inherently causes uncertainty in the reaction, because one is forced to choose between either stirring the solutions rapidly to achieve uniform concentrations of reactants in each liquid, or stirring slowly to have a smooth and uniform liquid interface. As a result, the precise stirring speed and method becomes critical. Gold nanoparticles were successfully

produced with this method, capped with a large variety of ligands, but in all cases the size distribution was terrible: $\Delta R/R > 1$. because uniformity in the size of the gold seed is required for uniform nanorod growth, we stopped pursuing this direction.

We next tried a method to produce PbS nanorods via modification of the ligands used during the synthesis [38]. Very high quality crystalline structures were reported in that reference, though without mention of their optical properties. The synthesis is more similar to that of PbSe (not PbS) QDs, in that elemental sulfur is used as a precursor. Importantly, elemental sulfur is not nearly as reactive as selenium, which is why the much more reactive TMS is used as the typical sulfur precursor in nanocrystal synthesis. But, according to this paper, by adding oleylamine to the synthesis, the reactivity is increased and interesting structures, including nanorods, can be created.

We encountered many problems with this method. First, the solubility of sulfur is quite bad in the solvents used, and depends on the oxygen content of the solvent. Depending on the precise type of elemental sulfur (pellets, powder, or flakes) and the method of mixture (sonicating, stirring, heating, in ambient or N_2 environment) different color products were created (yellowish, clear, grey, even once dark purple.) The paper neglected to mention which is desired. We found that only for the clear mixture, produced with the best quality powdered sulfur by sonicating in N_2 , were any nanoparticles produced at all. But instead of producing nanorods, large (10-20 nm) PbS cubes were produced (see Fig. 4.9). In addition, the oleylamine was found to be irrelevant for the synthesis. Producing large cubic particles is expected with precursors with low reactivity, and is also mentioned by Warner [38] as a possible product depending on the reactivity of the sulfur in the

synthesis. It became apparent that the problem lay in our oleylamine, which was evidently not increasing the reactivity of the sulfur as desired. At only 70% purity, it is my opinion that the paper relied on a specific impurity no longer found in the oleylamine from that company. We attempted using oleylamine from other companies, with similar negative results. Eventually, we also stopped pursuing this direction.

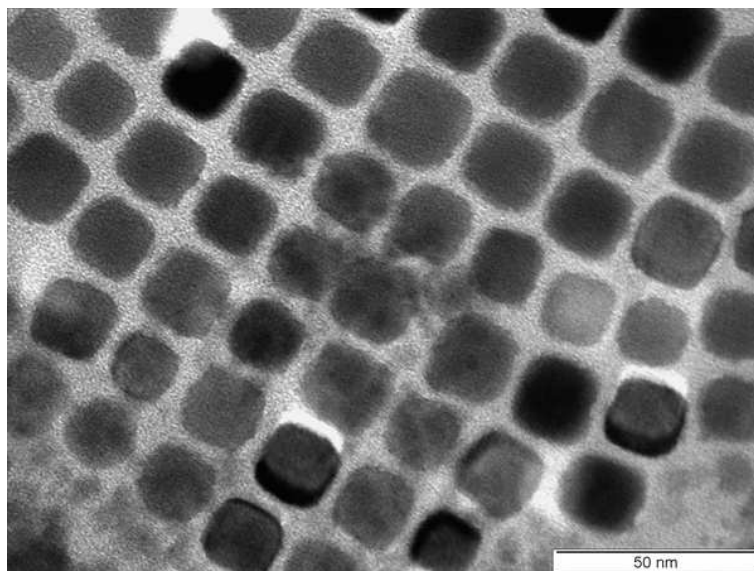


Figure 4.9: TEM image of the PbS cubes formed during an attempted nanorod synthesis.

Our next attempt was to reproduce the synthesis of brightly emitting and extremely narrow PbS nanorods [39], using a seemingly simple single-precursor reaction. Ideally, a single chemical, lead hexadecylxanthate (Pb-HDX), which contains both the lead and sulfur, is heated to around 60 °C, at which point it breaks down and forms nanorods. So called “single-pot” syntheses are ideal for their simplicity, especially because this one is performed so close to room temperature. Nevertheless, there were many problems again associated with this method.

The primary problem is that HDX is not sold commercially, and required a separate synthesis itself. The fabrication method is only briefly described in the

literature, and followup characterization methods are not described at all; but eventually a method was developed by incorporating parts of other related methods [40, 41, 42, 43] and is described in Appendix A.2. In short, potassium hexadecylxanthate (K-HDX) is first produced and purified, and then the potassium is replaced with lead by reacting with lead nitrate, followed by an additional purification. Though the K-HDX was found to be very stable in ambient storage conditions, the Pb-HDX was found to be very unstable, often decomposing during the purification, with evident color changing from the color of Pb-HDX (whitish yellow) to that of lead sulfide (brownish to black). Still, many batches were successfully made and then used in attempted nanorod synthesis.

This tendency for Pb-HDX to decompose proved to be the primary problem with this method. Very high concentrations were required to produce nanorods, so high in fact that the Pb-HDX would not dissolve in the solvent at room temperature. Instead, in the best case, it would dissolve and then immediately decompose at nearly 60 °C, making this process entirely not reproducible or controllable. In worse cases, it would partially react before that temperature, noticeably changing color before dissolving, resulting in even worse control. As a result, even though PbS nanorods were produced with this method, they came along with a whole zoo of other types of nanocrystals, and their sizes and shapes were completely uncontrolled (Fig. 4.10). Eventually this method was also dropped, as there did not seem to be any possible method to improve the lack of control. Also, upon more careful examination of the paper, the reported bright emission and strong absorption peak are most likely from surface trap states, as it is very close to reported absorption and emission from lead-ligand complexes [44] and would be somehow blue-shifted from the absorption and emission of PbS monomers [45].

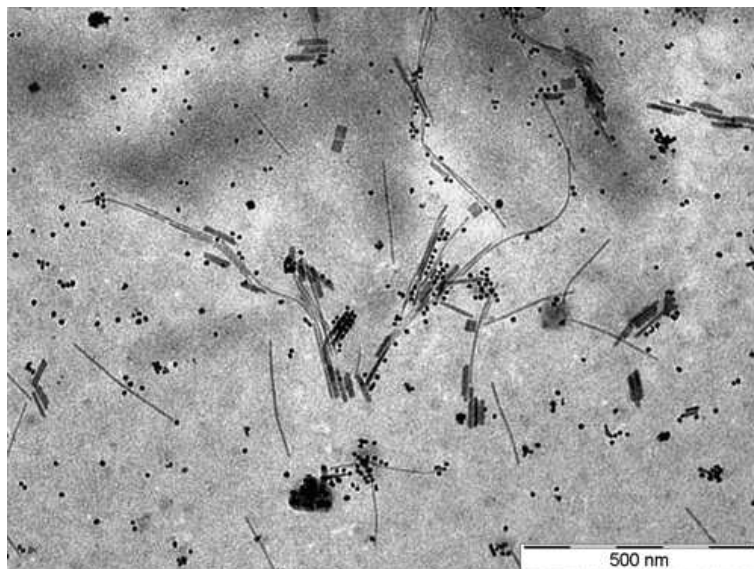


Figure 4.10: TEM image of the result of attempted PbS nanorod synthesis *via* decomposition of Pb-HDX. Both straight and curved thin nanorods along with fatter nanorods, cubes, spheres, and aggregates of PbS are visible. This image was nicknamed the “nano-zoo”.

Finally, we decided that a new synthesis method was required. With knowledge of the deficiencies learned from the other syntheses, we knew that it should satisfy the following criteria: it should avoid chemicals with low purity, ideally use well-understood precursors with high reactivity, and be as similar as possible to existing well-established methods. We began a collaboration with the Murray group at the University of Pennsylvania, because of their demonstrated ability to work magic [46, 47, 36] to produce robust nanocrystal syntheses. With their guidance, a synthesis was developed within weeks that satisfied all criteria.

4.6.2 Nanorod synthesis using TDP

The simplest way to describe the synthesis is that it is identical to the well-established PbSe QD method described in chapter 2.5 except that trioctylphos-

phine (TOP) is replaced by Tris(diethylamino)phosphine (TDP). Thus, it shares all of the simplicity and expected robustness of that previous method. The NR synthesis was carried out using standard Schlenk-line techniques under dry nitrogen. Tris(diethylamino)phosphine (TDP, Aldrich, 97%), oleic acid (OA, Aldrich, 90%), 1-octadecene (ODE, Aldrich, 90%), squalane (Aldrich, 99%), amorphous selenium shots (Se, Aldrich, 99.999%), and lead(II) oxide (PbO, Aldrich, 99.9%) were used as purchased without further purification. Anhydrous ethanol, chloroform, acetone, hexane, and tetrachloroethylene (TCE) were purchased from various sources. To prepare 1.0 M stock solutions of TDPSe, 7.86 g of Se was dissolved in 100 mL of TDP at least one day before the synthesis.

Typically, 0.22 g of PbO was dissolved in 5 mL of squalane in the presence of 1 mL OA. (Squalane can be replaced by ODE.) After drying under nitrogen at 150 C for 30 min, the solution was heated to 170 C and 3 mL of a 1 M TDPSe solution in TDP was injected under vigorous stirring. Once the reaction finished, the reaction mixture was cooled to room temperature using a water bath. The crude solution was mixed with hexane and precipitated by ethanol. The precipitated NRs were isolated by centrifugation (at 5000 rpm for 3 min) and redispersed in chloroform or other organic solvents. Size-selective precipitation can be carried out to obtain better monodispersity of NRs samples using chloroform/acetone or other solvent/nonsolvent pairs. This process is explained in more detail in Ref. [48]. An example HRTEM image is shown in Fig. 4.11.

The size of the synthesized NRs was determined from transmission electron microscopy. In-plane powder X-ray diffraction shows that the NRs grow along the $\langle 100 \rangle$ direction [48]. Absorption was measured on a Shimadzu UV-3101PC spectrophotometer at room temperature. Emission spectra were recorded at room

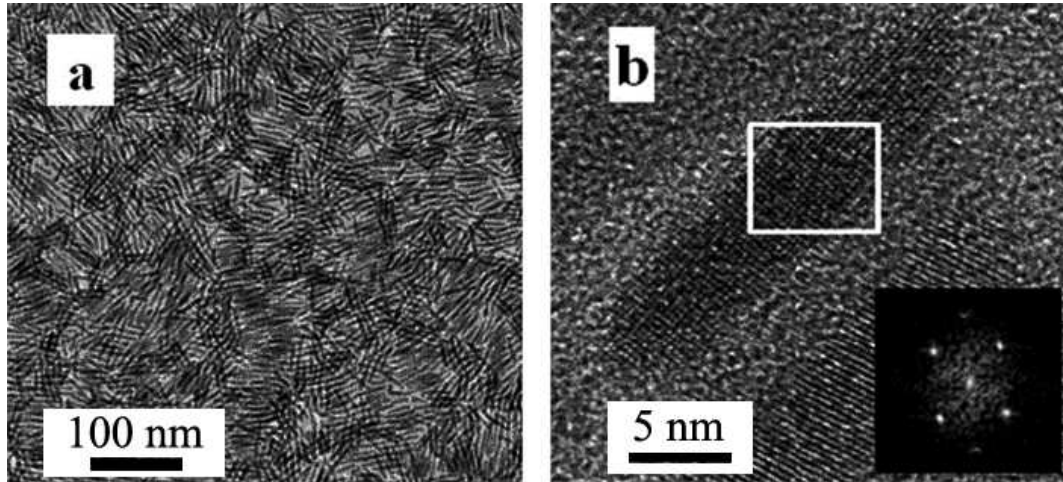


Figure 4.11: (a) TEM image of typical PbSe NRs. (b) High-resolution TEM image of an individual PbSe NR. (Inset: FFT image of the (100) face.)

temperature with an infrared fluorimeter equipped with a 200-mm focal length monochromator, a single mode fiber coupled laser source (S1FC635PM, 635 nm, Thorlabs, Inc) as the excitation source, and an InGaAs photodiode (New Focus Femtowatt model 2153). Fluorescence lifetime was measured using an InP/InGaAs PMT (Hamamatsu H10330A-75) with 120-fs excitation pulses from a Ti:sapphire regenerative amplifier (Spectra-Physics Hurricane) with 1 kHz repetition rate. NRs were dissolved in tetrachloroethylene (TCE) for all measurements to avoid spurious absorbance in the near-IR. Quantum yield measurements were performed using an integrating sphere, with the method described in Ref. [49].

4.6.3 Absorption Spectra

First, we will highlight the qualitative differences between the absorption spectra of NRs and spherical NCs. Figure 4.12 shows the absorption spectrum of 3.3 nm diameter x 12 nm length PbSe NRs along with that of 4.4 nm diameter spherical NCs, chosen to have a nearly identical first absorption peak. The spectrum of

the NRs has fewer obvious features than the NC spectrum. The first peak in the NR spectrum has a broad high energy side, even though its narrower low energy side is nearly identical to that of the NCs (inset of Fig. 4.12). Both of these observations indicate the presence of more densely-spaced transitions in the NR spectrum, which have the effect of smoothing out the peaks. Interestingly, the second NC peak appears where there is a dip in the NR spectrum.

The broadening of the NR absorption peak seen in Fig. 4.12 is connected with the dispersion of NR diameter and length. Our best PbSe NR samples have around 5% size distribution in radius, but a much larger 20% in length. This large length polydispersity will blur out many of the NR transitions in an ensemble, except for those that are roughly independent of length—specifically, the lowest energy exciton for each pair of NW subbands. Fortunately, this is also the transition predicted to have the largest oscillator strength. As we have shown above, the energies of the optical transitions of the ground exciton states practically coincide with the energies between non-interacting electron and hole subbands, even though their respective wave functions differ greatly. This greatly simplifies the interpretation of the absorption spectra of NRs.

We performed second-derivative analysis on the absorption spectra to determine the transition energies accurately. To avoid the problems inherent in this method [50], only the peaks in the second-derivative spectra that correspond to obviously-visible peaks in the measured spectra were used. NRs produced by our first syntheses showed instability in solution and would slightly aggregate during the absorption measurement. This adds a moderate scattering background, so only the absorption peak location is recorded for these samples. NRs synthesized more recently are more stable, and at least four peaks can be discerned, with an

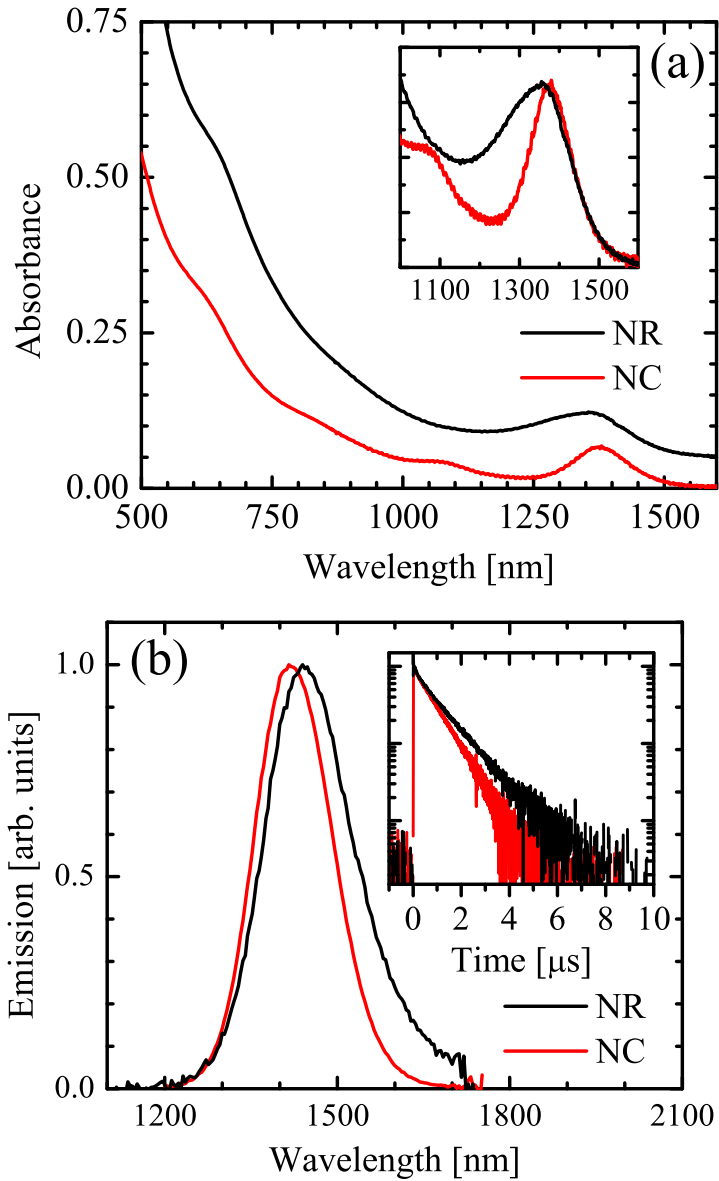


Figure 4.12: (a) Absorption spectra of PbSe NRs (black line, vertically offset for clarity) and spherical PbSe NCs (red line) are compared. The inset shows detail of the first peak. (b) Emission spectra and fluorescence decays measured at the emission peak (inset) of the same two samples.

additional peak in the three samples with narrowest size distribution. Fig. 4.13a has an example measured spectrum of a 3.9 nm diameter x 17 nm length PbSe NR that shows all five peaks, and the locations of all measurable peaks from all samples are shown in Fig. 4.13b. The measured peaks are plotted *vs.* $D^{-3/2}$ following the similar graph in Ref. [51]. This power of the diameter is chosen to make the trend linear over the measured range, allowing rough extrapolation to bulk as $D^{-3/2} \rightarrow 0$. In this manner, the peaks originating from the L-point and Σ -point are easily distinguished.

Quantitative theoretical description of the size-dependent absorption spectra of PbSe NRs shown in Fig. 4.13 requires a set of 6 room temperature energy band parameters for this semiconductor: m_t^\pm , m_l^\pm , and $P_{t,l}^2$. The parameters extracted from low temperature cyclotron resonance and interband magneto-optical experiments in bulk PbSe [52] describe quite well the average two-dimensional effective mass of electrons and holes at the bottom of the conduction band and the top of the valence band, respectively. The fitting procedure that gives this set is not sensitive, however, to the separation of $1/m_{l,t}$ and the $2P_{l,t}^2/m_0^2 E_g$ terms, and describes well only the sum of these terms, because the all measurements are conducted at the narrow energy range comparable with the PbSe energy gap. This procedure is also not very sensitive to the anisotropy of the carrier energy spectra, because a magnetic field averages out the 2D motion of electrons and holes. On the other hand, in order to predict nanocrystal energy levels quantitatively, both the separation of components of the effective masses and the band anisotropy are crucial. Finally, the energy band parameters are expected to be temperature dependent. Thus, we conclude that parameters inferred from cyclotron resonance and magneto-optical measurements might not describe the energy spectra of NRs and NCs measured at room temperature.

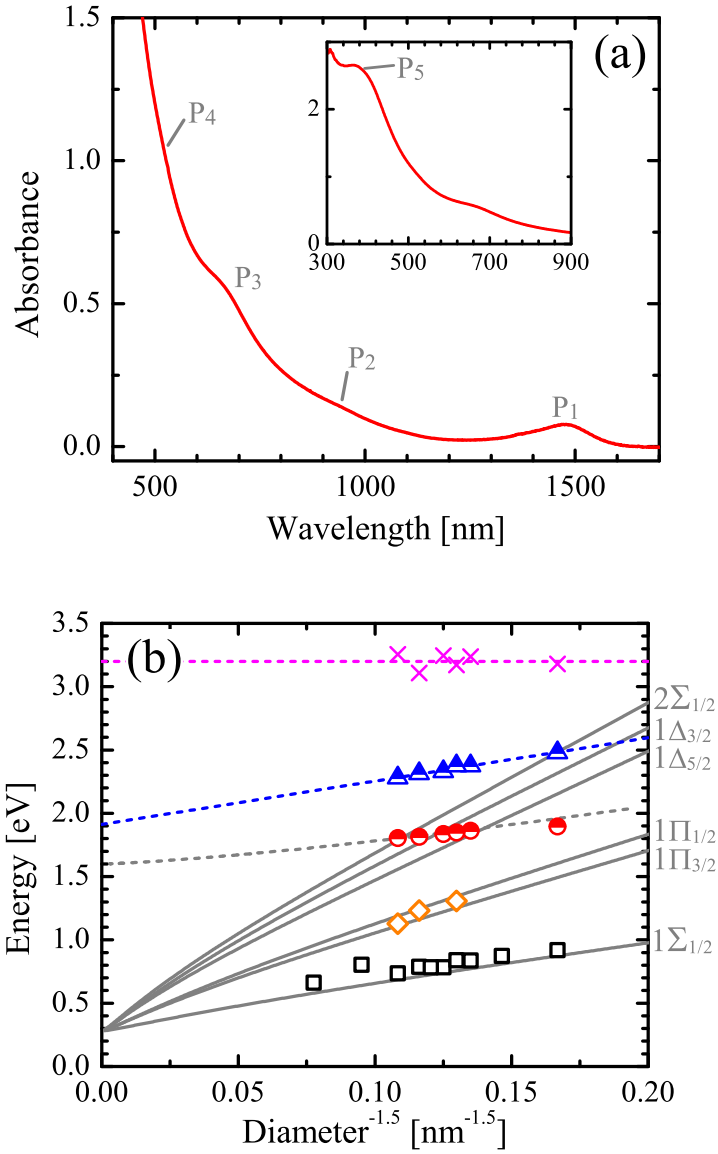


Figure 4.13: (a) Example absorption spectra of a 3.9 x 17 nm PbSe NR. Inset shows the same data, but on a scale where the 5th peak is visible. (b) Peaks in 2nd derivative spectrum as a function of NR diameter (symbols), calculated allowed transitions (grey lines), simple parabolic effective mass calculation around the Σ -point (dashed grey line), and linear fits (colored dashed lines.)

In principle, spatial confinement of carriers in nanostructures provides a more-sensitive way to determine the energy band parameters, due to the large modification of the energy spectra of confined carriers. With this motivation, we used the previously-measured absorption spectra of PbSe NCs in Refs. [47, 53, 54, 55, 56, 51] and extracted room-temperature band parameters using a global fitting procedure. Importantly, this new set of parameters not only quantitatively describes the low-energy transitions of PbSe NCs, but may also help resolve the long-standing controversy over the symmetry of the second peak in the NC absorption spectra (see Appendix B.4). These band parameters (Table 4.1) are used in all graphs presented in this work.

Table 4.1: Energy band parameters that provide the best fits to the room temperature data from PbSe NCs. The left columns show the transverse band components, while the right columns show the ratio of transverse to longitudinal components.

Name	Ref. [52]	Best Fit	Aniso. ratio	Ref. [52]	Best Fit
m_t^+/m_0	0.29	0.59	m_l^+/m_t^+	1.28	1.6
m_t^-/m_0	0.27	0.79	m_l^-/m_t^-	3.53	1.6
$2P_t^2/m_0$	3.6 (eV)	4.25 (eV)	P_t^2/P_l^2	1.82	3.0

The theoretical size dependence of the optical transitions in PbSe NRs is calculated within our 4 band model and shown in Fig. 4.13b by solid lines. The lowest two transitions agree well with the theory. The third predicted transition is not observed, possibly owing to its proximity to other strong transitions in our NR samples. The third and fourth peaks are strong transitions that do not appear to be associated with the L-point. Their energies extrapolate back to the Σ -point energy. The third peak is fit well by the same parabolic band model used to model spherical PbSe NCs, and thus we assign this transition to the lowest-energy excitonic state at the Σ point. This line was calculated for both spheres and rods with $m_\Sigma^e = m_\Sigma^h = 0.45m_0$ and $E_g(\Sigma) = 1.65$ eV. Without more-detailed knowledge of the band structure there, we cannot predict the excited states with any

accuracy. Thus, the identity of the fourth transition cannot be determined, but as the energies approach the same 1.65-eV bulk value, it is reasonable to tentatively attribute it to a higher-energy exciton from the Σ point. Finally, the fifth peak was perhaps the strongest in the absorption spectra, but showed no size dependence. We tentatively ascribe this to a metal-complex transition on the surface of the nanocrystal based on its proximity to absorption peaks of Pb(II) complexes [44]. The identities of these transitions are summarized in Table 4.2.

Table 4.2: Transitions observed in the absorption spectra of PbSe NRs.

Label	Assigned Transitions
P_1	$1\Sigma_{1/2}^h \rightarrow 1\Sigma_{1/2}^e$
P_2	$1\Pi_{3/2}^h \rightarrow 1\Pi_{3/2}^e$ and $1\Pi_{1/2}^h \rightarrow 1\Pi_{1/2}^e$
P_3	Σ -point ground state
P_4	Σ -point excited state (?)
P_5	Surface metal complex mode

The fluorescence spectra and decays (Fig. 4.12b) are nearly identical for NCs and NRs, with a slightly larger Stokes shift in the NRs along with a slightly broader peak. The ensemble quantum yield of the nanorods is around 15%, around half that of the NCs. This might indicate that the radiative lifetime of the rods is longer than that of the NCs, but it is also possible that the QY reflects an ensemble with 15% emitting and 85% non-emitting rods.

Two effects would be expected to modify the radiative lifetime in nanorods. First, because the radiative lifetime is inversely proportional to the oscillator strength, the increased electron-hole correlation in NRs should decrease the lifetime compared to NCs. Second, the effect of screening is reduced in NRs, which is believed to be the cause of the long lifetime in PbSe NCs[54]. Approximating the NR as a dielectric prolate spheroid, the screening will substantially decrease along the rod axis, while slightly increasing along the other two axes, with an overall ef-

fect of a reduction in screening of the lifetime. Compared to a spherical NC of the same diameter, the larger oscillator strength and the reduced screening should each produce about a factor of 3 reduction in lifetime in NRs with typical aspect ratios. Together this amounts to almost an order of magnitude reduction, and should be measurable even considering other sample-related uncertainties. However, the measured lifetime (Fig. 4.12b) is nearly identical in NCs and NRs. This discrepancy is not understood. It might be explained by a dark ground exciton state that controls the photoluminescence decay in PbSe NRs and NCs, with the same activation mechanism in both structures. To be thorough, the nonradiative rate must be determined, and completing this along with exploring this phenomenon is a topic of future work.

4.7 Discussion and Conclusions

Our model of the electronic structure of lead-salt NRs is based on the 4 band $\mathbf{k} \cdot \mathbf{p}$ Hamiltonian suggested in Ref. [27], using the standard boundary condition of a vanishing envelope wave function at the NR surface. All calculations are conducted within a cylindrical approximation. To use this model for description of various properties of NRs or NWs, one needs to know a set of the 6 temperature-dependent band parameters that describe a specific bulk lead-salt semiconductor. For the PbSe NRs studied in this chapter, we extracted the set of room-temperature parameters from analysis of the size-dependence of previously-measured room temperature absorption spectra of spherical PbSe NCs.

The most significant conclusion of this work is that the fundamental excitations in PbSe NRs are one-dimensional excitons under each pair of optically coupled

electron–hole subbands. The binding energy of the ground exciton state, which accumulates the most oscillator strength, increases with decreasing NR thickness and reaches 400 meV in the narrowest rods. Surprisingly, the large binding energy of the exciton is almost exactly compensated by the self–interaction of electrons and holes with their own images, which makes the energies of the optical transitions nearly independent of the solvent dielectric constant. Although the finite length of NRs affects the spacing between excited exciton states, it has a negligible effect on the energy of the exciton ground states.

With the set of PbSe band parameters extracted from spherical NC absorption spectra (Table 4.1), the model presented here describes the absorption spectra of PbSe NRs, and potentially resolves some troublesome aspects of $\mathbf{k} \cdot \mathbf{p}$ theory of spherical PbSe NCs. The energy of the optical transitions to the exciton ground states calculated within a cylindrical approximation match the two lowest-energy transitions observed experimentally. Although the effect of anisotropy is important for description of the absorption in spherical PbSe NCs, it is diminished in NRs (see Appendix B.1 & B.4), and the energy of the first two transitions is unaffected by it.

The absorption spectra of PbSe NRs have another remarkable feature. The size dependence of the third and fourth absorption peaks is strong evidence that they originate from the Σ point of the Brillouin zone. Similar states connected with the Σ point were observed previously in the absorption spectra [51] and in the hot carrier dynamics [57] of spherical PbSe NCs. These observations provide clear experimental evidence that even in the smallest nanostructures with diameter only 3 nm components of wave functions from distinct critical points (L and Σ , in this particular case) are not mixed if they are well-separated energetically. This

experimental fact provides strong justification for the applicability of the multiband effective mass approximation in such small nanostructures.

The predicted strong increase in electron–hole Coulomb interaction in PbSe NWs should have major implications for other properties. This enhancement should increase the rate of the nonradiative Auger recombination as well as the rate of the inverse process, impact ionization. A high rate of impact ionization or efficient multiple exciton generation, combined with good conductivity that might be expected in PbSe NWs, suggests that these structures may be promising for photovoltaic applications.

To summarize, we have developed a theory that describes both the energy spectra of individual electrons and holes and the absorption spectra of lead–salt NWs and NRs. Calculations show that even though spatial and dielectric confinement dramatically increase the exciton binding energy, the absorption spectra of PbSe NWs and NRs are practically unaffected, which should lead to insensitivity of these spectra to the surrounding media. The size dependence of lowest absorption peaks measured in PbSe NRs is very well described by the developed theory. It should be straightforward to apply this model to PbS and PbTe NRs.

BIBLIOGRAPHY

- [1] M. Kuno, *Phys. Chem. Chem. Phys.* **10**, 620 (2008).
- [2] Y.-w. Jun, J.-s. Choi, and J. Cheon, *Angew. Chem. Int. Ed.* **45**, 3414 (2006).
- [3] C. Burda, X. Chen, R. Narayanan, and M. A. El-Sayed, *Chem. Rev.* **105**, 1025 (2005).
- [4] E. C. Scher, L. Manna, and A. P. Alivisatos, *Philos. Trans. R. Soc. London, Ser. A* **361**, 241 (2003).
- [5] E. A. Muljarov, E. A. Zhukov, V. S. Dneprovskii, and Y. Masumoto, *Phys. Rev. B* **62**, 7420 (2000).
- [6] E. A. Mulyarov and S. G. Tikhodeev, *J. Exp. Theor. Phys.* **84**, 151 (1997).
- [7] A. Shabaev and Al. L. Efros, *Nano Lett.* **4**, 1821 (2004).
- [8] U. Bockelmann and G. Bastard, *Phys. Rev. B* **45**, 1688 (1992).
- [9] J. Sun, W. E. Buhro, L.-W. Wang, and J. Schrier, *Nano Lett.* **8**, 2913 (2008).
- [10] M. Califano and A. Zunger, *Phys. Rev. B* **70**, 165317 (2004).
- [11] C.-Y. Yeh, S. B. Zhang, and A. Zunger, *Phys. Rev. B* **50**, 14405 (1994).
- [12] A. Franceschetti, L. W. Wang, G. Bester, and A. Zunger, *Nano Lett.* **6**, 1069 (2006).
- [13] M. P. Persson and H. Q. Xu, *Appl. Phys. Lett.* **81**, 1309 (2002).
- [14] M. P. Persson and H. Q. Xu, *Nano Lett.* **4**, 2409 (2004).
- [15] M. P. Persson and H. Q. Xu, *Phys. Rev. B* **70**, 161310 (2004).
- [16] Y. M. Niquet, A. Lherbier, N. H. Quang, M. V. Fernandez-Serra, X. Blase, and C. Delerue, *Phys. Rev. B* **73**, 165319 (2006).
- [17] J.-C. Charlier, X. Blase, and S. Roche, *Rev. Mod. Phys.* **79**, 677 (2007).

- [18] M. V. Fernandez-Serra, C. Adessi, and X. Blase, Phys. Rev. Lett. **96**, 166805 (2006).
- [19] U. Landman, R. N. Barnett, A. G. Scherbakov, and P. Avouris, Phys. Rev. Lett. **85**, 1958 (2000).
- [20] B. F. Habenicht, C. F. Craig, and O. V. Prezhdo, Phys. Rev. Lett. **96**, 187401 (2006).
- [21] M. Bruno, M. Palumbo, A. Marini, R. Del Sole, and S. Ossicini, Phys. Rev. Lett. **98**, 036807 (2007).
- [22] L. Brus, Nano Lett. **10**, 363 (2010).
- [23] F. W. Wise, Accounts Chem. Res. **33**, 773 (2000).
- [24] I. Kang and F. W. Wise, J. Opt. Soc. Am. B **14**, 1632 (1997).
- [25] V. I. Rupasov, Phys. Rev. B **80**, 115306 (2009).
- [26] J. O. Dimmock and G. B. Wright, Phys. Rev. **135**, A821 (1964).
- [27] D. L. Mitchell and R. F. Wallis, Phys. Rev. **151**, 581 (1966).
- [28] A. L. Efros and A. L. Efros, Sov. Phys. Semicond. **16**, 772 (1982).
- [29] J. D. Jackson, *Classical Electrodynamics Third Edition*, 3rd ed. (Wiley, New York, 1998).
- [30] W. R. Smythe, *Static and Dynamic Electricity* (McGraw-Hill, New York, 1950).
- [31] L. E. Brus, J. Chem. Phys. **80**, 4403 (1984).
- [32] R. Loudon, Am. J. Phys. **27**, 649 (1959).
- [33] R. J. Elliott and R. Loudon, J. Phys. Chem. Solids **15**, 196 (1960).
- [34] S. Schmitt-Rink, D. A. B. Miller, and D. S. Chemla, Phys. Rev. B **35**, 8113 (1987).

- [35] Al. L. Efros and A. V. Rodina, *Solid State Commun.* **72**, 645 (1989).
- [36] K.-S. Cho, D. V. Talapin, W. Gaschler, and C. B. Murray, *J. Am. Chem. Soc.* **127**, 7140 (2005).
- [37] K.-T. Yong, Y. Sahoo, K. R. Choudhury, M. T. Swihart, J. R. Minter, and P. N. Prasad, *Nano Lett.* **6**, 709 (2006).
- [38] H. W. Jamie and C. Huaqiang, *Nanotechnology* **19**, 305605 (2008).
- [39] S. Acharya, U. K. Gautam, T. Sasaki, Y. Bando, Y. Golan, and K. Ariga, *J. Am. Chem. Soc.* **130**, 4594 (2008).
- [40] N. Pradhan, B. Katz, and S. Efrima, *J. Phys. Chem. B* **107**, 13843 (2003).
- [41] F. C. Whitmore and C. T. Simpson, *J. Am. Chem. Soc.* **55**, 3809 (1933).
- [42] D. L. Vincent and C. B. Purves, *Can. J. Chem.* **34**, 13021314 (1956).
- [43] P. Sawant, E. Kovalev, J. T. Klug, and S. Efrima, *Langmuir* **17**, 2913 (2001).
- [44] K. Polk, M. Nikl, E. Mihkov, and K. Nitsch, *J. Lumin.* **94-95**, 397 (2001).
- [45] C. Leiggenger and G. Calzaferri, *Chem.-Eur. J.* **11**, 7191 (2005).
- [46] C. B. Murray, D. J. Norris, and M. G. Bawendi, *J. Am. Chem. Soc.* **115**, 8706 (1993).
- [47] C. B. Murray, S. Sun, W. Gaschler, H. Doyle, T. A. Betley, and C. R. Kagan, *IBM J. Res. Dev.* **45**, 47 (2001).
- [48] W.-k. Koh, A. C. Bartnik, F. W. Wise, and C. B. Murray, *J. Am. Chem. Soc.* **132**, 3909 (2010).
- [49] J. C. de Mello, H. F. Wittmann, and R. H. Friend, *Adv. Mater.* **9**, 230 (1997).
- [50] I. Moreels and Z. Hens, *Small* **4**, 1866 (2008).
- [51] R. Koole, G. Allan, C. Delerue, A. Meijerink, D. Vanmaekelbergh, and A. Houtepen, *Small* **4**, 127 (2008).

- [52] H. Pascher, G. Bauer, and R. Grisar, *Phys. Rev. B* **38**, 3383 (1988).
- [53] I. Moreels, K. Lambert, D. De Muynck, F. Vanhaecke, D. Poelman, J. C. Martins, G. Allan, and Z. Hens, *Chem. Mater.* **19**, 6101 (2007).
- [54] B. L. Wehrenberg, C. Wang, and P. Guyot-Sionnest, *J. Phys. Chem. B* **106**, 10634 (2002).
- [55] J. Steckel, S. Coe-Sullivan, V. Bulovic, and M. Bawendi, *Adv. Mater.* **15**, 1862 (2003).
- [56] W. W. Yu, J. C. Falkner, B. S. Shih, and V. L. Colvin, *Chem. Mater.* **16**, 3318 (2004).
- [57] B. Cho, W. K. Peters, R. J. Hill, T. L. Courtney, and D. M. Jonas, *Nano Lett.* **10**, 2498 (2010).

CHAPTER 5
CHARGE TRANSFER IN QUANTUM DOTS

Charge transfer (CT) to and from nanocrystals is necessarily at the foundation of nanocrystal electrical device engineering. Injecting charges to interact with light, or extracting photoexcited charges to do work are two basic building blocks of optoelectronics. The basic mechanisms behind charge transfer are intuitively simple—charges will always move energetically downhill, through any available pathways. Understanding and eventually gaining control of these pathways is the goal of charge transfer research.

Marcus theory is the dominant model of charge transfer (CT) between molecular systems [1]. The intuitive picture behind the model is simple, and is shown in Fig. 5.1. The figure shows how the free energy of both the initial (left side

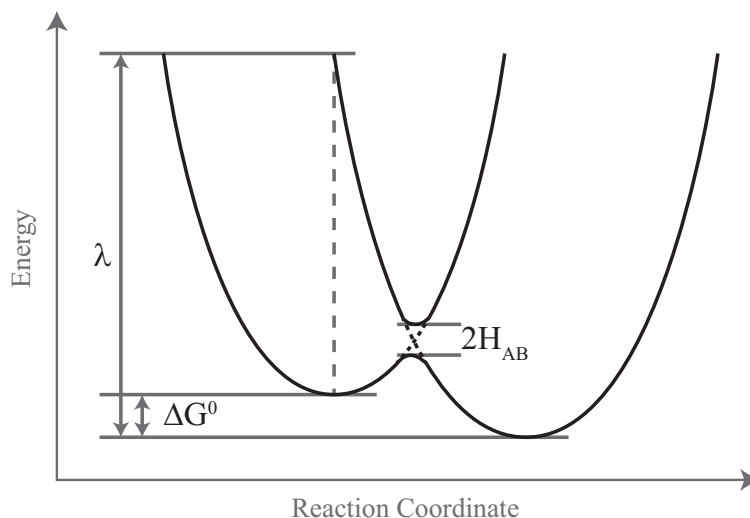


Figure 5.1: Energy diagram of Marcus theory.

parabola) and final (right side parabola) *system configurations* depend on the *reaction coordinate*. The two system configurations are simply having the charge on either the donor (left side) or acceptor (right side), and the reaction coordinate is

some arbitrary parametrization of the charge transfer. In general, there are many parameters associated with the changes in the system that occur during charge transfer, such as bond lengths and angles, and the reaction coordinate traces out a path in this parameter space which is followed during the charge transfer. Thus the two parabolas show the energy of the electron as it moves along the charge transfer path. Often the precise nature of the reaction coordinate path is never known, and we will not investigate it further here.

Due to energy conservation, the actual charge transfer event can only occur where the two parabolas cross. At this crossing point, the two parabolas are connected by a weak interaction, H_{AB} , between the donor and acceptor, coupling the energy levels, and allowing the charge to move from the left side minima to the right side one. But there is an energetic barrier to this, which is overcome by random thermal fluctuations. As a result, intuitively, charge transfer will only be efficient if the barrier is $\lesssim k_bT$. This energy scale also adds justification to the assumption of parabolic energy curves, since at this ~ 10 meV scale, parabolic approximations are often more than sufficient for molecular processes. Assuming a Boltzmann distributed density of states, the charge transfer rate is determined by the height of this barrier compared to k_bT , that is, $T^{-1} \sim \exp(-\Delta E_{\text{barrier}}/k_bT)$.

For example, suppose that the donor and acceptor are balls connected by a spring, and that the reaction coordinate is the length of the spring. Suppose also that charge transfer can only occur when the spring is one particular length, but that it takes energy to compress the spring to that point. Random thermal fluctuations cause the spring to vibrate, and there is a chance that when the spring is just the right size, the electron will instantly move from donor to acceptor, changing the configuration from initial to final, then allowing the system to relax

to the new ground state.

In terms of the variables defined in the figure, the rate of charge transfer within Marcus theory can be expressed as [2, 3]:

$$k_{\text{CT}} = \frac{1}{\tau_{\text{CT}}} = \frac{2\pi}{\hbar} |H_{\text{DA}}|^2 \frac{1}{\sqrt{4\pi\lambda k_b T}} \exp \left[-\frac{(\lambda + \Delta G^0)^2}{4\lambda k_b T} \right] \quad (5.1)$$

where H_{DA} is the electronic coupling between initial and final states, λ is the reorganization energy, ΔG^0 is the total Gibbs free energy change during the charge transfer, k_b is the Boltzmann constant, and T is the temperature. At a given temperature, there are three parameters that one might tune to control the transfer rate: ΔG^0 , λ , and H_{DA} .

The energy difference ΔG^0 is determined by the energy levels of the charge acceptor and donor. For our system, the simplest manner to change this parameter is to vary the size of the nanocrystal, exploiting their size-dependent energy levels. If their energy levels can be accurately measured, then one should be able to predict the size dependence of the charge transfer rate to an acceptor that remains unchanged for all NC sizes. Thus, our first task will be to accurately measure the energy levels of the nanocrystals.

The recombination energy λ is slightly more difficult to tune. This energy is all structural or other environmental energy changes that occur during the charge transfer, as a result of the charge moving from place to place. Many things fall into this category, including structural changes in either the donor or acceptor, vibrational motion caused by the transfer, and electrostatic energy differences between the initial and final configurations. The simplest, and most easily predictable, method to tune this parameter is by the latter source, electrostatic changes. Specifically, because the charge moves from one dielectric material to another during the charge transfer, the stored electrostatic energy changes from initial to final states.

One simple way to modify this is to change the dielectric constant of the medium, thereby either making the medium less or more easily polarized by the moving charge. Thus, we will attempt to modify λ by changing the solvent in which the transfer occurs.

Finally, the parameter H_{DA} can be tuned. This is the most difficult parameter to understand and to controllably modify. This is because it depends both on the potential that couples donor and acceptor, which is not known, and also on the precise atomic-scale wavefunction dependence of the initial and final states, which is beyond all but the most sophisticated calculations, and far beyond the scope here. Certain toy models can be proposed— the simplest being a finite potential barrier. This gives an exponential dependence to H_{DA} on the barrier thickness, which has been approximately verified experimentally in many cases. But there is no simple way to predict the height of the barrier from knowledge of its molecular makeup, and thus the predictive power of these types of models is very limited. Finding better ways to explore, predict, and control this parameter will remain a topic of future work, and for the purposes here H_{DA} will be assumed constant.

5.1 Absolute Energy Levels in Lead–Salt QDs

5.1.1 Introduction

Energy levels of nanocrystals (NCs) are typically calculated relative to an arbitrary zero point in energy, simply to avoid unnecessary complications in the calculation when they are not necessarily needed. Optical properties involving the absorption and emission of photons, and in general all effects that are independent of the

environment around the QD, only need these relative energy levels. But, when considering the effects of coupling between the QD and a neighboring system, the energy levels need to be placed on an absolute footing, relative to some global zero point, such as vacuum.

There are two strategies to calculating these absolute energy levels: bottom-up and top-down. Bottom-up approaches consider the NC as a large molecule, and through *ab initio* methods, can calculate the energy levels. But, this is a significant undertaking, is still an area of active research, and well beyond the scope here. A top-down approach to the problem considers the NC as a truncated piece of bulk semiconductor, and splits the calculation into two pieces: the absolute energy levels of the bulk semiconductor bands, and the shifts to those levels associated with the truncation to finite size. This produces a dramatic simplification, because the most complicated parts of the calculation are all placed together within an experimentally measurable and tabulated quantity— such as the electron affinity of the bulk semiconductor.

Truncating the semiconductor on the nanoscale produces two shifts to the bulk value. First, quantum confinement increases the kinetic energy of the charges, widening the energy gap. Second, the charges within the NC will create image charges within the dielectric medium surrounding the NC. In the simplest case of a flat interface, this interaction can be modeled with a single image charge. When the outer dielectric constant is smaller, the sign of the image charge makes the interaction repulsive, creating the so-called “dielectric confinement” effect, and giving both electrons and holes an additional positive energy shift. But even though the energy shift is positive for both types of carriers, the net effect is to additionally widen the energy gap. This is an initially confusing statement, and

deserves some clarification.

5.1.2 The Transport Energy Gap

To see why the energy gap is widened by dielectric confinement, we need to be more precise about what we mean by the “gap.” There are two primary energy gaps associated with nanocrystals: optical and transport. The optical gap is what is measured in optical spectra—the energy of an electron–hole pair within the nanocrystal. On the other hand, the transport gap is what is measured in electrical charging measurements, such as scanning tunneling spectroscopy (STS) or cyclic voltammetry (CV), where only a single electron or hole is involved. The tunneling gap can be written as the difference between the electron affinity (EA) and the ionization potential (IP), which are respectively, the energy needed to add and remove an electron from the system. In Fig. 5.2, the populations in an ideal two level quantum dot system are shown for each of these quantities. Note that the sign of the EA and IP are chosen so that they will be approximately equal to the LUMO and HOMO energy levels of the NC.

In order to determine the optical and transport energy gaps, the simplest method is to just add up the total energy for each of the above populations. Specifically, let’s define $E_{1,2}$ as the energies for occupied electrons in each of the two levels, $E_{self}^{e,h}$ as the dielectric confinement energy of a single electron or hole in a level, and E_{bind} as the Coulomb binding energy of a single electron and hole

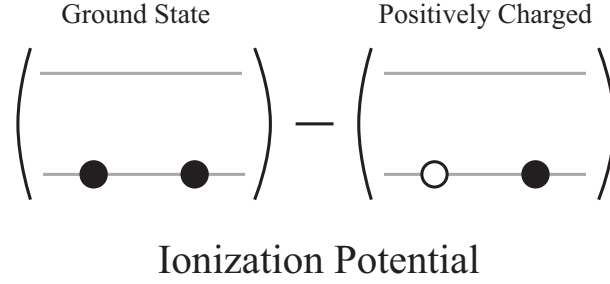
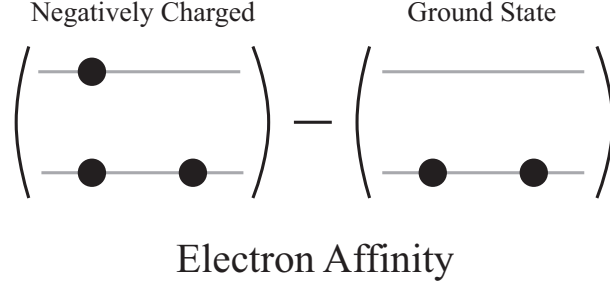
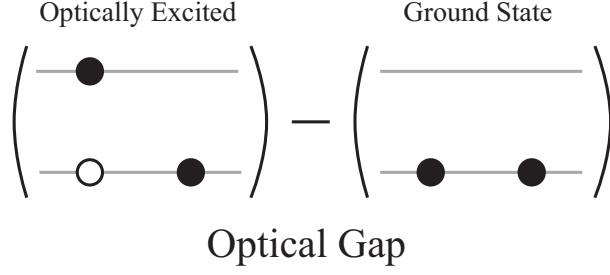


Figure 5.2: Diagram of the populations of an idealized two level quantum dot system.

together. Referring to Fig. 5.2, we find the following:

$$\begin{aligned}
 \Delta E_{\text{optical}} &= (E_1 + E_2 + E_{\text{self}}^e + E_{\text{self}}^h + E_{\text{bind}}) - (E_1 + E_1) \\
 &= E_2 - E_1 + E_{\text{self}}^e + E_{\text{self}}^h + E_{\text{bind}}
 \end{aligned} \tag{5.2}$$

$$\begin{aligned}
 \text{EA} &= (E_1 + E_1 + E_2 + E_{\text{self}}^e) - (E_1 + E_1) \\
 &= E_2 + E_{\text{self}}^e
 \end{aligned} \tag{5.3}$$

$$\begin{aligned}
 \text{IP} &= (E_1 + E_1) - (E_1 + E_{\text{self}}^h) \\
 &= E_1 - E_{\text{self}}^h
 \end{aligned} \tag{5.4}$$

$$\begin{aligned}
 \Delta E_{\text{transport}} &= \text{EA} - \text{IP} \\
 &= E_2 - E_1 + E_{\text{self}}^e + E_{\text{self}}^h
 \end{aligned} \tag{5.5}$$

One further simplification can be made to Eq. (5.2). Because the final three terms typically cancel in lead–salt nanocrystals, due to the similar electron and hole effective masses, $\Delta E_{\text{optical}} \approx E_2 - E_1$.

Importantly, the corrections from dielectric confinement $E_{self}^{e,h}$ increase the size of both the optical and transport gap in Eq. (5.2) and Eq. (5.5). Additionally, the EA is located above E_2 and the IP is located below E_1 , as shown in Fig. 5.3.

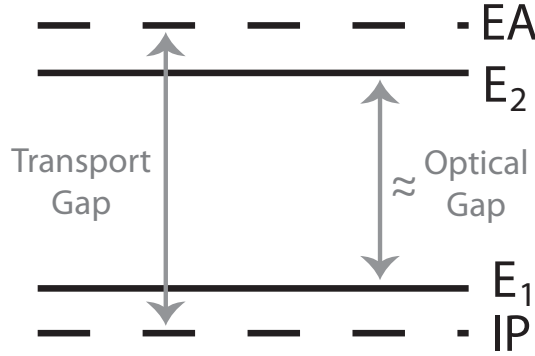


Figure 5.3: Comparison of the bare QD energy levels $E_{1,2}$ and the shifted electron affinity (EA) and ionization potential (IP) locations.

5.1.3 Calculating the Absolute Energy Levels

Brus [4] outlines an iterative procedure to include the effects of dielectric confinement in the calculation of absolute energy levels. Initially, wave functions and energy levels are calculated using a $\mathbf{k} \cdot \mathbf{p}$ model. Next, charge distributions are inferred from the wave functions and are used to determine the charge density in the NC. The electrostatic corrections to the energy, including dielectric effects are then calculated. Finally, an additive constant is included to the energy, so that as $R \rightarrow \infty$, the electron affinity approaches the experimentally measured value in bulk. Together, all of this produces the NC electron affinity. This EA is fed back

into the original $\mathbf{k} \cdot \mathbf{p}$ calculation as a finite potential well, and the procedure is then iterated until it becomes self-consistent.

For practical simplicity, we perform here only the first iteration of this procedure, assuming that additional shifts will be small enough to ignore. Energy levels are initially calculated using the $\mathbf{k} \cdot \mathbf{p}$ method of Kang & Wise [5] assuming an infinite potential barrier. The electrostatic energies $E_{self}^{e,h}$ are then calculated and added (subtracted) from the EA (IP), respectively. Brus [4] modeled the QD as a dielectric sphere inside of a dielectric medium with the formula:

$$E_{self}^{e,h} = \int d^3\mathbf{r}_{e,h} |\Psi_{e,h}|^2 \frac{e^2}{2R} \sum_{n=0}^{\infty} \frac{(\varepsilon - 1)(n + 1)}{\varepsilon_2(\varepsilon n + n + 1)} \left(\frac{r_{e,h}}{R}\right)^{2n} \quad (5.6)$$

where ε_2 is the dielectric constant of the nanocrystal, ε_1 is that of the medium, and $\varepsilon = \varepsilon_2/\varepsilon_1$. Because the $n = 0$ term of the sum does not depend on r_e or r_h , it is also independent of the nanocrystal wavefunction. This term also dominates the value of the sum, and can be used as a simple approximation.

$$E_{self}^{e,h} \approx \frac{e^2}{2R} \frac{(\varepsilon - 1)}{\varepsilon_2} = \left(\frac{1}{\varepsilon_1} - \frac{1}{\varepsilon_2}\right) \frac{e^2}{2R} \quad (5.7)$$

Unfortunately, it is still an open question over which dielectric constants to associate with a NC and use in this equation. More than just the question of whether optical or static constants are more appropriate, but even whether the use of dielectric constants measured in bulk semiconductors is even valid in nanostructures. In principle, measurements of the absolute energy levels like these should be able to determine these constants, but in practice the results are never clear enough to unequivocally make a choice.

For example, consider the following complication. The above dielectric sphere model neglects the effect of the ligands covering the surface of the nanocrystal. In order to include this effect, a slightly more complex model can be used, with an

additional thin dielectric shell between the sphere and the outside medium. We can still use Eq. (5.7), but we need to replace the medium dielectric constant ϵ_1 with an effective one ϵ_{eff} :

$$\epsilon_{\text{eff}} = \frac{(R + S)\epsilon_1\epsilon_3}{S\epsilon_1 + R\epsilon_3} \quad (5.8)$$

where the spherical shell has dielectric constant ϵ_3 and thickness S . Our quantum dots are typically covered with oleic acid ligands, with a molecular length around $S = 2$ nm, and a dielectric constant around 2-2.5 (static or optical). As a result, for small QDs, the effect of the ligand shell can dominate the value of the effective medium dielectric constant, as illustrated in Fig. 5.4. That is, for a solvent index that varies from $2 \rightarrow \infty$, the effective medium index only changes by a factor of 2. This effect is even more dramatic if a dielectric constant of 1 is used for the ligands, which is often used for monolayers of molecules, though again, the proper choice is not known.

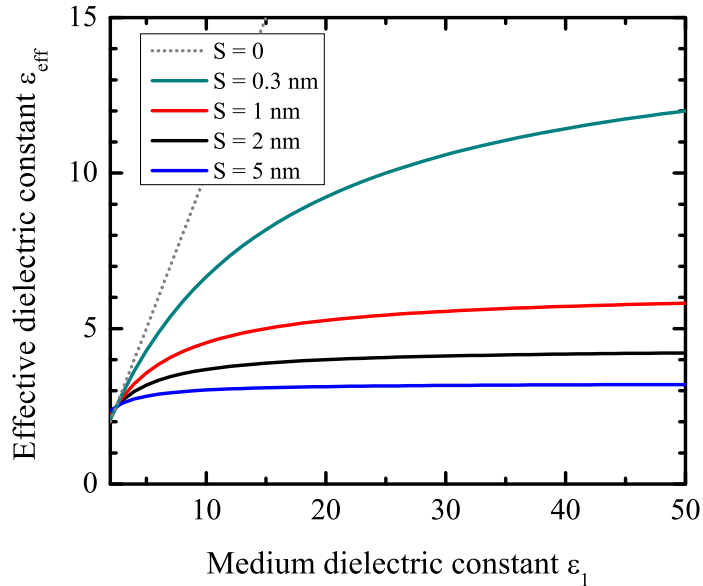


Figure 5.4: Effective shell+medium dielectric constant as a function of medium dielectric constant for a 3 nm NC, surrounded by an oleic acid shell of thickness S .

Because so little is known about the proper choice of dielectric constants, we

will assume that the bulk values are still applicable in nanostructures. This has the benefit of removing all dependence on the nanocrystal dielectric, because both the optical and static dielectric constants are so large in the lead salts as to have a negligible impact on Eq. (5.7). The medium dielectric constant will be left as a fitting parameter, with knowledge that the best fit value should be reasonable.

5.1.4 Comparison to Cyclic Voltammetry

Cyclic voltammetry [6] is a method of measuring energy levels relative to a known reference electrode, and it is performed in solution at room temperature, making it much simpler than methods which rely on high vacuum, such as photoelectron spectroscopy. Three electrodes are used: reference, working and counter. A nanocrystal film is deposited on the working electrode, and all three are immersed in an electrolyte solution. The potential of the working electrode is swept linearly between two set points, causing the nanocrystals to become charged whenever the potential is swept across one of their energy levels. This charging is seen as a peak in the I-V curve of the device. Using the known electrode potential of the reference electrode, absolute energy levels can be determined.

All cyclic voltammetry (CV) data were taken using an Epsilon (BAS) potentiostat. All measurements were carried out with the QDs capped with oleic acid dried into a film on a Pt working electrode, immersed in 0.1 M Bu₄NClO₄ in acetonitrile at a scan rate of 100 mV/s. The counter electrode is a platinum wire; the reference electrode is Ag/AgCl in saturated NaCl. Expected uncertainties in the results are ± 0.1 eV.

In Fig. 5.5, the measured CV energies are shown for PbS and PbSe NCs along

with the calculated values. The IP was not resolvable in the measurement due to nanocrystal decomposition upon charging, which is a common problem in CV measurements. The $R \rightarrow \infty$ bulk electron affinity was left as a fitting parameter for both PbS and PbSe, which has the effect of an overall additive constant to the calculated energies. The best fit values of -4.45 and -4.85 eV for PbS and PbSe, respectively, were close to the literature values of -4.6 and -4.7 eV [7, 8, 9]. And the best fit medium dielectric constant of 1.6 ± 1.0 was close to the optical dielectric constant of acetonitrile of 1.7.

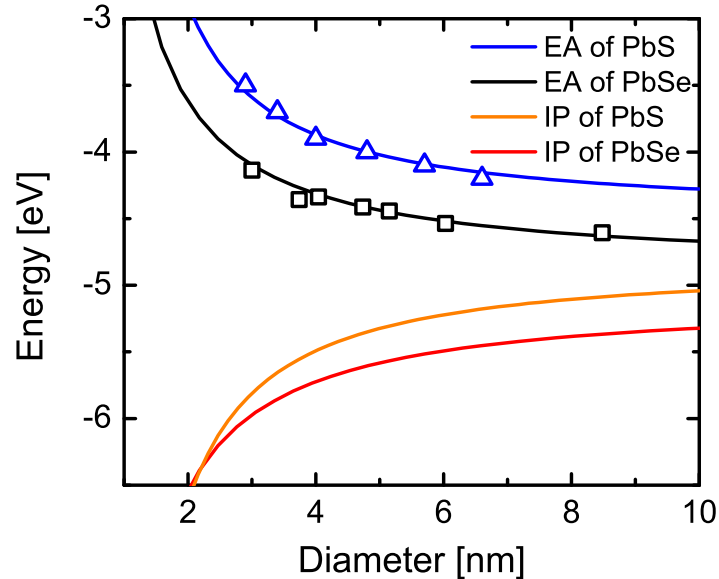


Figure 5.5: Calculated EA and IP of PbS (blue, orange lines) and PbSe (black, red lines) QDs, along with measured CV data (symbols).

Unfortunately, even though the uncertainty in the fit value for the dielectric constant is only moderate, $\epsilon = 1.6 \pm 1.0$, we still cannot state with any certainty what we learn about the dielectric constants. As stated previously, that could be interpreted as either evidence that the optical dielectric constant should be used, or as evidence that the static dielectric constants should be used, but in a model that includes the shielding effect of the ligands. Both would produce dielectric constants around 2.0. Further understanding requires further experiments— primarily,

if the IP had been resolved, then the transport gap would immediately give the value of the medium dielectric constant. Barring this, experiments in a variety of different solvents may produce measurable trends in the EA, though finding solvents compatible with cyclic voltammetry and also compatible with the NCs is very difficult.

5.2 Reorganization Energy

The total reorganization energy λ_{total} contains many different effects. As mentioned previously, the simplest piece to predict and modify involves the electrostatic energy stored in the system. As a result, we will write the total reorganization energy as a sum of two pieces, $\lambda_{\text{total}} = \lambda_0 + \lambda_e$, where λ_e is the electrostatic contribution and λ_0 is everything else. We will leave λ_0 undetermined and later use it as an adjustable parameter, though being mindful that it should not go far over the 100 meV range to be physically plausible.

To calculate λ_e , we choose a simple model for our physical system. Our model of a general donor–acceptor system will be of two dielectric spheres of radii R_1 and R_2 , separated by a center-to-center distance d . Initially the charge will be assumed to be evenly spread over the surface of sphere 1, and finally will be spread evenly over the surface of sphere 2. The spheres have dielectric constants ϵ_1 and ϵ_2 and are immersed in a dielectric medium with constant ϵ_3 . This model may seem like somewhat of a drastic oversimplification, but has been used successfully to model molecular charge transfer in the past [10, 11, 12], and is attractive for having both an analytic solution [13] and for having very simple analytic approximations that capture the important physics [2].

Of course, with this model we encounter the same problems as we did previously with the absolute energy level calculations, i.e. the dielectric constants are unknown. Importantly, though, since we are not performing cyclic voltammetry, there will be much more flexibility in the choice of solvent. By varying the solvent, we might be able to determine which dielectric constants are important— either static or optical. Notably, though, it already goes beyond the scope of this simple model to include the effect of the ligand layer surrounding the NC. If included, its effect would be to shield the energy levels of the nanocrystal from the effects of the medium. To partially take it into account, we will assume that the NC energy levels do not depend on the medium. On the other hand, the ligand layer will not greatly shield the charge acceptor from the effects of the medium, and in the important case where the acceptor is smaller than the nanocrystal donor, then the dominant contribution to λ_e will come from this acceptor alone. Because of all this, it is not unreasonable to neglect the ligands, while holding the NC energy levels constant.

The electrostatic reorganization energy can be written as [2, 14]

$$\lambda_e = \frac{1}{8\pi} \left(\frac{1}{\varepsilon_{3,\text{op}}} - \frac{1}{\varepsilon_{3,\text{st}}} \right) \int (D_i - D_f)^2 dv \quad (5.9)$$

where $\varepsilon_{3,\text{op}}$ and $\varepsilon_{3,\text{st}}$ are the optical and static dielectric constants of the medium, D_i and D_f are the initial and final electrostatic inductions of the system, and the integral is performed over the volume occupied by the outside medium. The stored electrostatic energy inside of the two spheres has been neglected, primarily because we assumed that the charge is spread into a uniform surface shell on each sphere, which acts to cancel out any internal energy. In order to get some physical insight to this model, it is useful to look at an approximation to it which is valid for large

separation d [2, 10].

$$\lambda_e \approx \left(\frac{1}{\varepsilon_{3,\text{op}}} - \frac{1}{\varepsilon_{3,\text{st}}} \right) \left(\frac{e^2}{2R_1} + \frac{e^2}{2R_2} - \frac{e^2}{d} \right) \quad (5.10)$$

From this equation, a few things become apparent. First, if either the donor or acceptor is much smaller than the other, then it will have the dominant effect on λ_e . In addition, the important dielectric quantity to consider is the combination $(1/\varepsilon_{3,\text{op}} - 1/\varepsilon_{3,\text{st}})$ of both the optical and static dielectric constants. Practically, if we vary this quantity, we should expect to see a uniform trend in the charge transfer rate.

5.3 Charge Transfer to Molecular Acceptors

In order to test the dependence of charge transfer rate on these quantities, we need an appropriate acceptor molecule. It must satisfy three demanding criteria: first, either electron or hole transfer from lead-salt NCs must be energetically favorable; second, it must be dispersible in various organic solvents; and finally, it must bind directly to the QD surface. Beginning with the third requirement, we chose the thiol (SH-) group as the binding functional group of the molecular acceptor, because it is known to bind strongly with the Pb ion of NCs [15, 16]. To satisfy the second condition, molecules with long alkyl chains are required. As a result, 10-dodecylanthracene-9-thiol (DAT) was synthesized [17], which combines a long alkyl chain with a central anthracene body, which is additionally attractive in application as an excellent molecular conductor [18]. The QD-DAT system is shown in Fig. 5.6.

To determine whether charge transfer is possible from QDs, cyclic voltammetry was used to determine the energy levels of DAT. The measured EA of DAT was

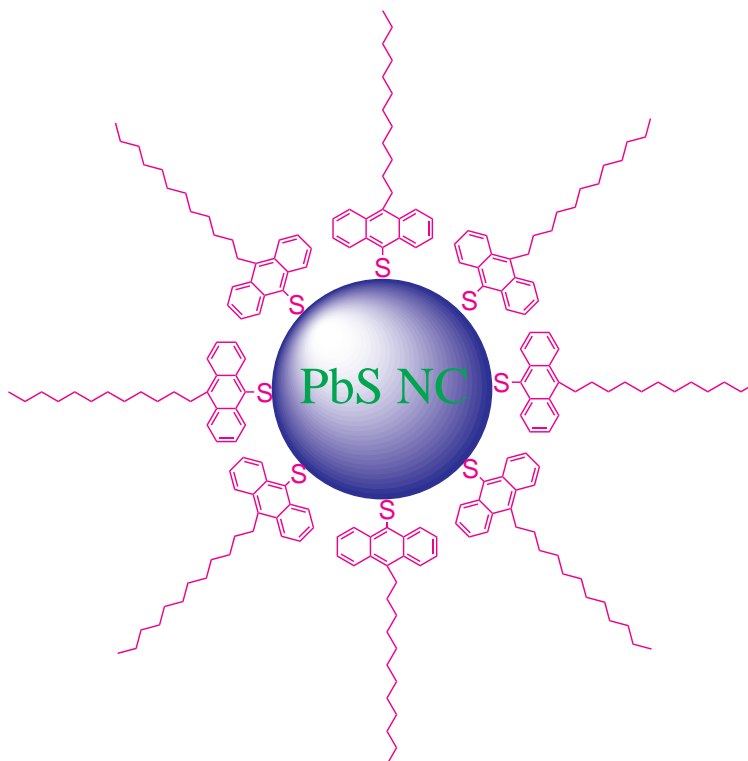


Figure 5.6: Schematic of a single spherical PbS QD donor bound to many DAT molecular acceptors.

at -3.94 eV *vs.* vacuum, which should allow electron transfer from PbS QDs for diameters less than a critical diameter $D_{\text{crit}} \approx 4.2$ nm. Because the optical energy gap of DAT is much larger than that of the QDs, we can deduce that the IP is sufficiently low to avoid hole transfer for all QD sizes. The energy level alignment is summarized in Fig. 5.7.

In order to verify this alignment, and specifically the existence of the critical diameter, the presence of charge transfer was probed using fluorescence measurements. If both the electron and hole remain in the QD, then it should fluoresce, while if charge transfer occurs, then the fluorescence will be quenched. In addition, monitoring the time dependence of the fluorescence can tell us the timescale of the charge transfer. In all following experiments, only the QD is optically excited,

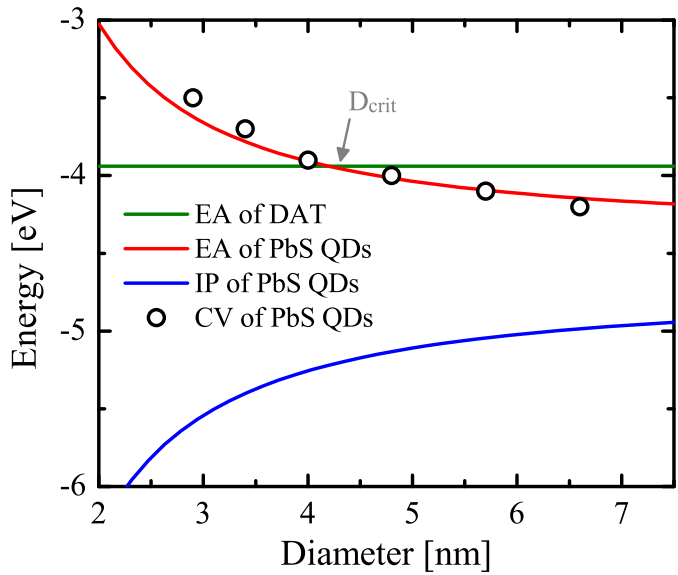


Figure 5.7: EA and IP of PbS QDs as a function of QD diameter and the EA of DAT molecules (flat line). Below diameter D_{crit} , electron transfer from PbS to DAT should be allowed.

followed by either time-integrated fluorescence or time-correlated single photon counting (TCSPC) measurements. Sample preparation was performed by mixing DAT molecules with PbS QDs in organic solvents with a molar ratio of DAT to QDs in excess of 10000:1. Thus, the binding of the DAT to the QDs should be saturated (every available bond site is occupied) in all cases, regardless of the details of the particular solvent used.

As a simple test of the presence of the critical diameter D_{crit} , we tested QD sizes above and below with diameters 5.6 and 3.0 nm. As expected, the 5.6 nm QDs show no sign of charge transfer, while the 3.0 nm QDs are quenched dramatically (over 99%) in the presence of DAT. The time-integrated data for both sizes is shown in Fig. 5.8.

Now that we had evidence of the presence of charge transfer, we turned to transient fluorescence to provide a quantitative measure of the CT rate. We varied

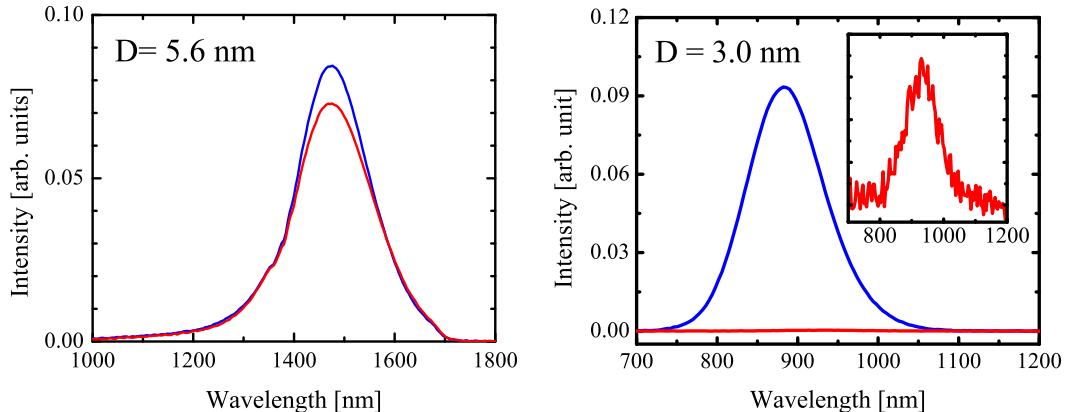


Figure 5.8: Time-integrated fluorescence measurements of PbS QDs bound to DAT molecules. Blue lines are bare QDs without DAT; red lines are after binding to DAT. Inset shows detail of the quenched emission. The QDs smaller than the critical diameter show dramatic quenching in the presence of the DAT electron acceptor.

two aspects of our system: the QD size and the solvent. As mentioned, these were chosen to independently vary the parameters ΔG^0 and λ , respectively, in Marcus theory. We tested three QD sizes below the critical diameter: 3.0, 3.5 and 3.7 nm. The inset of Fig. 5.9a shows that the fluorescence of 3.0 nm PbS QDs decays with a time constant of 2.7 μs before exposure to DAT. After coupling to DAT, the decay times decrease to the ≈ 10 ns range (Fig. 5.9a). The organic solvent was varied over as wide a range of dielectric constants as was possible, with the constraint that the QDs remain soluble. The fluorescence transients for six solvents were measured, and the representative cases of toluene, chloroform, and dichloromethane are shown in Fig. 5.9b.

Because the transfer times were not single exponential, some average lifetime needs to be calculated in order for a quantitative analysis. We used an intensity weighted average lifetime [19, 20], $\langle t \rangle = \sum_i a_i \tau_i^2 / a_i \tau_i$, after fitting with a multi-component exponential function. In general, the effect of the radiative rate should be subtracted off as $k_{\text{CT}} = \tau_{\text{QD+DAT}}^{-1} - \tau_{\text{QD}}^{-1}$, but because $\tau_{\text{QD+DAT}} \ll \tau_{\text{QD}}$, this is

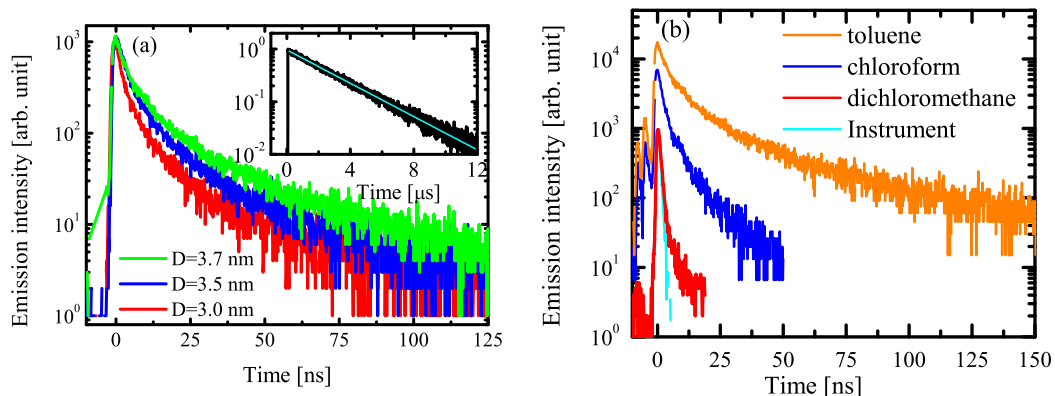


Figure 5.9: Measured fluorescence decay times of PbS QDs bound to DAT molecules. In (a) the dependence on QD size is shown, with an unbound 3.0 nm QD shown in the inset. In (b) the dependence on solvent is shown.

only a negligible change.

Following our expectations from Eq. (5.10), we plotted the average lifetimes versus that combination of dielectric constants, but could not see a uniform trend in the data (Fig. 5.10a). Similarly, plotting versus only the optical dielectric constant of the media also produces no noticeable trend (Fig. 5.10b). On the other hand, plotting versus only the static dielectric constant produces a clear trend in the data (Fig. 5.11a). Guided by this experimental observation, we propose to model the reorganization energy with only static dielectric effects. That is, we simply calculate the difference in electrostatic energy between initial and final configurations. Possible reasons for this assumption are discussed later in this chapter.

Specifically, using the same model of two dielectric spheres with charge spread evenly over their surfaces, we set the radius of the DAT molecule $R_2 = 1.0$ nm and the donor-acceptor separation $d = R_1 + R_2$, so that donor and acceptor are touching, as a reasonable approximation. We left the parameter λ_0 as a free parameter, and show the predicted transfer rates for various choices of this value

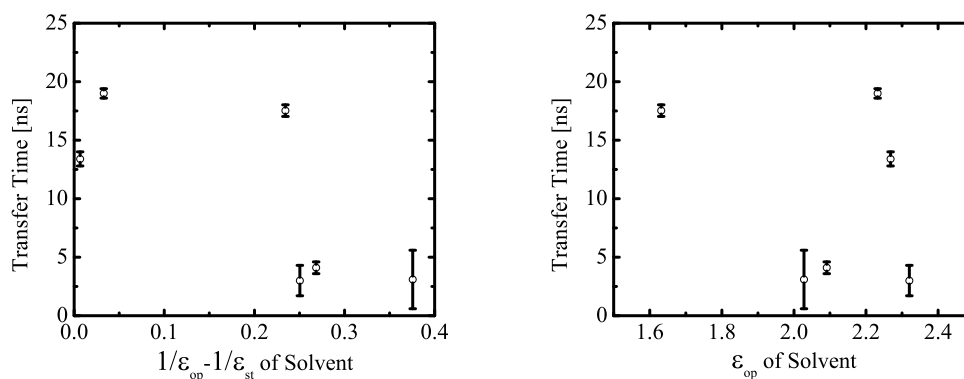


Figure 5.10: Dependence of charge transfer time on various combinations of the solvent dielectric constants. In (a) the standard combination of optical and static constants is chosen. In (b) only the optical constant is used. In neither case is a uniform trend observed with these choices.

in Figure 5.11. For all graphs, the value of unknown multiplicative constant H_{DA} was chosen to set the overall scale of the transfer correctly, but held constant for all QD sizes and solvents.

This model produces a good fit to the variation of CT time with dielectric constant (Fig. 5.11a), and a reasonable fit to the trend with NC size (Fig. 5.11b). The best fit to the measured trend with QD size is obtained with $\lambda_0 = 0$, although this causes the transfer time to increase by many orders of magnitude as the dielectric constant approaches that of water (inset of Fig. 5.11a). With slightly larger values of λ_0 , the transfer time will either remain roughly constant or decrease further for large values of the dielectric constant. Unfortunately this trend cannot be addressed directly with the DAT molecules; to our knowledge, there are no viable organic solvents with static dielectric constants that large. Considering the simplicity and approximations of the theoretical approach, the agreement with experiment is good. We tentatively attribute the importance of the static dielectric constant to the long time scales involved in CT processes studied here, relative to the time scale of molecular motion. The longitudinal relaxation time is less than

10 ps for all the solvents used in this work [21, 22, 23, 24, 25, 26, 27]. The slow time scale of the transfer relative to orientational relaxation allows the molecules to be in constant equilibrium, so the reorganization is purely electrostatic in nature. In general, for faster charge transfer, the solvent dipoles are not expected to be in instantaneous electrostatic equilibrium with the reactants during CT, and thus a more complex non-equilibrium calculation is required, resulting in the combination of dielectric constants in Eq. (5.9).

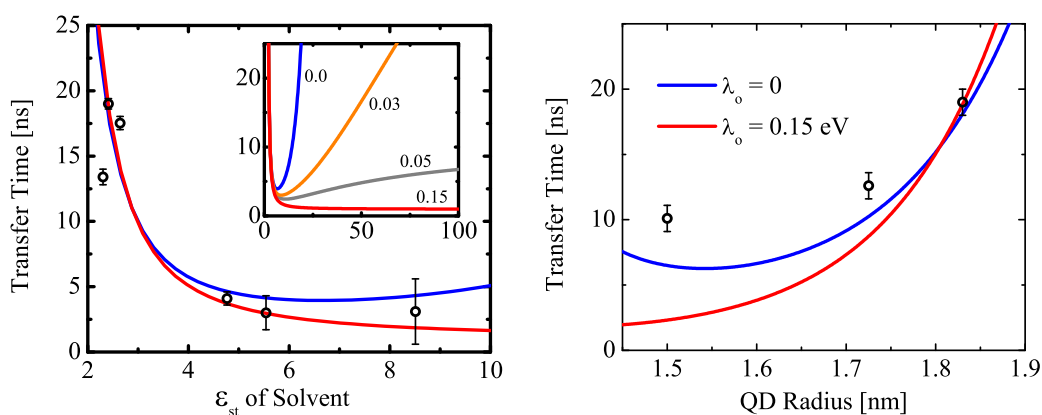


Figure 5.11: Charge transfer time dependence on solvent static dielectric constant (a) and QD size (b). Experimentally measured values (symbols) are compared to calculated trends (colored lines) for different values of the unknown parameter λ_0 . The inset of (a) shows the trends for $\lambda_0 = 0, 0.03, 0.05, 0.15$ eV for even larger static dielectric constants than those measured.

Finally, it is important to look back at our assumption that the QD energy levels do not change with solvent static dielectric constant. In the worst case, if there were no shielding from the ligands and the full effect of the medium is felt on the QD energy levels, the expected trend in transfer time would be opposite of that observed here. As the static dielectric constant increases, the dielectric confinement energy decreases $\propto 1/\epsilon$. This would decrease the energy gap ΔG^0 , causing the charge transfer time to be longer. But in contrast, we see shorter transfer times for larger dielectric constants. So, even if this effect were included more accurately it could not produce the observed trends alone.

5.4 Conclusion

In summary, we have measured the electron affinity of PbS and PbSe QDs as a function of size. The data was fit to a model that incorporated dielectric effects, with a best fit value of the effective medium dielectric constant of 1.6 ± 1 . This value is consistent with either the optical dielectric constant of acetonitrile of 1.7, or even with the static value of 37.5 after being screened by a low dielectric constant ligand layer. The location of these energy levels is verified by binding PbS QDs to DAT molecules and seeing fluorescence quenching below, but not above, a critical QD diameter D_{crit} .

Second, we find that the rate of charge transfer from PbS NCs to DAT molecules increases dramatically with solvent static dielectric constant. This trend is accounted for by a modified Marcus theory that incorporates only static dielectric effects. Within this model, the assumption was made that the QD energy levels are not affected by the change of solvent, which is only possible if they are shielded by a small dielectric constant ligand layer.

The consistent picture appears to be that the static dielectric constants of all quantities should be used, possibly because of the long timescale of all reactions involved with charge transfer. Though due to the number of assumptions made in our models, we cannot completely rule out other options. The most additional progress can be made by somehow measuring the EA and IP simultaneously, either by refining the CV measurement, or by using some other method. Photoelectron spectroscopy is designed to measure the IP directly, and even though it would be useful to have this information, because the experiment is performed in high vacuum after ligand modification, the IP measured there may not be the same as what would be measured in solution with oleic acid ligands. Scanning tunneling

spectroscopy offers the ability to directly measure both EA and IP directly, but has the unfortunate problem that the raw data has both an unknown additive and a multiplicative constant applied, with extensive literature devoted to analyzing the data. In short, there is no obvious single experiment that would definitively answer the questions raised here, and more likely, a consistent picture will have to be made to explain many individual experiments over time.

BIBLIOGRAPHY

- [1] R. A. Marcus, *Annu. Rev. Phys. Chem.* **15**, 155 (1964).
- [2] R. A. Marcus, *J. Chem. Phys.* **24**, 966 (1956).
- [3] R. A. Marcus, *J. Chem. Phys.* **24**, 979 (1956).
- [4] L. E. Brus, *J. Chem. Phys.* **80**, 4403 (1984).
- [5] I. Kang and F. W. Wise, *J. Opt. Soc. Am. B* **14**, 1632 (1997).
- [6] J. Heinze, *Angew. Chem. Int. Ed.* **23**, 831 (1984).
- [7] R. A. Knapp, *Phys. Rev.* **132**, 1891 (1963).
- [8] G. Guizzetti, F. Filippini, E. Reguzzoni, and G. Samoggia, *Phys. Status Solidi A* **6**, 605 (1971).
- [9] S.-H. Wei and A. Zunger, *Phys. Rev. B* **55**, 13605 (1997).
- [10] E. D. German and Y. I. Kharkats, *Chem. Phys. Lett.* **246**, 427 (1995).
- [11] R. A. Marcus, *J. Chem. Phys.* **43**, 679 (1965).
- [12] M. J. Powers and T. J. Meyer, *J. Am. Chem. Soc.* **100**, 4393 (1978).
- [13] Y. Nakajima and T. Sato, *J. Electrostat.* **45**, 213 (1999).
- [14] Y. I. Kharkats, *Sov. Electrochem.* **12**, 566 (1976).
- [15] V. S. Gurin, K. N. Kasparov, and E. A. Tyavlovskaya, *Colloids Surf., A* **139**, 1 (1998).
- [16] B. R. Hyun, H. Y. Chen, D. A. Rey, F. W. Wise, and C. A. Batt, *J. Phys. Chem. B* **111**, 5726 (2007).
- [17] B.-R. Hyun, A. C. Bartnik, J.-K. Lee, H. Imoto, L. Sun, J. J. Choi, Y. Chujo, T. Hanrath, C. K. Ober, and F. W. Wise, *Nano Lett.* **10**, 318 (2010), doi: 10.1021/nl903623n.

- [18] J. Oliver H. LeBlanc, *J Chem. Phys.* **33**, 626 (1960).
- [19] J. R. Lakowicz, *Principles of fluorescence spectroscopy* (Springer, New York, NY, 2006).
- [20] D. R. James, Y. S. Liu, P. Demayo, and W. R. Ware, *Chem. Phys. Lett.* **120**, 460 (1985).
- [21] C. P. Smyth, *Ann. Rev. Phys. Chem.* **17**, 433 (1966).
- [22] J. M. Halbout and C. L. Tang, *J. Phys.* **44**, 135 (1983).
- [23] T. Bischofberger and Y. R. Shen, *Opt. Lett.* **4**, 40 (1979).
- [24] A. A. Antony and C. P. Smyth, *J. Am. Chem. Soc.* **86**, 152 (2002), doi: 10.1021/ja01056a008.
- [25] G. Vicq and G. Delbos, *J. Mol. Liq.* **56**, 287 (1993).
- [26] M. W. Evans and M. Ferrario, *Adv. Mol. Relax. Interact. Processes* **23**, 113 (1982).
- [27] J. Barthel, K. Bachhuber, R. Buchner, and H. Hetzenauer, *Chem. Phys. Lett.* **165**, 369 (1990).

CHAPTER 6

FUTURE DIRECTIONS

Charge transfer research has perhaps the most broad opportunity for further research, and also some of the strongest potential for application in devices. I feel that this dissertation shows evidence that Marcus Theory remains relevant in nanocrystals, but much more further work is needed. For example, the ionization potential (IP) remains unknown, preventing further work involving hole transfer. Either the IP needs to be directly measured, perhaps with ultraviolet photoelectron spectroscopy (UPS) or with refinements to the CV measurements performed here, or it may be possible to infer the IP with more accurate knowledge of the effective medium dielectric constant. For example, varying the solvent used in CV across a broad range of known static and optical dielectric constants may provide enough of a trend to match with an effective dielectric model. But finding solvents that span a large range that are also compatible with CV will be difficult. And regardless it may be difficult to measure such a trend on top of the fundamental 0.1 eV uncertainty in CV.

Perhaps more importantly, the parameter H_{DA} of Marcus Theory remains uninvestigated. This parameter determines the overall scale of the transfer rate, and could vary dramatically depending on the molecular makeup of the acceptor and any linker molecules connecting it to the donor. To predict this parameter, detailed atomistic calculations are needed. Although it may be possible to directly model photoinduced charge transfer with either time dependent density functional theory (TDDFT) or other dynamical models, because of the gigantic 10-100 ns timescales measured here and elsewhere [1], compared to the 10-100 ps state-of-art simulations [2], this method may be hopelessly intractable at present. The best

approach may be to calculate the initial and final wavefunctions using an artificial constraint on the location of the charge [3] and then calculate directly the matrix element H_{DA} using these wavefunctions. Of course, using DFT to calculate wavefunctions is always difficult to justify, as it is not a wavefunction-based method. Experimentally varying this parameter, on the other hand, is as simple as changing the charge acceptor. Or, if the system has the form donor-linker-acceptor, then modifying the linker might change H_{DA} independently of the other parameters, allowing a more controlled experiment.

Similarly, the PbSe nanorods synthesized in this dissertation allow almost as large a terrain for future exploration, because very little is still known about them. Topics including hot carrier relaxation rates, multiple exciton generation efficiencies, vibrational modes, charge transfer rates, dephasing times, temperature dependence of the absorption and emission, and many others, all need to be reevaluated in light of the electronic structure calculations presented here. If the rods can be persuaded to align on a substrate, polarization studies of the absorption and emission may shed additional light on the fine structure of the electronic states, which is not measurable in isotropically-shaped spherical QDs. One especially simple example, that of the far-IR vibrational absorption spectrum, is particularly sensitive to the aspect ratio and dielectric constant of the nanorod— and if the aspect ratio is known from TEM, then this may be the first method able to directly measure the dielectric constant of a nanocrystal.

On the other hand, even though the core-shell QDs have a novel core-shell electronic structure, which more-or-less causes them to act like a single material QD, this also somewhat limits their further appeal. Because the significant extra effort required to synthesize them over true core QDs is not offset by dramatically

improved properties, it is difficult to justify using them in application. Further work should be done on larger sized core-shell QDs, which reach the size regime where the electron and hole may separate into different layers, because this will become very sensitive to the bulk band edge alignment of the two semiconductors, which is currently unknown, and is a very important parameter in charge transfer research.

BIBLIOGRAPHY

- [1] B.-R. Hyun, Y.-W. Zhong, A. C. Bartnik, L. Sun, H. D. Abruna, F. W. Wise, J. D. Goodreau, J. R. Matthews, T. M. Leslie, and N. F. Borrelli, *ACS Nano* **2**, 2206 (2008).
- [2] S. V. Kilina, C. F. Craig, D. S. Kilin, and O. V. Prezhdo, *J. Phys. Chem. C* **111**, 4871 (2007).
- [3] Q. Wu and T. Van Voorhis, *Phys. Rev. A* **72**, 024502 (2005).

APPENDIX A
ADDITIONAL SYNTHESSES

A.1 CdSe Quantum Dots

The synthesis of cadmium-based nanoparticles [1] is at least as well established as that of the lead-salts, but many more subtleties are encountered, due in part to the higher temperatures involved and the reactivity of the chemicals used. In addition, many different methods are encountered in the literature, with small (yet still very important) modifications. The purpose here is to present a method that is somewhat more robust than those in the literature, though sacrificing slightly the tunability of the absorption peak. This method is adopted from private communication with the Robertson group in the department of Material Science and Engineering at Cornell University.

Table A.1: Chemicals needed for a typical synthesis of CdSe QDs.

Name, (purity)	Abbr.	Amount	(g/mol)	(g/mL)
Cadmium Oxide	CdO	1 mmol	128.41	8.15
Selenium Powder (100 mesh, 99.5%)	Se	see text	78.96	4.81
Trioctylphosphine	TOP	see text	370.64	0.831
Oleic Acid (99%)	OA	4 mmol	282.46	0.895
1-Octadecene, (90%)	ODE	20-25 mL	252.48	0.789
Oleylamine (70%)	OLA	3.5 mL	267.49	0.813

The chemicals needed for the synthesis are shown in Table A.1. Importantly, the oleic acid purity is now 99%, though 90% may also be possible and is untested. The highest currently available purity of oleylamine is 70%, and it is recommended to buy it from Sigma Aldrich, as other companies may have other impurities which can lead to many problems.

The previous day, a 12% by mass solution of selenium in TOP is created within

a glove box, and is left overnight under moderate stirring in order to thoroughly dissolve the selenium. On the day of the synthesis, the first step is to produce Cd-oleate. First, add 1 mmol of CdO to a 50 mL flask. Seal the flask, vacuum, and fill with N₂ (repeat 3x). Weigh 4 mmol of oleic acid, and add to flask with a syringe that has been thoroughly flushed with nitrogen. Optionally, to make the injection of the viscous oleic acid easier, add ~2-3 mL of less viscous ODE. Heat the solution to 180 °C, and wait until the the solution turns clear. Cool the solution back down to 110 °C. Now, vacuum the flask for 2-3 minutes and fill with N₂. Repeat this ~3-5 times until the droplets of re-condensed water disappear from the top of the flask. If you cannot see any water, do this 5x anyway. Now, add 7.5 mmol of oleylamine, followed by 20 mL of ODE, using a nitrogen flushed syringe in each case. Heat the solution to 260 °C, and allow it to thoroughly stabilize temperature.

When it is stabile, add 1.316g of TOP-Se solution to the flask, and allow 5 minutes of reaction time at 260 °C. Size tuning with temperature and synthesis duration are untested in our lab with this method. Cool to room temperature in a water bath, leaving the solution in the same flask, under nitrogen flow, during the cooling process.

For this process, it might be necessary to use a thermometer sleeve, likely requiring a special order from a glassware maker, to encase the temperature probe, protecting it from chemical reactions at the high reaction temperature.

A.2 Hexadecylxanthate ligands

The synthesis of lead hexadecylxanthate is a combination of methods in Refs. [2, 3, 4, 5]. The chemicals needed for a typical synthesis are shown in Table A.2.

Table A.2: Chemicals needed for a synthesis of lead hexadecylxanthate.

Name	Abbr.	Amount
Hexadecanol (Cetyl Alcohol)	HDOH	9.7 g
Potassium Hydroxide	KOH	2.24 g
Carbon Disulfide	CS ₂	3.5 mL
Toluene	Tol	25 mL
Hexane	Hex	100 mL

The first step is to create potassium hexadecylxanthate (K-HDX). First, combine hexadecanol and KOH in a large 3-neck flask, positioned on a heating mantle. Insert a mechanical stirrer into flask, using stabilizer attachment, through the center neck. This is *not* a magnetic stir bar— it is a device similar to a mixer used when cooking masked potatoes, for example, and is useful for solutions so viscous that a magnetic stir bar is useless. When stirring, there shouldn't be any noise or "clinking" of the stir bar against glass. If so, adjust position of flask until it goes away, to avoid breaking any of the glass. Keep the stir speed low during the adjustment.

Air-free techniques are not needed, but septums are still nice to prevent splashing, so if desired put two on the remaining two necks. Somehow arrange the temperature probe inside the flask, entering from one of the two side necks, such that it is as close to the stirrer as possible without hitting it. The idea is to make sure the liquid, when stirring, will touch the probe. I typically would duct tape the probe to the top of the mechanical stirrer to be absolutely sure that it wouldn't hit the rapidly spinning blade of the stirrer. Raise the temperature to 150 °C, and begin stirring when the contents become liquid (around 40-50 °C.) Contents will

begin to turn yellow or orange at 100 °C, and will get increasingly darker as you get closer to 150 °C.

At 150C, reduce the set point of the temperature to 100 °C and add the 25 mL of toluene. There is a small amount of boiling, but the temperature goes quickly to 100 °C. When the temperature is stable at 100 °C, remove the heating mantle, and then slowly syringe in the CS₂. By “slow” I mean somewhere in between “dropwise” and “as fast as possible.” It is not very sensitive to this. During this, the temperature drops to 85-90 °C, and a yellow-orangish precipitate forms. Temperature is allowed to reduce to room temperature, while vigorous stirring is maintained. Continue stirring for 1 hour. After 1 hour, add the 100mL Hexane, and then stir for 2 more hours.

In order to purify the K-HDX, use a large vacuum flask with filter attachment, and filter out residual liquid from the synthesis. I used a small portable pump to pump the liquid out, and in general you do not want to use too strong of a pump or the entire filter assembly will be sucked into the flask. When dry, add hexane to wash the precipitate, and place on the vacuum filter assembly and filter it out. Repeat 3 times. When dry, place entire filter assembly in the vacuum chamber for the glove box and vacuum for 5 minutes. When complete, in a similar manner as above, wash with DI water, filter, and vacuum dry. Finally, wash again with hexane, filter, and vacuum dry. You should be left with a light yellowish to white powder. Grind up the powder with a mortar and pestle and place in storage in a desiccator.

To create Pb-HDX from K-HDX, first add 178 mg of K-HDX to 10mL of methanol in a 20mL glass vial. Vortex, sonicate, and stir solution until well dissolved. Separately, add 100 mg of lead nitrate to 3.0 mL of water. While methanol

solution is stirring, add the water solution to it dropwise and observe the immediate formation and precipitation of Pb-HDX. Ideally, keep adding drops until you no longer observe the formation of the Pb-HDX. It is difficult to tell when precipitation stops, and it is safer to have too much than not enough.

Set up a filter flask, filter funnel, and filter paper. Rinse filter paper briefly with methanol or water and allow to drip through filter. Pour solution into filter setup, let drip through until all the liquid has gone through. Alternatively, apply a weak vacuum to help suck it down. Add 20mL of a 1:3 water:methanol mixture and allow to pass through the filter. Repeat rinsing at least two more times. Allow to dry at room temperature. For faster drying, place in room temperature vacuum chamber for 1 hour. If the final powder turns brownish to black, or even has a hint of those colors, then assume that the Pb-HDX has begun to decompose, and discard. Next time, try rinsing more times or drying somehow faster.

BIBLIOGRAPHY

- [1] C. B. Murray, D. J. Norris, and M. G. Bawendi, *J. Am. Chem. Soc.* **115**, 8706 (1993).
- [2] N. Pradhan, B. Katz, and S. Efrima, *J. Phys. Chem. B* **107**, 13843 (2003).
- [3] F. C. Whitmore and C. T. Simpson, *J. Am. Chem. Soc.* **55**, 3809 (1933).
- [4] D. L. Vincent and C. B. Purves, *Can. J. Chem.* **34**, 13021314 (1956).
- [5] P. Sawant, E. Kovalev, J. T. Klug, and S. Efrima, *Langmuir* **17**, 2913 (2001).

APPENDIX B
PBSE NANORODS

B.1 Effect of anisotropy on the nanowire energy spectra

The cylindrically symmetric Hamiltonian in Eq. (4.4) can be derived from the full Hamiltonian in Eq. (4.3) by transformation to the new coordinate system connected with NW direction. The full Hamiltonian is defined with respect to a crystallographic direction of the Brillouin zone, where the z -axis is pointed towards one of the L-points, and we will call this coordinate system the primed system, $\{x', y', z'\}$. We need to express Eq. (4.3) in the new coordinate system where the z -axis is directed along the rod axis, called the unprimed system, $\{x, y, z\}$. To do this, we use a coordinate rotation, and define the x -axis such that the rotation occurs in the x - z plane. In the rotation, vector quantities, such as $\hat{\mathbf{p}}$ or $\hat{\boldsymbol{\sigma}}$ are transformed using the rotation matrix, $\hat{\mathbf{p}}' = R(\theta)\hat{\mathbf{p}}$, with R defined as

$$R(\theta) = \begin{pmatrix} \cos \theta & 0 & -\sin \theta \\ 0 & 1 & 0 \\ \sin \theta & 0 & \cos \theta \end{pmatrix}. \quad (\text{B.1})$$

This transformation expresses the squared momenta in Eq. (4.3) as:

$$\hat{p}'_x{}^2 = \cos^2 \theta \hat{p}_x^2 - \sin 2\theta \hat{p}_x \hat{p}_z + \sin^2 \theta \hat{p}_z^2 \quad (\text{B.2})$$

$$\hat{p}'_z{}^2 = \sin^2 \theta \hat{p}_x^2 + \sin 2\theta \hat{p}_x \hat{p}_z + \cos^2 \theta \hat{p}_z^2. \quad (\text{B.3})$$

and the diagonal and off-diagonal elements of the matrix of Hamiltonian in Eq. (4.3) in new coordinate system as:

$$\begin{aligned} \frac{1}{m_t}(\hat{p}_x'^2 + \hat{p}_y'^2) + \frac{1}{m_l}\hat{p}_z'^2 &= \left(\frac{\cos^2 \theta}{m_t} + \frac{\sin^2 \theta}{m_l}\right)\hat{p}_x^2 + \frac{1}{m_t}\hat{p}_y^2 + \\ &+ \left(\frac{\sin^2 \theta}{m_t} + \frac{\cos^2 \theta}{m_l}\right)\hat{p}_z^2 + \\ &+ \sin 2\theta \left(\frac{1}{m_l} - \frac{1}{m_t}\right)\hat{p}_x\hat{p}_z \end{aligned} \quad (\text{B.4})$$

$$\begin{aligned} P_t\sigma'_x\hat{p}'_x + P_t\sigma'_y\hat{p}'_y + P_l\sigma'_z\hat{p}'_z &= (P_t\cos^2\theta + P_l\sin^2\theta)\sigma_x\hat{p}_x + P_t\sigma_y\hat{p}_y + \\ &+ (P_t\sin^2\theta + P_l\cos^2\theta)\sigma_z\hat{p}_z + \\ &+ \frac{1}{2}\sin 2\theta(P_l - P_t)(\sigma_z\hat{p}_x + \sigma_x\hat{p}_z) \end{aligned} \quad (\text{B.5})$$

Notice that neither elements are cylindrically symmetric in the new coordinates. To enforce this symmetry, we rewrite these expressions in a form that separates a cylindrically symmetrical part, formally: $a\hat{O}_x + b\hat{O}_y = (1/2)(a + b)(\hat{O}_x + \hat{O}_y) + (1/2)(a - b)(\hat{O}_x - \hat{O}_y)$. The first term, which has cylindrical symmetry, is used in the zero-th order Hamiltonian, and the second term creates the asymmetric perturbation. This procedure produces the Hamiltonian in Eq. (4.4), along with the perturbation matrix

$$\hat{H}_{an} = \begin{pmatrix} \frac{1}{2}\hat{U}\left(\frac{1}{m_l^-} - \frac{1}{m_t^-}\right) \times & \frac{1}{2m}(P_l - P_t)\{\sin^2\theta(\hat{\sigma}_x\hat{p}_x - \hat{\sigma}_y\hat{p}_y) + \\ \times \left(\frac{1}{2}\sin^2\theta(\hat{p}_x^2 - \hat{p}_y^2) + \sin 2\theta\hat{p}_x\hat{p}_z\right) & + \sin 2\theta(\hat{\sigma}_z\hat{p}_x + \hat{\sigma}_x\hat{p}_z)\} \\ \frac{1}{2m}(P_l - P_t)\{\sin^2\theta(\hat{\sigma}_x\hat{p}_x - \hat{\sigma}_y\hat{p}_y) + & -\frac{1}{2}\hat{U}\left(\frac{1}{m_l^+} - \frac{1}{m_t^+}\right) \times \\ + \sin 2\theta(\hat{\sigma}_z\hat{p}_x + \hat{\sigma}_x\hat{p}_z)\} & \times \left(\frac{1}{2}\sin^2\theta(\hat{p}_x^2 - \hat{p}_y^2) + \sin 2\theta\hat{p}_x\hat{p}_z\right) \end{pmatrix} \quad (\text{B.6})$$

We study the effect of anisotropy described by Eq. (B.6) on the energy spectrum of electrons and holes. Figure B.1 compares the energy of the lowest electron levels in a 4 nm PbSe NW calculated within the cylindrical approximation and with complete numerical inclusion of the anisotropy. The anisotropy was taken into

account by diagonalizing the matrix elements of H_{an} in the space of the lowest 20 valence and highest 20 conduction states (that is, including the highest ten and lowest ten doubly degenerate electron and hole levels.) One can see in Fig. B.1 that the anisotropy in PbSe splits the nearly degenerate energy levels, whose radial or angular quantum momentum numbers differ by one in radial or angular quantum momentum numbers, while necessarily leaving the Kramer's degeneracy unbroken. The splitting should broaden the energy levels without an overall shift in the level position.

B.2 Calculations of the one dimensional Coulomb potential

Calculation of the one dimensional Coulomb potential in Eq. (4.19) and self interaction energy in Eq. (4.18) can be greatly simplified by initial averaging over angular variables. For the U_1 term of Eq. (4.19) the angular integration results

$$\langle U_1 \rangle(z) = \int_0^R d\rho_e \rho_e \int_0^R d\rho_h \rho_h |\Psi_e|^2 |\Psi_h|^2 V_1(\rho_e, \rho_h, z), \quad (\text{B.7})$$

where

$$V_1(\rho_e, \rho_h, z) = -4\pi \frac{e^2}{\kappa_s \sqrt{\rho_e \rho_h}} Q_{-1/2} \left(\frac{z^2 + \rho_e^2 + \rho_h^2}{2\rho_e \rho_h} \right) \quad (\text{B.8})$$

and Q_n is the Legendre function of the second kind. The two remaining radial integrals are evaluated numerically.

For the second term in Eq. (4.19), U_2 , the angular integrals vanish unless $m = 0$ leaving only this term from the sum. This results in the following expression for

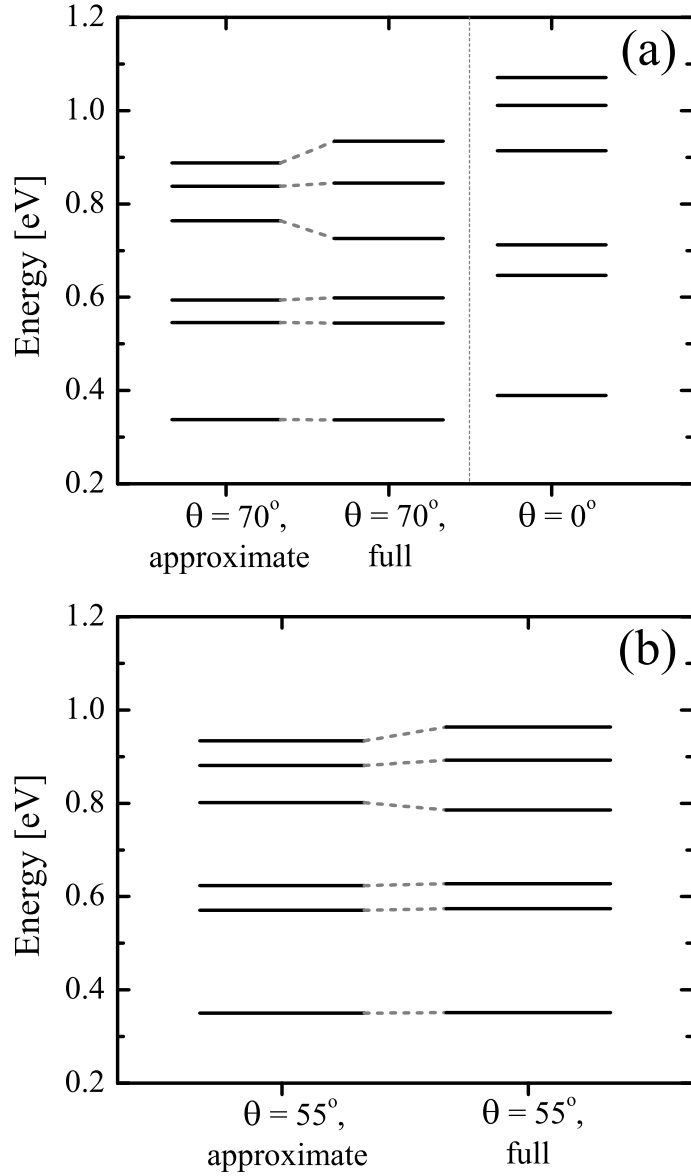


Figure B.1: Effect of the energy spectrum anisotropy on the energy of the 1D subband bottom in a 4 nm PbSe NW grown along the (a) $\langle 111 \rangle$ and (b) $\langle 100 \rangle$ crystal axes. The “approximate” calculations are conducted within the cylindrical approximation, which gives Eq. (4.15) for the energy levels. The “full” calculations are performed as described in the text. The energy levels are labeled by the angle between the L-point and the rod growth axis. Note that the $\theta = 0$ energy levels do not require perturbation, as $H_{an} = 0$ for that angle.

$\langle U_2 \rangle(z)$:

$$\begin{aligned} \langle U_2 \rangle(z) &= -8\pi \frac{e^2}{\kappa_s} \int_0^\infty du \frac{(\kappa_s - \kappa_m) K_0(Ru) K_1(Ru) \cos(uz)}{\kappa_s I_1(Ru) K_0(Ru) + \kappa_m I_0(Ru) K_1(Ru)} \times \\ &\times \underbrace{\left(\int_0^R d\rho_e \rho_e |\Psi_e|^2 I_0(u\rho_e) \right)}_{i_e(u)} \underbrace{\left(\int_0^R d\rho_h \rho_h |\Psi_h|^2 I_0(u\rho_h) \right)}_{i_h(u)}. \end{aligned} \quad (\text{B.9})$$

To calculate the integrals i_e and i_h in Eq. (B.9), we approximate the squared wavefunctions as a short sum of the form $|\Psi_e|^2 = \sum_{n=1}^N A_n (1 - \rho_e^{2n})$, with $N \approx 8$. Even with so few terms, the maximum relative error is typically $< 10^{-7}$. This allows us to solve these two integrals analytically:

$$\begin{aligned} i_e(u) &= \sum_{n=1}^N A_n \int_0^R d\rho_e \rho_e (1 - \rho_e^{2n}) I_0(u\rho_e) \\ &= \sum_{n=1}^N A_n \left(\frac{R I_1(u)}{u} - \frac{R^{2+2n} {}_1F_2(1+n; 1, 2+n; R^2 u^2/4)}{2+2n} \right), \end{aligned} \quad (\text{B.10})$$

where ${}_pF_q$ is the generalized hypergeometric function. The remaining integral over u in Eq. (B.9) is performed numerically.

Lastly, the two self interaction terms in Eq. (4.18), U_e and U_h , after angular integrations are reduced to

$$\begin{aligned} \langle U_{e,h} \rangle &= \frac{2e^2}{\kappa_s} \sum_{m=0}^\infty \int_0^\infty du \left(\int_0^R d\rho_{e,h} \rho_{e,h} |\Psi_{e,h}|^2 I_m^2(u\rho_{e,h}) \right) \times \\ &\times \frac{(\kappa_s - \kappa_m) K_m(Ru) (K_{m-1}(Ru) + K_{m+1}(Ru)) (2 - \delta_{m0})}{\kappa_s K_m(Ru) (I_{m-1}(Ru) + I_{m+1}(Ru)) + \kappa_m I_m(Ru) (K_{m-1}(Ru) + K_{m+1}(Ru))} \end{aligned} \quad (\text{B.11})$$

The two dimensional integrals in Eq. (B.11) was taken numerically. It is summed over only the first ≈ 20 values of m , as the sum converges rapidly.

B.3 Numerical calculation of the exciton binding in PbSe nanorods

Our analytic model makes the assumption that the 1D exciton is only weakly confined along the NR axis. In this case the finite length of the NR affects only the exciton center of mass motion. To verify this assumption, the 1D Hamiltonian was numerically diagonalized, while treating both binding and confinement exactly. As an orthogonal basis for this diagonalization we used a sufficiently large set of electron and hole plane waves that satisfied the single particle boundary conditions. The 1D exciton wave function in this basis set can be written as:

$$\Psi_{1D} = \sum_{n_e=1}^{N_e} \sum_{n_h=1}^{N_h} A_{n_e, n_h} \frac{2}{L} \sin\left(\frac{n_e \pi z_e}{L}\right) \sin\left(\frac{n_h \pi z_h}{L}\right) \quad (\text{B.12})$$

where A_{n_e, n_h} are the numerical coefficients.

The kinetic energy is diagonal in this basis, and matrix elements of Eq. (4.21) can be evaluated analytically. Calculation time was dominated by evaluation of these matrix elements and scaled as $O(N_e N_h)$. For $N_e = N_h \approx 30$, calculations were sufficiently converged for the lowest few dozen states, and required roughly one minute of computation time on a desktop computer. Results are detailed earlier in the text.

B.4 Choice of the room temperature band parameters

The absence of reliable room temperature energy band parameters for bulk PbSe has lead to several problems in the quantitative description of spherical PbSe NC electronic properties within effective mass theory, and as a result, to some

controversy on their electronic structure [1, 2, 3, 4, 5]. As has been noted [6, 2], effective mass theory significantly overestimates the energy gap in PbSe NCs (though not in PbS.) In addition, the nature of the 2nd optical transition is still a source of debate [7, 8, 9, 10], whether it is of symmetry type S-P or P-P. Considering the body of experimental evidence, the explanation put forward by Franceschetti [9] seems to offer the simplest explanation of this controversy, that the electron and hole P states are split into P_{\perp} and P_{\parallel} states by the anisotropy of the bands, and the second transition is of type P_{\parallel} - P_{\parallel} . These two problematic aspects of experimental spectra of PbSe NCs for effective mass theory— overestimation of the bandgap and the symmetry of the 2nd transition— as well as the observation of several optical transitions in a wide range of energies can be used for extraction of a real set of the energy band parameters.

Although the extraction of the set of energy band parameters from room temperature absorption spectra is possible, it is likely that many sets of parameters will equally well fit the first few optical transitions. In order to increase the accuracy of the fit, we want to somehow incorporate the energy band parameters in low temperature experiments in bulk PbSe. So, the total band edge effective masses for electrons and holes at $T = 4$ K are held constant at the values from experiment [11]. In addition, to limit the degrees of freedom in the fit, the anisotropy of the far-band contributions to both the electron and hole are held equal. That is, $m_l^+/m_t^+ = m_l^-/m_t^-$, even though their individual values will differ. With these constraints, a fit is performed using the body of literature data [12, 13, 14, 15, 16, 5] for the first transition, and the data from Koole [5] for the second and third transitions.

The final set of room temperature parameters are shown in Table 4.1 together

with the set of low temperature parameters reported for bulk PbSe in Ref. [11]. The transition energies calculated using these parameters are shown in Fig. B.2. The anisotropic effective mass calculations were performed using the method outlined in Ref. [17] and the results compared to the energies measured in Ref. [5], ignoring those points criticized in Ref. [18] as possibly being 2nd derivative artifacts.

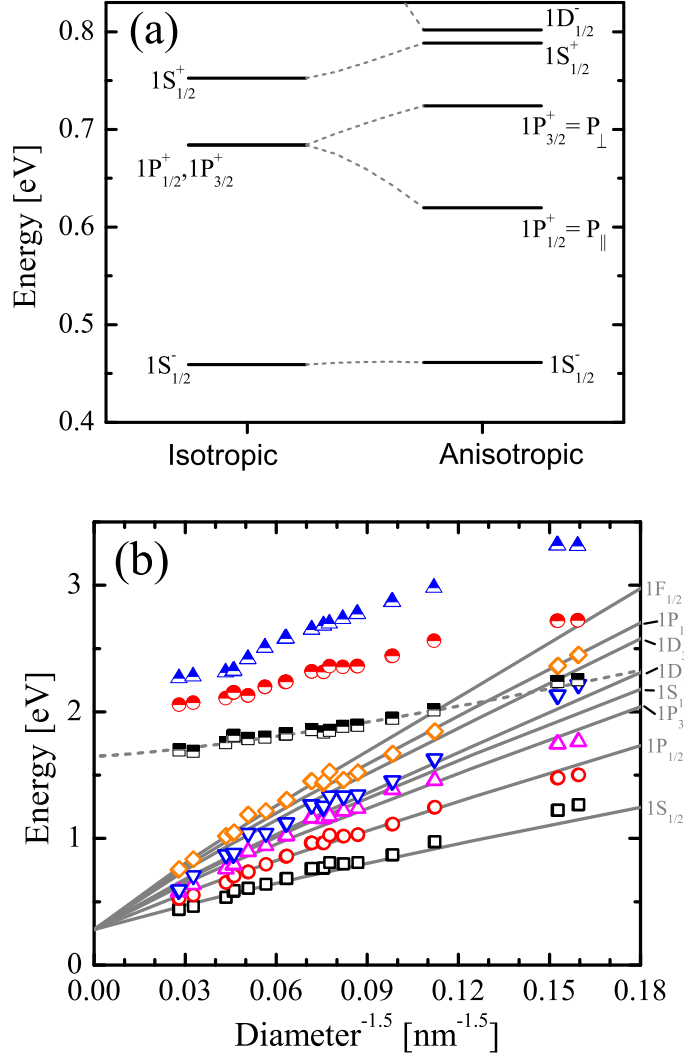


Figure B.2: Calculations of the lowest electron levels in spherical PbSe NCs. (a) Splitting of the P state induced by the fully anisotropic Hamiltonian in a 4 nm radius NC. Anisotropic states are labeled by writing the state in the basis of isotropic states, and labeling it by the isotropic state with largest coefficient. (b) The size dependence of the transition energies in spherical PbSe NCs. Experimental data [5] are shown by symbols. The solid lines show the size dependence of optically allowed transitions calculated in a fully anisotropic effective mass model. The optically allowed transitions occur between the states of the same symmetry but opposite parity, and we label them by a symmetry type, which is common for both states. Open points indicate transitions originating from the L-point in the Brillouin zone, while half-open points are suggested to be from the Σ point as in Ref. [5]. The dashed line shows the size dependence of lowest confined level connected with the Σ point of the Brillouin zone, calculated in a parabolic effective mass approximation as explained in the text.

BIBLIOGRAPHY

- [1] J. M. An, A. Franceschetti, S. V. Dudiy, and A. Zunger, *Nano Lett.* **6**, 2728 (2006).
- [2] G. Allan and C. Delerue, *Mater. Sci. Eng., C* **25**, 687 (2005).
- [3] S. V. Kilina, C. F. Craig, D. S. Kilin, and O. V. Prezhdo, *J. Phys. Chem. C* **111**, 4871 (2007).
- [4] A. Franceschetti, *Phys. Rev. B* **78**, 075418 (2008).
- [5] R. Koole, G. Allan, C. Delerue, A. Meijerink, D. Vanmaekelbergh, and A. Houtepen, *Small* **4**, 127 (2008).
- [6] A. Lipovskii, E. Kolobkova, V. Petrikov, I. Kang, A. Olkhovets, T. Krauss, M. Thomas, J. Silcox, F. Wise, Q. Shen, and S. Kycia, *Appl. Phys. Lett.* **71**, 3406 (1997).
- [7] H. Du, C. Chen, R. Krishnan, T. D. Krauss, J. M. Harbold, F. W. Wise, M. G. Thomas, and J. Silcox, *Nano Lett.* **2**, 1321 (2002).
- [8] J. J. Peterson, L. Huang, C. Delerue, G. Allan, and T. D. Krauss, *Nano Lett.* **7**, 3827 (2007).
- [9] A. Franceschetti, J. W. Luo, J. M. An, and A. Zunger, *Phys. Rev. B* **79**, 241311 (2009).
- [10] M. T. Trinh, A. J. Houtepen, J. M. Schins, J. Piris, and L. D. A. Siebbeles, *Nano Lett.* **8**, 2112 (2008).
- [11] H. Pascher, G. Bauer, and R. Grisar, *Phys. Rev. B* **38**, 3383 (1988).
- [12] C. B. Murray, S. Sun, W. Gaschler, H. Doyle, T. A. Betley, and C. R. Kagan, *IBM J. Res. Dev.* **45**, 47 (2001).
- [13] I. Moreels, K. Lambert, D. De Muynck, F. Vanhaecke, D. Poelman, J. C. Martins, G. Allan, and Z. Hens, *Chem. Mater.* **19**, 6101 (2007).
- [14] B. L. Wehrenberg, C. Wang, and P. Guyot-Sionnest, *J. Phys. Chem. B* **106**, 10634 (2002).

- [15] J. Steckel, S. Coe-Sullivan, V. Bulovic, and M. Bawendi, *Adv. Mater.* **15**, 1862 (2003).
- [16] W. W. Yu, J. C. Falkner, B. S. Shih, and V. L. Colvin, *Chem. Mater.* **16**, 3318 (2004).
- [17] G. E. Tudury, M. V. Marquezini, L. G. Ferreira, L. C. Barbosa, and C. L. Cesar, *Phys. Rev. B* **62**, 7357 (2000).
- [18] I. Moreels and Z. Hens, *Small* **4**, 1866 (2008).

NANOCRYSTAL VIBRATIONAL SPECTRA

C.1 Introduction

Coupling of the electronic structure to the vibrational structure is a somewhat less explored area of nanocrystal research. Though some work has gone into understanding the vibrational spectra of nanocrystals, even such fundamental concepts as the Huang-Rhys parameter in lead-salt quantum dots is not well established. This is true, even though the exchange of phonons is important in many of the hotly researched topics of nanocrystal science, including hot carrier relaxation, charge transfer, and multiple exciton generation.

Similar to how electronic structure provides a foundation for the study of electronic properties, the vibrational mode structure provides a similar foundation for studying vibrational properties or the electron-phonon coupling. Here we will present a novel method of calculating nanocrystal vibrational spectra, which is general enough to incorporate all previously developed methods as special cases. Experiments were performed to verify the models presented here, but the results have been questioned due to oxidation of the nanocrystals during the experiment. Further experiments are needed to address this issue, and the current results will not be presented here or discussed further.

C.2 Quantum Dot Vibrational Model

Vibrational modes can be calculated using a variety of methods, though all can be divided into two categories— atomistic and continuum. Atomistic methods calculate the forces on individual atoms, either using simple analytic models of charged spheres connected to various neighbors by springs, with enough free parameters to fit to experimental vibrational spectra, or through sophisticated wavefunction calculation methods, such as density functional theory, to directly calculate the forces. The former method is useful because it combines a model that can be intuitively grasped, often along with an analytic solution, and enough flexibility to be practically useful. But, it relies on the simplicity of periodic boundary conditions in bulk crystals in order to be easily solved, which are violated in nanostructures. The latter method is sufficiently complex to be beyond the scope here, though has had great success in small molecular systems. A third method, called the continuum method, attempts to retain as much small scale detail as possible without sacrificing the simplicity of an analytic theory, and will be the focus of the work presented here.

The continuum method models the nanostructure as an elastic solid, using a modified Navier equation to couple the vibrations of the polarized solid with an electrostatic field [1, 2]. It was first used to determine how the shape of microstructures affects their vibrational frequencies [3]. Later work has continued to adapt the model, improving its accuracy and allowing solutions in different structures. But as the model grew, it also diverged, and there are now a handful of different modifications of the theory. Because of this, we will present the theory in a novel way that is general enough to encompass most of these current modifications. Variables used and the overall approach of the derivation follows that of Roca [4].

C.2.1 The System of Equations

The continuum method is a combination of Maxwell's equations coupled to a Navier-like mechanical force equation. For crystal sizes much smaller than a wavelength, an electrostatic approximation is made, yielding only two coupled equations.

$$\rho(\omega^2 - \omega_{TO}^2)\mathbf{u} = -\nabla \cdot \bar{\bar{\tau}} + \alpha \nabla \Phi \quad (\text{C.1})$$

$$\nabla \cdot (\epsilon_\infty \nabla \Phi) = 4\pi \nabla \cdot (\alpha \mathbf{u}) \quad (\text{C.2})$$

where $\alpha^2 = \epsilon_\infty \rho (\omega_{LO}^2 - \omega_{TO}^2) / 4\pi$, \mathbf{u} is the mechanical vibration displacement, Φ is the electrostatic potential, $\bar{\bar{\tau}}$ is a stress-tensor which defines the short-range vibrational forces between ions, ω_{TO} and ω_{LO} are the zone-center transverse and longitudinal optical frequencies, ρ is the reduced-mass density, and ϵ_∞ is the high frequency dielectric constant.

Most of the differences presented in the literature involve the choice of the stress tensor $\bar{\bar{\tau}}$. Typically a simple analytic form is chosen for it, designed to capture the initial curvature of the vibrational bands around the zone-center minima in bulk crystal. The idea being that the effect of making a finite sized crystal is that the vibrational modes no longer have a single wavevector \bar{k} , but rather have a spread of values determined by the size of the nanocrystal. But, because the vibrational spectra in nanocrystals requires wavevector components reaching magnitudes $\lesssim \pi/R$, which for small crystals ($R \approx 5-10a$) can be a significant fraction of the π/a size of the Brillouin zone. As a result, more information about the bulk vibrational band structure is needed than just the initial zone-center curvature. As a result, in order to be able to make a more general theory, we need a manner to construct this tensor that can incorporate more information about the vibrational band structure in bulk.

In a rigorous theory, the tensor $\bar{\bar{\tau}}$ can be chosen to perfectly fit bulk dispersion curves, but this would result in a matrix *functional* of the displacement \mathbf{u} . In quantum dots, certain approximations need to be made to retain analytic solvability. First, spherical boundary conditions require some form of isotropic approximation. Second, its functional form can be approximated as having the form of a linear differential operator. To that end, we introduce a general form for the divergence of $\bar{\bar{\tau}}$ by introducing two unknown linear differential operators \hat{O}_L and \hat{O}_T .

$$\nabla \cdot \bar{\bar{\tau}} = \nabla(\rho \hat{O}_L \nabla \cdot \mathbf{u}) - \nabla \times (\rho \hat{O}_T \nabla \times \mathbf{u}) \quad (\text{C.3})$$

With that definition, taking separately the divergence and curl of Eq. (C.1) produces the following two equations:

$$\nabla^2 \hat{O}_L \nabla \cdot \mathbf{u} = (\omega^2 - \omega_{LO}^2) \nabla \cdot \mathbf{u} \quad (\text{C.4})$$

$$\nabla^2 \hat{O}_T \nabla \times \mathbf{u} = (\omega^2 - \omega_{TO}^2) \nabla \times \mathbf{u} \quad (\text{C.5})$$

The above equations have a simple operator-eigenvalue form, which suggests a method of solution. Restricting $\hat{O}_{L,T}$ to the set of hermitian operators, then because it commutes with ∇^2 by construction, then these operators share a complete set of eigenvectors and eigenvalues. That is, using the following definitions of the eigenvalues of ∇^2 :

$$\nabla^2(\nabla \times \mathbf{u}) = -Q^2(\nabla \times \mathbf{u}), \quad \nabla^2(\nabla \cdot \mathbf{u}) = -q^2(\nabla \cdot \mathbf{u}) \quad (\text{C.6})$$

Then we define the following to be true:

$$\hat{O}_L(\nabla \cdot \mathbf{u}) = \frac{\omega_{LO}^2 - \omega_L^2(q)}{q^2} \nabla \cdot \mathbf{u}, \quad \hat{O}_T(\nabla \times \mathbf{u}) = \frac{\omega_{TO}^2 - \omega_T^2(Q)}{Q^2} \nabla \times \mathbf{u} \quad (\text{C.7})$$

where the functions $\omega_L(q)$ and $\omega_T(Q)$ are defined such that Eqs. (C.7) are true, and the form of those equations has been chosen to simplify later expressions. This

simplifies Eqs. (C.4, C.5) into

$$[\omega^2 - \omega_T^2(Q)] \nabla \times \mathbf{u} = 0 \quad (\text{C.8})$$

$$[\omega^2 - \omega_L^2(q)] \nabla \cdot \mathbf{u} = 0 \quad (\text{C.9})$$

Solutions to the complete system of equations (C.2, C.6, C.8, C.9) are found by first solving the Helmholtz equations (C.6) for the current system geometry, and then combining those two solutions for $\nabla \cdot \mathbf{u}$ and $\nabla \times \mathbf{u}$ as follows:

$$\mathbf{u} = -\frac{1}{q^2} \nabla(\nabla \cdot \mathbf{u}) + \frac{1}{Q^2} \nabla \times (\nabla \times \mathbf{u}) + \frac{\alpha}{\rho(\omega^2 - \omega_{TO}^2)} \nabla \Phi_H \quad (\text{C.10})$$

$$\Phi = \Phi_H - \frac{4\pi\alpha}{\epsilon_\infty q^2} \nabla \cdot \mathbf{u} \quad (\text{C.11})$$

where Φ_H is an additional arbitrary function that satisfies the Laplace equation $\nabla^2 \Phi_H = 0$.

In order to not lose the meaning behind these equations, it's important to quickly review what has been done here. We originally noted the need for a more general form of the stress tensor $\bar{\bar{\tau}}$, and decided on a form that includes the (still undetermined) operators $\hat{O}_{L,T}$. But, even though these operators are still arbitrary, we were able to construct solutions to our differential equations, Eqns. (C.1, C.2). We did so by expressing the solutions in terms of the solutions to the simpler Helmholtz equations (C.6), and the unknown functions $\omega_L(q)$ and $\omega_T(Q)$. The solutions to those simpler equations can be found for simple geometries in standard texts, while the unknown functions will be determined from the bulk vibrational band structure as follows.

C.2.2 Description of Solutions

In an infinite periodic crystal, we require that the vibrational spectrum becomes that of the bulk crystal. Periodic boundary conditions provide two simplifications to the solutions in Eqs. (C.10, C.11). First, $\Phi_H = 0$ because there are no other periodic solutions to the Laplace equation. Second, the solutions decouple into independent longitudinal and transverse modes. Because of our isotropic approximation, their dispersion curves are also isotropic, with $\omega_L(q)$ and $\omega_T(Q)$ for wavevector magnitude q and Q , respectively.

Thus, we can choose the functions ω_L and ω_T to best match the material's bulk dispersion curves, within a spherical Brillouin zone approximation. Ideally, one should use the direction in k-space that has the largest density of states to determine the functions, though some sort of averaging could also be used.

Conversely, in a nanostructure the boundary conditions may not allow the longitudinal and transverse solutions to decouple. In general though, Eqs. (C.8, C.9) must be satisfied, so the types of possible solutions can be classified as one of the following four choices.

- a) $\nabla \times \mathbf{u} = 0, \quad \omega = \omega_L(q)$: Pure Longitudinal Modes
- b) $\nabla \cdot \mathbf{u} = 0, \quad \omega = \omega_T(Q)$: Pure Transverse Modes
- c) $\omega = \omega_T(Q) = \omega_L(q)$: “Mixed” Modes
- d) $\nabla \cdot \mathbf{u} = 0, \quad \nabla \times \mathbf{u} = 0$: “Dielectric” Modes

Mixed modes are so named because they have both a longitudinal and transverse component, while dielectric modes derive their name from the so-called dielectric continuum model [3] which shares their solutions.

It is important to make clear that not all four types of solutions will be allowed

in any given structure. The type of dispersion curves and boundary conditions chosen will affect which types of solutions are allowed. Specifically, (a) and (b) require boundary conditions that decouple transverse and longitudinal equations, (c) requires there to be overlap between the dispersion curves, while (d) requires a very specific class of boundary conditions, discussed later.

C.2.3 Boundary Conditions in Heterostructures

For the case of material interfaces with piecewise-continuous material parameters, the boundary conditions can be derived by integrating the differential equation across the boundary. Assuming that both \mathbf{u} and Φ are continuous, integrating Eqs. (C.1, C.2) across a boundary, referred to as $-\epsilon$ to $+\epsilon$, yields:

$$\hat{n} \cdot \bar{\bar{\tau}} \Big|_{-\epsilon}^{+\epsilon} = 0 \tag{C.12}$$

$$\hat{n} \cdot (4\pi\alpha\bar{u} - \epsilon_\infty \bar{\nabla}\Phi) \Big|_{-\epsilon}^{+\epsilon} = 0 \tag{C.13}$$

The equations are the usual conditions of continuity of the normal component of the stress (C.12) and the electric displacement (C.13). One small subtlety has been overlooked, though. Since the original equations only specify $\bar{\nabla} \cdot \bar{\bar{\tau}}$, there's an apparent gauge freedom in our choice of the stress tensor. Thus, it may incorrectly appear as if there were also a gauge freedom in the choice of boundary condition (C.12). Though there is a gauge freedom in the choice of $\bar{\bar{\tau}}$, in order to have the boundary condition have the precise form of (C.12), one is forced to a specific gauge. This is not the choice made by some previous authors working with quantum dots [4], who instead chose a gauge that made $\bar{\bar{\tau}}$ symmetric, which

contradicts their boundary conditions. The correct choice is:

$$\begin{aligned}\tau_{ij} &= -\rho \hat{O}_L (\bar{\nabla} \cdot \bar{u}) \delta_{ij} - \rho \hat{O}_T (\bar{\nabla} \times \bar{u})_k \epsilon_{ijk} \\ &= -\rho \frac{\omega_{LO}^2 - \omega_L^2(q)}{q^2} (\bar{\nabla} \cdot \bar{u}) \delta_{ij} - \rho \frac{\omega_{TO}^2 - \omega_T^2(Q)}{Q^2} (\bar{\nabla} \times \bar{u})_k \epsilon_{ijk} \quad (\text{C.14})\end{aligned}$$

It is important to note that the boundary condition enforces the continuity of $\hat{n}_i \tau_{ij}$, with the index contraction on the *left side*. Since the tensor has an antisymmetric component, this choice is important. With these boundary conditions, the solution of any nanoscale heterostructure is straightforward and uniquely determined.

C.2.4 Boundary Conditions in Quantum Dots

Even though the boundary conditions are clear when working within a heterostructure, they are not clear in cases such as quantum dots suspended in a solvent. Because the model assumes all regions to be occupied by elastic solids, the model's parameters are not necessarily well-defined in the outside region, which includes possibilities such as solvents or vacuum. Thus it is meaningless to enforce the continuity equations (C.12, C.13), and one needs to propose a new set of boundary conditions.

The electric potential Φ and the dielectric constant ϵ_{out} are still meaningful in the outside material. Thus, it is at least straightforward to adapt (C.13), by just omitting the \bar{u} contribution to the electric displacement in the outside material. On the other hand, it is not clear how to change (C.12), and as a result, multiple methods have become common.

Currently, the common choices can be classified first as either “stiff” or “free”, and second as either “mixed” or “pure”. Stiff boundary conditions enforce zero

displacement at the quantum dot surface, corresponding to surface atoms held rigidly in place; while soft boundary conditions enforce zero stress at the surface, corresponding to surface atoms moving freely. In addition, pure boundary conditions enforce pure longitudinal or transverse solutions, while mixed conditions forbid them.

Table C.1: Boundary conditions at the surface of nanocrystals. The common electromagnetic BCs are shown on top, while the four common choices of mechanical BCs are on bottom.

Electromagnetic Boundary Conditions		
$\Phi_{in} _R = \Phi_{out} _R$		
$\hat{r} \cdot (4\pi\alpha\bar{u} - \epsilon_\infty\bar{\nabla}\Phi) _R = \hat{r} \cdot (-\epsilon_{out}\bar{\nabla}\Phi) _R$		
Mechanical Boundary Conditions		
	Stiff	Free
Pure	$\hat{r} \cdot \bar{u} _R = 0$ $\bar{\nabla} \cdot \mathbf{u} = 0$ or $\bar{\nabla} \times \mathbf{u} = 0$	$\hat{r} \cdot \bar{\bar{r}} \cdot \hat{r} _R = 0$ $\bar{\nabla} \cdot \mathbf{u} = 0$ or $\bar{\nabla} \times \mathbf{u} = 0$
Mixed	$\bar{u} _R = 0$	$\hat{r} \cdot \bar{\bar{r}} _R = 0$

For quantum dots, previous work has emphasized both pure [1, 5] and mixed [4, 6], and also both stiff [5, 4, 6, 7] and free [7] boundary conditions. Thus, there are situations under which all of the above choices accurately reproduce experimental data.

C.2.5 Theoretical Pitfalls

A few notable complications arise when using this model. Foremost is that many boundary conditions require the coupling of transverse and longitudinal components, requiring both $\bar{\nabla} \cdot \bar{u} \neq 0$ and $\bar{\nabla} \times \bar{u} \neq 0$. Equations (C.8, C.9) then require that the dispersion curves overlap at the frequency ω ; but in many materials, the

dispersion curves *never* overlap over the entire Brillouin zone.

In order to resolve this dilemma, one must look outside of the Brillouin zone, specifically at imaginary wavevectors. Normally, in large crystals, imaginary wavevectors are disallowed because they lead to exponential solutions that don't satisfy the periodic boundary conditions. But in a confined structure, like a quantum dot, there is no mathematical reason to disallow them.

If somehow the analytic form of the dispersion curve is known, then the behavior of $\omega(k)^2$ with imaginary k is clear. But when the formula is unknown, or in the important case of a fit to experimental dispersion curves, its behavior depends strongly on the details of the fit, because we require an extrapolation to negative k^2 . Thus, care must be taken when making these fits, so that the behavior under imaginary wavevector is at least physically reasonable, and is hopefully motivated with some physical model.

C.2.6 Conclusion

Here we have presented a simple and novel method for the calculation of QD vibrational spectra. Depending on the boundary conditions considered and the complexity of the chosen functions $\omega_L(q)$ and $\omega_T(Q)$, all previously published methods can be reproduced as special cases.

BIBLIOGRAPHY

- [1] M. Babiker, J. Phys. C: Solid State Phys. **19**, 683 (1986).
- [2] M. Born and K. Huang, *Dynamical theory of crystal lattices* (Oxford University Press, London, 1954).
- [3] R. Ruppin and R. Englman, Reports on Progress in Physics **33**, 149 (1970).
- [4] E. Roca, C. Trallero-Giner, and M. Cardona, Phys. Rev. B **49**, 13704 (1994).
- [5] E. P. Pokatilov, S. N. Klimin, V. M. Fomin, J. T. Devreese, and F. W. Wise, Phys. Rev. B **65**, 075316 (2002).
- [6] M. P. Chamberlain, C. Trallero-Giner, and M. Cardona, Phys. Rev. B **51**, 1680 (1995).
- [7] M. I. Vasilevskiy, Phys. Rev. B **66**, 195326 (2002).